

Dissertation
zur Erlangung des akademischen Grades eines
Doktors der Naturwissenschaften in der Fakultät
Physik der Technischen Universität Dortmund

Investigation of n^+ -in-n Planar Silicon Pixel Detectors for Application in the ATLAS Experiment

vorgelegt von

Dipl.-Phys. Silke Altenheiner
Lehrstuhl für Experimentelle Physik IV
Fakultät für Physik
Technische Universität Dortmund

Dortmund, Mai 2015



Dissertation
zur Erlangung des akademischen Grades
eines Doktors der Naturwissenschaften
in der Fakultät Physik
der Technischen Universität Dortmund

Investigation of n^+ -in-n Planar Silicon Pixel Detectors for
Application in the ATLAS Experiment

vorgelegt von

Dipl.-Phys. Silke Altenheiner
Lehrstuhl für Experimentelle Physik IV
Fakultät für Physik
Technische Universität Dortmund

Dortmund, Mai 2015

Gutachter:	Prof. Dr. C. Gößling, TU Dortmund
Zweitgutachter:	Prof. Dr. K. Kröninger, TU Dortmund
Vorsitzender der Prüfungskommission:	Prof. Dr. G. Uhrig, TU Dortmund
Beisitzer:	Dr. B. Siegmann, TU Dortmund
Termin der mündlichen Prüfung:	9. Juli 2015

Life is either a great adventure or nothing. - Helen Keller

Contents

1. Introduction	1
2. The LHC and the ATLAS Detector	3
2.1. The Large Hadron Collider	3
2.2. LHC Upgrades	3
2.3. The ATLAS Detector	5
2.4. ATLAS Upgrades	8
2.4.1. The ATLAS Pixel Insertable B-Layer (IBL)	9
3. Radiation damage in silicon	13
3.1. Crystal Defect Types	13
3.2. Type inversion	14
3.3. Annealing	15
3.4. Leakage Current	16
4. ATLAS Pixel Sensors	19
4.1. Principles of Silicon Particle Detectors	19
4.1.1. Energy Loss of Photons in Matter	19
4.1.2. Energy Loss of Charged Particles in Matter	20
4.1.3. Intrinsic and Extrinsic Semiconductors	21
4.1.4. The pn-Junction	22
4.1.5. Float Zone and Magnetic Czochralski Silicon	22
4.2. ATLAS Pixel Sensor Modules	23
4.2.1. ATLAS Pixel Sensor	24
4.2.2. Front End I3	25
4.2.3. Bump Bonding	25
4.3. IBL Sensors	25
4.4. Front End I4	27
4.5. FE-I4 Single Chip Assembly	28
5. Methodology	31
5.1. Measurement of IV Characteristics	31
5.2. Irradiation Sites	31
5.3. Operation of FE-I4 ATLAS ReadOut Chips	33
5.3.1. USBpix ReadOut-System and STControl	33
5.3.2. Tuning and Standard Scans	34
5.3.3. Single Chip Card	40
5.4. Laboratory Setup	40
5.4.1. Cooling	42
5.4.2. Source carrier	42
6. TestBeam	45

6.1.	Beam-Lines	45
6.2.	Testbeam Setup	46
6.2.1.	Telescope	46
6.2.2.	Cooling and Mechanics	47
6.2.3.	The Telescope-DAQ-Software	49
6.3.	Analysis Chain	55
6.3.1.	Reconstruction with EU Telescope	55
6.3.2.	TBmon	56
6.3.3.	Uncertainty of the testbeam measurements	60
7.	Results of Lab and TestBeam Measurements	65
7.1.	Devices under test	65
7.2.	IBL sensors	65
7.2.1.	Cooling and temperature dependencies	66
7.2.2.	Sensor efficiencies	68
7.2.3.	Edge efficiency	78
7.2.4.	Summary of the IBL sensors measurements	79
7.3.	Magnetic Czochralski sensors	79
7.3.1.	IV and CV Measurements	79
7.3.2.	Tuning before and after irradiation	81
7.3.3.	Testbeam measurements unirradiated	82
7.3.4.	Measurements after pion irradiation	83
7.3.5.	Summary of the MCz and FZ sensors	84
8.	Conclusions and Outlook	89
A.	Details of Testbeam Measurements	97
A.1.	IBL Testbeam Campaigns	97
A.2.	MCz and FZ comparison	98
B.	Publications	103

1. Introduction

The study of fundamental particles and interactions in the last century has led to a deep understanding of the microscopic structure of the universe and resulted in a detailed understanding of the Standard Model. The Standard Model is comprised of a fundamental set of particles and their interactions through the electroweak and the strong nuclear force. The fundamental set of particles consists of three generations of quarks and leptons and four gauge bosons. The ongoing effort to understand the subatomic world requires very high energies and high statistics.

The Large Hadron Collider (LHC) is currently the largest ring collider in the world. It has a designed centre-of-mass energy of 14 TeV and a designed luminosity of $10^{34}\text{cm}^{-2}\text{s}^{-1}$. One of the two large multi-purpose detectors at the LHC is the ATLAS¹ detector. The first huge achievement of ATLAS and the other multi-purpose detector CMS² was the discovery of the Higgs Boson at 125 GeV in 2012. This discovery leads to the Nobel Prize in Physics in 2013, however, despite this discovery the end of particle Physics has not been reached. Physics beyond the Standard Model is still under investigation, examples for this research are super symmetry and CP violation which could explain the asymmetry of antimatter and matter in the universe.

The ATLAS detector consists of several sub-detectors, each with different tasks. An overview of these sub-detectors, ATLAS, and the LHC in general, is given in chapter 2. During the last long-shutdown the Inner Detector of ATLAS was upgraded with the insertion of an additional layer between the first pixel layer and a smaller beam pipe, the so called Insertable B-Layer (IBL). It improves the vertex resolution of ATLAS.

The impact of radiation on the sensor material is described in chapter 3. This is important since the IBL is extremely close to the interaction point. A description of the operating mode of the sensor and the readout electronic that is used for the ATLAS pixel detector and the IBL can be found in chapter 4. The methodology detailing irradiation of the sensors and subsequent measurements are explained in chapter 5. Chapter 6 gives an overview of the testbeam principles, the reconstruction, and analysis chain. Prior to the construction and insertion of the IBL, many testbeam measurements and verification of the defined requirements for the detector were also performed, these are described in chapter 2. The main scope of this thesis is the investigation of n⁺-in-n planar pixel sensors, intended to be paired with the FEI4B front-end readout chip, to fit the specifications of IBL. A significant contribution to the data taking during the testbeams has been done. This includes the preparation, debugging, and expert operation of the samples. The final results of testbeam and laboratory measurements are presented in chapter 7. Finally, a summary of the measurements and observations is given in chapter 8 as well as an outlook on further measurements.

¹A Toroidal LHC ApparatuS

²Compact Myon Solenoid

2. The LHC and the ATLAS Detector

2.1. The Large Hadron Collider

The Large Hadron Collider (LHC) at CERN¹ is a ring accelerator with a circumference of 27 km and is about 100 m below ground level. It is currently the world's largest proton accelerator with a maximum energy of 7 + 7 TeV. It is also possible to collide heavy ions. The LHC is the last accelerator within a chain of accelerators, the whole complex is shown in Figure 2.1.

The acceleration starts with protons from ionized H₂ within LINAC² where they are accelerated in bunches up to an energy of 50 MeV before they are injected to the Booster. They leave the Booster with an energy of 1.4 GeV. The Proton Synchrotron (PS) and the Super Proton Synchrotron (SPS) increase the energy up to 26 GeV and 450 GeV.

Afterwards they get into the LHC which has four interaction points where the two separated beam pipes are crossed to generate collisions. Up to 20 protons out of the 10¹¹ protons per bunch interact. At each collision point a detector is located to measure and record the produced particles. These particle detectors are ATLAS³, CMS⁴, LHCb⁵ and ALICE⁶.

ATLAS and CMS are multipurpose detectors. ALICE is specialized in heavy ion collisions and LHCb on CP violation in $b\bar{b}$ -systems.

2.2. LHC Upgrades

The LHC Upgrade is planned in three steps, see Figure 2.2. Each shutdown of the machine will last between one and two years and has a different focus.

Phase-0

This long shutdown (LS1) started from early 2013 and last until the end of 2014. For an LHC operation at an energy of 7 TeV per beam and at the design luminosity of 10³⁴ cm⁻²s⁻¹ it was needed to consolidate the magnet inter-connects to get stronger magnetic fields. In April 2015 the LHC circulated successfully a beam at 6.5 TeV.

¹European organization for nuclear research (the acronym stands for: **C**onseil **E**uropeen pour la **R**echerche **N**ucleaire and is a remnant of the establishment)

²**L**INear **A**Ccelerator

³**A** Toroidal **L**H**C** **A**pparatu**S**

⁴**C**ompact **M**uon **S**olenoid

⁵**L**arge **H**adron **C**ollider **b**eauty

⁶**A** **L**arge **I**on **C**ollider **E**xperiment

2. The LHC and the ATLAS Detector

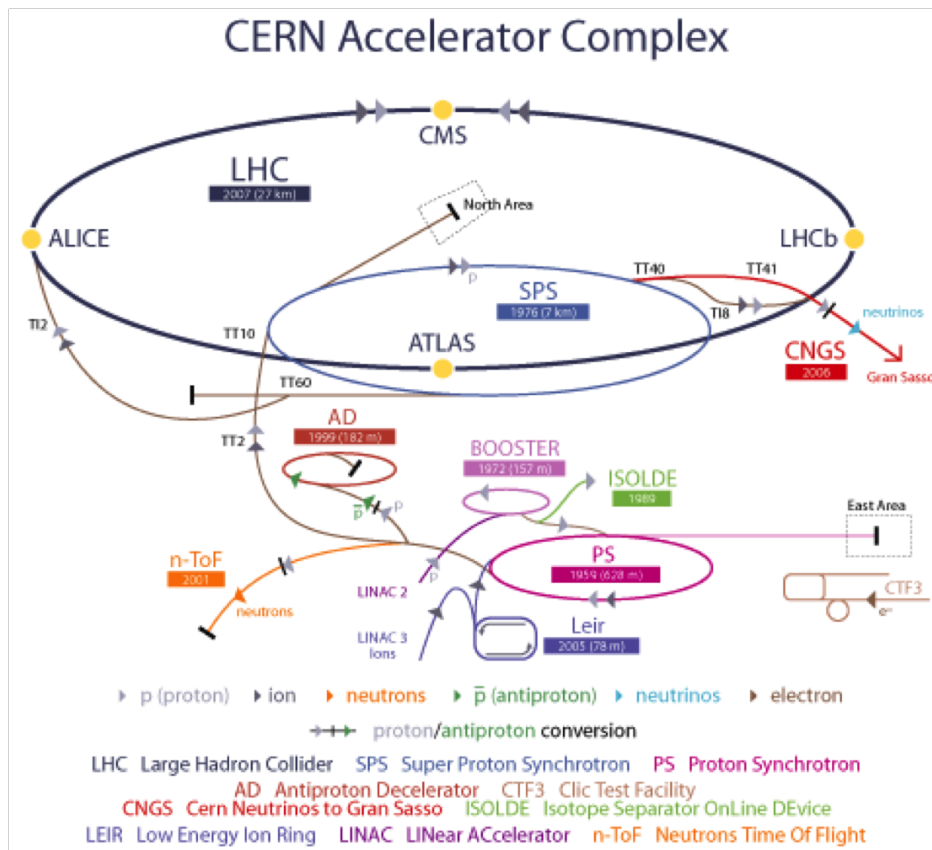


Figure 2.1.: Image of the CERN accelerator complex with its detectors [1]

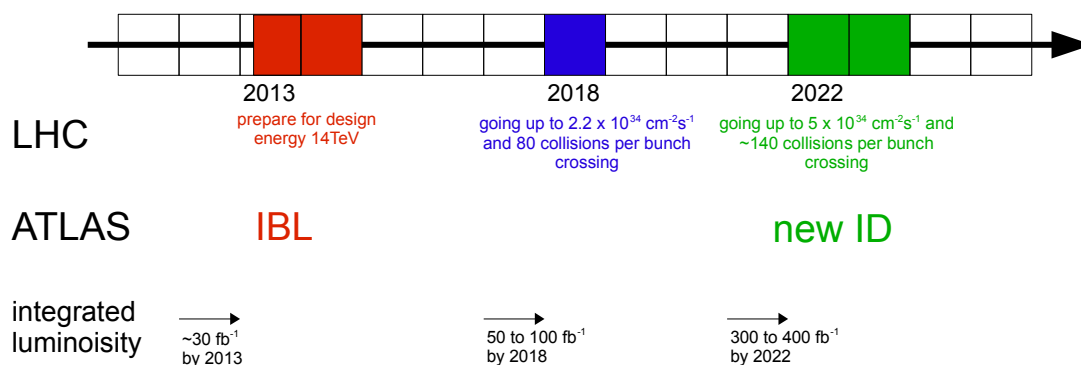


Figure 2.2.: Time schedule for the LHC and ATLAS upgrades. Information from [2]

Phase-I

The second LS is planned for the year 2018. After LS2 the LHC luminosity will be increased to $2.2 \cdot 10^{34} \text{ cm}^{-2}\text{s}^{-1}$. A new LINAC will be inserted as a replacement for the existing LINAC2. This in combination with collimation upgrades in the accelerator complex increases the number of particles per bunch. The LHC should deliver up to 400 fb^{-1} in the following run phase.

Phase-II

In the shutdown after 2022 it is planned to increase the luminosity up to $5 \cdot 10^{34} \text{ cm}^{-2}\text{s}^{-1}$. The technologies needed to realize this goal are under research and development.

2.3. The ATLAS Detector

The ATLAS detector is with its length of 44m, a diameter of 25 m and a weight of about 7000 t the largest detector at the LHC.

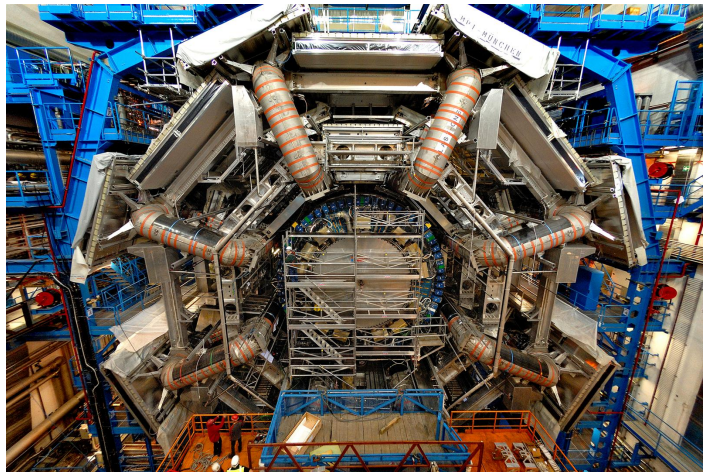


Figure 2.3.: View of ATLAS during assembly. The muon system, toroid magnets and the inner detector can be seen. [3]

ATLAS consists of four sub-detectors:

- Inner Detector
- Electromagnetic Calorimeter
- Hadronic Calorimeter
- Muon Spectrometer

Inner Detector

The Inner Detector (ID) is the innermost component of the ATLAS Detector and contains the Pixel Detector, the SCT⁷ and the TRT⁸. The whole ID has a length of

⁷SemiConductor Tracker

⁸Transition Radiation Tracker

2. The LHC and the ATLAS Detector

6.2 m with a diameter of 2.1 m.

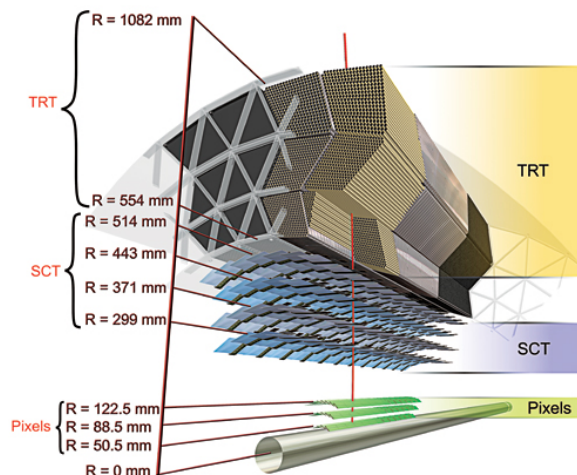


Figure 2.4.: Components of the inner detector of ATLAS [4]

Pixel Detector The pixel detector is nearest to the interaction point. It consists of 1744 identical pixel modules. These modules are described in section 4.2. They are mounted on cooling and local support structures, so called staves, around the beam line. These staves are forming three concentric barrel layers. The innermost one, the B-Layer; is located at a radius of 5.05 cm.

To complete the detector there are two end-caps on both sides with three disks each for large pseudorapidity values⁹ up to $|\eta| = 2.5$.

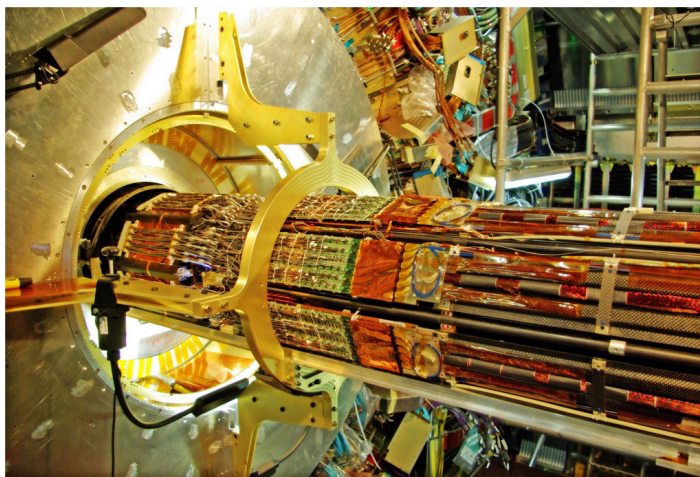


Figure 2.5.: Picture of the ATLAS pixel detector during its installation [3]

Semi Conductor Tracker The SCT consists of four barrel layers and nine endcaps on each side. It is made of silicon single sided p-in-n microstrip sensors. By using a strip detector the position of a traversing particle can be estimated in one dimension only. To get a two-dimensional hit information it has two layers of microstrip sensors and they are rotated against each other by a stereo angle of 40 mrad.

⁹The pseudorapidity η is defined by $\eta = -\ln \tan(\theta/2)$, with the polar angle θ with regard to the beam axis.

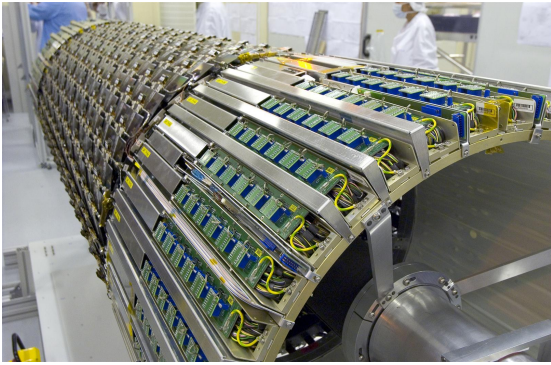


Figure 2.6.: Picture of the silicon tracker. [3]

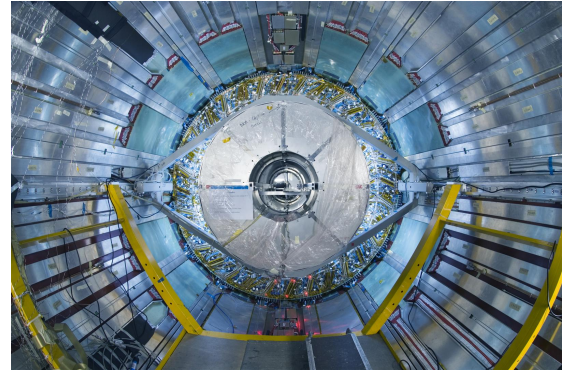


Figure 2.7.: The completed TRT barrel with all services. [3]

Radiation Tracker The TRT is the outermost part of the inner detector. It is composed of straw-tubes with a diameter of 4 mm which are filled with a xenon-based gas mixture. In total the TRT is 2.3 m in diameter and 7 m in length. On average a particle crosses 36 straws while passing the TRT, which has a spatial resolution of approximately $130 \mu\text{m}$.

Besides, the TRT can be used for electron identification as well. Electrons passing the passive material emit transition radiation due to the different dielectric constants. This radiation can be detected by the straws.

Calorimeters

There are two different types of calorimeter in ATLAS, the electromagnetic calorimeter (EMCAL¹⁰) and the hadronic calorimeter (HCAL¹¹). Both are sampling calorimeters with active and passive material for interacting with the particles and measurement of the resulting showers.

The EMCAL measures photons and electrons. It uses liquid argon as a sampling material and the absorber is made of lead. The HCAL can detect all hadrons. It is build out of steel and scintillator material.

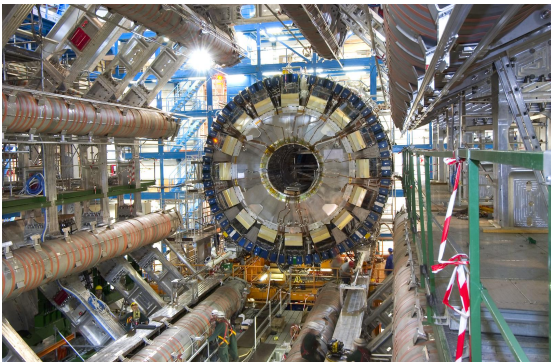


Figure 2.8.: View of the ATLAS calorimeter along one of eight toroid magnets [3]

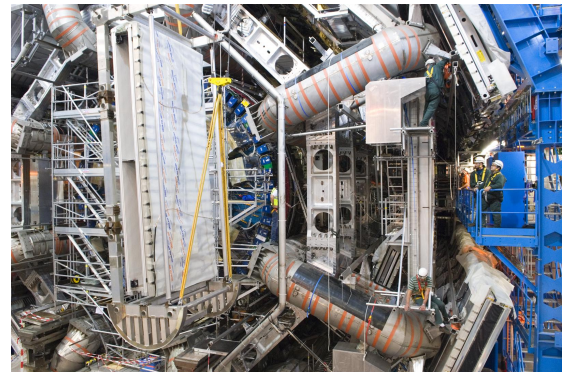


Figure 2.9.: Installation of the ATLAS muon barrel chambers [3]

¹⁰ElectroMagnetic CALorimeter

¹¹Hadronic CALorimeter

Muon Spectrometer

The muon spectrometer is the outermost part of the detector. Only muons and neutrinos can reach the muon spectrometer. All other particles are stopped in the calorimeters. Neutrinos reach the muon spectrometer but they are not detectable with ATLAS. The muon spectrometer consists of four different detector types:

- Resistive Plate Chambers (RCP):
They are segmented gaseous parallel electrode-plates operating in avalanche mode and are used for triggering in the central region.
- Thin Gap Chambers (TGC):
These are multi-wire proportional chambers in the forward regions.
- Monitored Drift Tubes (MDT):
They are used in the barrel region for high resolution tracking and are drift tubes filled with a gas mixture.
- Cathode Strip Chambers (CSC):
These are multi-core proportional chambers with strip cathodes.

The final layer of ATLAS is a toroidal magnet system. It provides a magnetic field in the range of 0,5 T in the barrel and 1 T in the end cap.

Trigger system

In ATLAS the TDAQ¹² is used to preselect and store the data of main interest. The first stage is a hardware based trigger system, the Level-1 trigger. It uses mainly the calorimeter and the muon system to select events of potential interest and reduces the rate of selected events to ~ 75 kHz. The selected events are stored on readout buffers and the further processing is done by the HLT¹³. The HLT consists of a Level-2 trigger and the Event Filter algorithm. With the help of the HLT the event rate is reduced to 200 Hz.

2.4. ATLAS Upgrades

The ATLAS collaboration will use the three shutdowns of the LHC (see Figure 2.2) to upgrade the whole detector to cope with the increased luminosity rates. It is also planned to repair and consolidate detector parts which failed during the preceding operation.

Phase-0

During the LS 1 a new fourth pixel layer, the IBL¹⁴, was installed at a radius of 3.2 cm between a new beam pipe and the existing pixel detector. The current pixel detector services for the modules were corrected.

The IBL project is described in detail in chapter 2.4.1.

¹²multi-level **T**igger and **D**ata **A**cquisition system

¹³**H**igh **L**evel **T**igger

¹⁴**I**nsettable **B**-**L**ayer

Phase-I.

The second upgrade phase should prepare the detector for the luminosity of $2.2 \cdot 10^{34} \text{ cm}^{-2}\text{s}^{-1}$. There is no update of the pixel detector foreseen during LS2. The IBL installation during LS1 will ensure a good performance of the pixel detector.

The LOI¹⁵ [5] (finished at the end of 2011) focuses on upgrades to the forward regions of the muon and calorimeter systems.

Phase-II.

In the currently last planned upgrade phase the focus will be on the inner detector. The inner detector will be deteriorated by radiation to its design limits and require a complete replacement.

A replacement completely based on silicon sensors is planned. It incorporates four pixel layers, three short strip (striplet) layers and two strip layers in the barrel part and in the forward region seven strip discs and six pixel discs. A simulation of the non ionising energy loss dose for the different layers is given in figure 2.10.

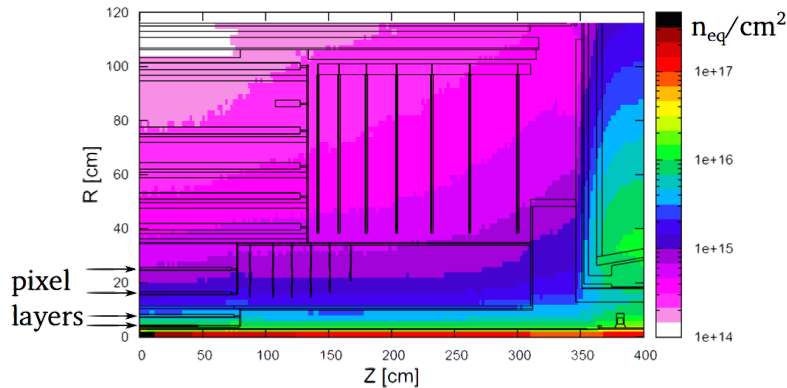


Figure 2.10.: Fluence for the ATLAS Inner Detector as a function of distance from the interaction point (in R outwards and Z along the beam pipe). The fluence is given in units of $1 \text{ MeV } n_{eq}\text{cm}^2$ [6]

2.4.1. The ATLAS Pixel Insertable B-Layer (IBL)

As mentioned in the section above the current phase-0 shutdown was used to install an additional pixel b-layer, the so called IBL.

The principle motivation is to provide an increased tracking performance under high-luminosity conditions [7]. This is necessary as the tracking performance of the current pixel detector will decrease on account of the radiation damages.

The IBL was inserted inside the existing pixel detector package. As shown in figure 2.11 there is no space between the old beam pipe and the pixel detector. For this reason the IBL is mounted on a new beam pipe with a smaller radius of 3 cm. To prepare the pixel detector for this and to renew services it was extracted from the ATLAS detector in 2013 and brought to the surface. At the beginning of 2014 the services were replaced

¹⁵Letter Of Intent

2. The LHC and the ATLAS Detector

and the pixel detector was inserted to ATLAS again. The IBL contains 14 staves and with an outer envelope of 40 mm it fits within the existing b-layer.

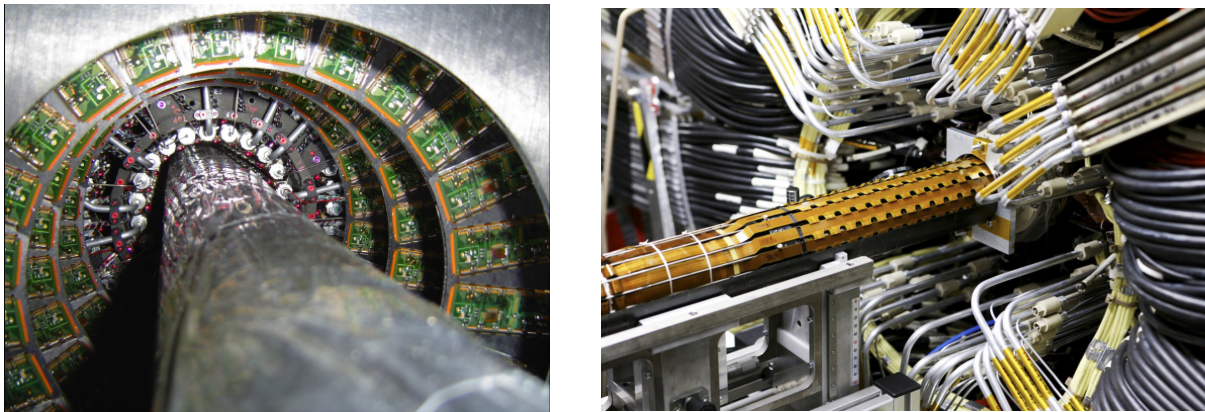


Figure 2.11.: A photo of the pixel detector surrounding the beam pipe during the integration in SR1 (left) [8] and a photo of the insertion of the IBL mounted on a new beam pipe with reduced radius (right) [9]

These mechanical constraints and the extremely close position to the beam pipe set some general requirements to the IBL sensor and read out chip:

- Radiation hardness:
 - The sensor has to operate stable after a non ionizing energy loss fluence of $5 \cdot 10^{15} \text{ n}_{eq} \text{ cm}^{-2}$. The maximum depletion voltage after this fluence should be 1000 V and the global hit detection efficiency has to be above 97 % within the active area for each module.
 - The readout electronic will be the FE-I4 (see section 4.4) and it has to withstand a total ionizing dose of 250 Mrad.
- Requirements concerning the geometry of the IBL:
 - Because of the extreme spatial constraints the modules of the IBL cannot be shingled on the staves. To get a geometric efficiency of about 97 % the inactive edges of each sensor should be less than $225 \mu\text{m}$. This means that the geometric inefficiency of the sensor, caused by its inactive edge, has to stay below 2.2 %. Details to the IBL planar sensor design are given in 4.3.
- General requirements to the sensor:
 - The pixel size should be $250 \mu\text{m} \times 50 \mu\text{m}$ and arranged in a matrix of 336 rows times 80 columns. This dimensions are given by the pixel size of the front end electronic.
 - The maximum power dissipation of 200 mW/cm^{-2} at 1000 V depletion voltage due to the limited cooling power. Most of the power dissipation is caused by the front end chip. The leakage current per pixel should be less than 100 nA.
 - The sensors have to operate stable at a sensor temperature of $-15 \text{ }^\circ\text{C}$.

There are two different sensor layouts for the IBL that fulfil these requirements. The planar silicon pixel sensor is described in detail in section 4.3.

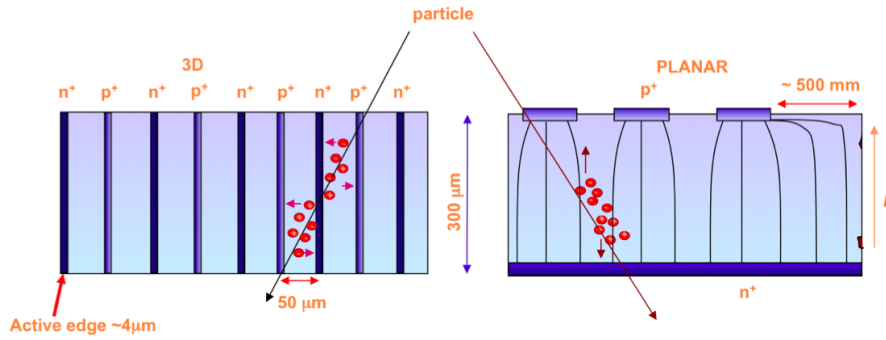


Figure 2.12.: Difference in particle detection of a 3D silicon sensor (left) and a planar sensor (right) [10]

Instead of depleting the entire bulk between the electrodes it is possible for 3D sensors to create electrodes within the silicon bulk via DRIE¹⁶ [11]. The 3D detector technology allows a lower bias voltage to fully deplete the sensor and a small electrode pitch with short collection times.

Two different manufacturers process the 3D sensors for the IBL: FBK¹⁷ and CNM¹⁸. The process at CNM and FBK is mainly similar and the wafers consist of p-type high resistivity silicon. Both use the double sided etching technique called Bosch-process, an important difference between these technologies are the active edges.

Further information on 3D sensors can be found in [12].

Each of the 14 IBL local support structures, staves, are made of low density carbon foams and carries 12 planar Double Chip Modules (DCM) and 8 3D Single Chip Modules (SCM). The location of the different sensors on the staff is shown in figure 2.13. One planar n⁺-in-n Double Chip Sensor is read out via two FE-I4 chips. The staves provides for the 32 FE-I4 read-out chips and the sensors a CO₂ evaporative cooling.

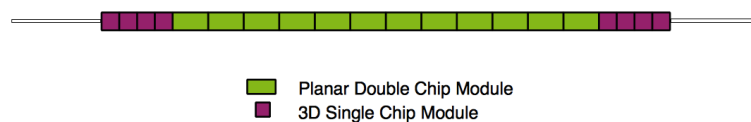


Figure 2.13.: Sketch of the sensor positions on staff.

¹⁶Deep Reactive-Ion Etching

¹⁷Fondazione Bruno Kessler, Povo di Trento, Italy

¹⁸Centro Nacional de Microelectronica, Barcelona, Spain

3. Radiation damage in silicon

The innermost layers of the ATLAS detector have to withstand fluences of up to $2 \cdot 10^{16} n_{eq} cm^{-2}$ after the upgrade to HL-LHC¹.

Defects induced by radiation influence characteristics of a detector, such as: effective doping concentration, leakage current, and charge collection efficiency. Further information about radiation damage in silicon can be obtained in [15] and [25].

3.1. Crystal Defect Types

High energy particles lose energy while traversing the detector not only by ionization, which is fully reversible, but also by NIEL².

The primary particle removes a lattice atom, the so called PKA³, and so becoming an interstitial atom and leaving behind a lattice vacancy. Any damage induced change in the material scales linearly with the energy transferred in the collision. With the NIEL scaling hypothesis it is possible to calculate and compare radiation damage induced by different particles and energies. The incoming radiation is normalized to a mono-energetic 1 MeV neutrons and the fluences are given in n_{eq}/cm^2 .

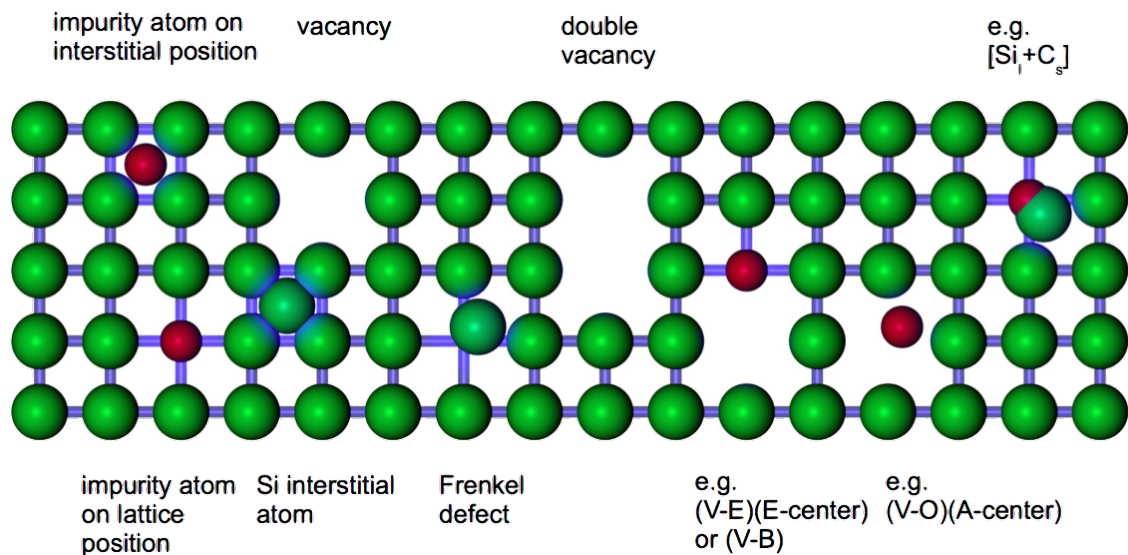


Figure 3.1.: Schematic illustration of different crystal defects [20]

¹High Luminosity LHC

²Non Ionising Energy Loss

³Primary Knock-on Atom

3. Radiation damage in silicon

Figure 3.1 shows the most common complex damage formations:

Interstitials and Vacancies:

These defects have no fixed lattice position at room temperature. They can form stable formations with other defects and anneal if they meet.

Frenkel defect:

A defect formed by an interstitial near a vacancy. The charge state of it may be either negative, positive, or neutral.

Double vacancy:

Two vacancies, i.e. a divacancy. This can have any charge state between double negative and single positive.

A-center:

Oxygen is not only a remnant from the crystal-growing process but is also added to increase radiation hardness (more informations given in [26]). If it forms a vacancy-oxygen complex it can act as an acceptor and a trapping center.

E-center:

For n-type Silicon, Phosphorus is used as a donor. If it forms a vacancy-phosphorus complex and in doing so loses a covalent bonding.

3.2. Type inversion

Higher radiation has increasing influence on the doping concentration. The removal of charge carriers can lead to a type inversion.

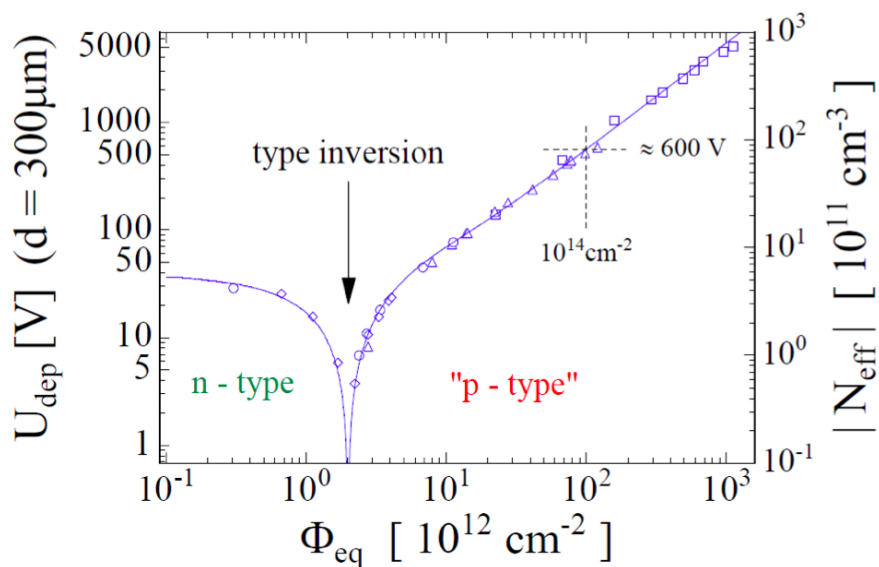


Figure 3.2.: Effective doping concentration is dependent on the fluence, which is shown in a neutron equivalent dosage [27]

The effective doping concentration changes from positive to negative, converting an n-type doped material to a p-type like material. Displacement damages act like acceptors, thus increasing the acceptor concentration N_A while decreasing the donor concentration N_D through donor removal due to defects in the crystal lattice. After a defined radiation dose, N_{eff} reaches a minimum and increases again. At this moment the bulk has changed from originally n-type to p-type. The fluence at which type inversion occurs depends on the initial doping concentration. This dependency and the influence on the depletion voltage is shown in figure 3.2. The influence of the effective doping concentration on the depletion voltage is given in:

$$V_{depl} = \frac{e_0 |N_{eff}| d^2}{\varepsilon_{Si} \varepsilon_0} \frac{1}{2} \quad (3.1)$$

with

$$N_{eff} = N_D - N_A. \quad (3.2)$$

As a result of this equation, higher fluences lead to an increasing depletion voltage. At a certain effective doping concentration, the sensor has to be operated partly depleted because it cannot be fully depleted safely.

3.3. Annealing

As already mentioned the effective doping concentration N_{eff} depends on the irradiation of the sensor. Not all defects generated by radiation are permanent or stationary. It changes with respect to temperature and time after the irradiation, this behavior is the so called annealing. Moving defects can form new complex defects or they can recombine and recover the damage.

The Hamburg model characterizes the effects of annealing through equation 3.3, N_{eff} is composed of three different components [25, 26].

$$\Delta N_{eff}(\phi_{eq}, t(T_a)) = N_a(\phi_{eq}, t(T_a)) + N_c(\phi_{eq}) + N_y(\phi_{eq}, t(T_a)) \quad (3.3)$$

N_a is the so called short-term annealing or beneficial annealing. It increases the effective doping concentration which leads to a lower depletion voltage for type inverted n⁺-in-n sensors. The reverse annealing N_y increases with time while N_A decreases. On a long time scale reverse annealing surpasses the beneficial annealing thus decreasing N_{eff} and increasing the depletion voltage. The stable damage N_c is not depending on annealing but only on the fluence. It consists of a so-called *incomplete donor removal*. This depends exponentially on the fluence with a final value of N_{C0} and in addition a fluence proportional introduction of *stable acceptors*:

$$N_C = N_{C0}(1 - \exp(-c\phi_{eq})) + g_C\phi_{eq} \quad (3.4)$$

Figure 3.3 shows the annealing behaviour and the three different annealing components. To avoid an uncontrolled annealing, irradiated sensors are stored and operated at low temperatures.

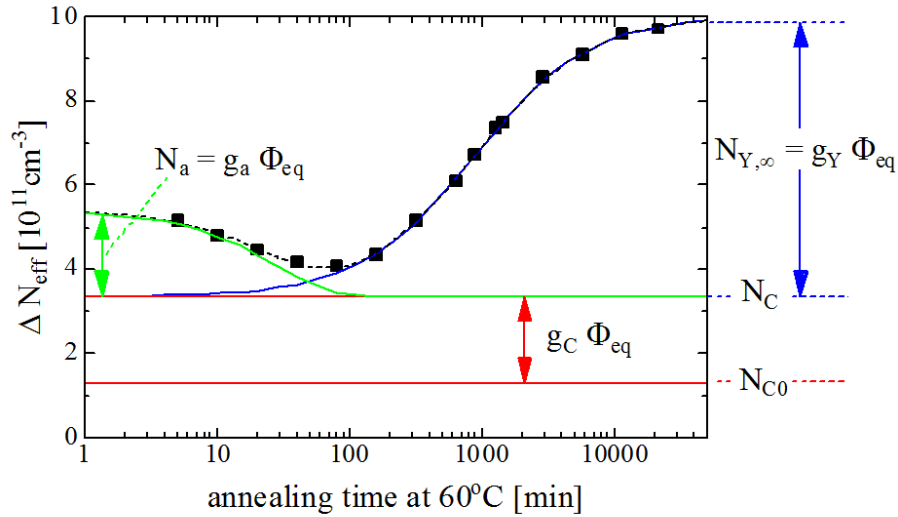


Figure 3.3.: Change of the effective doping concentration in dependence of the annealing time at a temperature of 60°C [25]

3.4. Leakage Current

The leakage current is the current remaining in the static reverse bias mode; mostly driven by charge carriers generated by crystal impurities within the depleted region. This current scales strongly with temperature T and with the size of the band gap E_g and can be described with:

$$I(T) \propto T^2 \exp\left(\frac{-E_g}{2k_B T}\right) \quad (3.5)$$

To compare and analyze leakage current measurements at different temperatures it is possible to normalize the current with equation 3.5.

$$I_0 = I \cdot \left(\frac{T_0}{T}\right)^2 \exp\left[\frac{-E_g}{2k_B} \cdot \left(\frac{1}{T_0} - \frac{1}{T}\right)\right] \quad (3.6)$$

The leakage current is also proportional to the fluence. This dependence is shown in figure 3.4 and is given by:

$$I = \alpha \cdot \phi_{eq} \cdot V \quad (3.7)$$

V is defined as the volume of the sensor that is depleted while α denotes the current related damage rate.

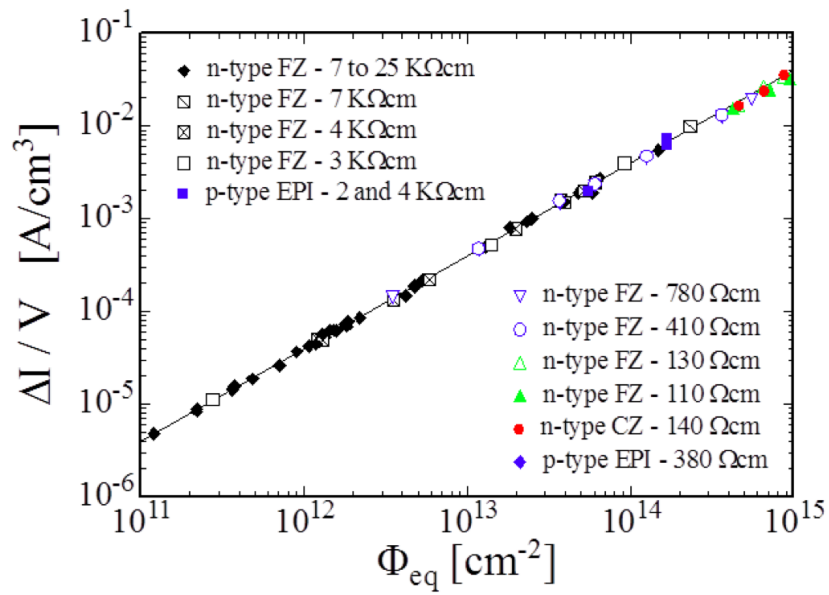


Figure 3.4.: Fluence dependence of the leakage current. Measurements were taken after 80 minutes annealing at 60°C [25]

4. ATLAS Pixel Sensors

This chapter gives an overview of the principles of silicon particle detectors and the functionality, and design, of the Pixel and IBL ATLAS sensors and assemblies.

4.1. Principles of Silicon Particle Detectors

Different particles interact with matter in dissimilar ways. Their signature in matter is determined by their charge, mass, and energy. In the following the energy loss of different particles in matter will be described as well as the general design of semiconductor sensors.

4.1.1. Energy Loss of Photons in Matter

Photons interact with matter mainly in three different processes. Up to an energy of 60 keV the photoelectric effect is dominant for silicon. At energies above 2 MeV the pair production is dominant. In between these energies the Compton scattering process is dominant.

Photoelectric Effect

The photoelectric effect describes a photon being absorbed completely by an atom. The excitation energy is used to excite an electron with a kinetic energy of E_{kin}^{e-} . This is equal to the energy of the photon E_γ minus the bond energy of the emitted electron E_{bin} .

$$E_{kin}^{e-} = E_\gamma - E_{bin}$$

Compton Scattering

The Compton effect describes the inelastic scattering of a photon with a quasi free outer shell electron of an atom. The energy of the photon is fractionally absorbed by the electron. This causes a change in the wavelength of the photon.

The quotient of the energies before and after the scattering is proportional to the incident photon energy scaled by a cosine of ϕ which describes the angle between an incoming and outgoing photon: the larger the angle, the larger the energy loss:

$$\Delta\lambda = \frac{h}{m_e c} (1 - \cos\phi) = \lambda_C (1 - \cos\phi) \propto E(1 - \cos\phi)$$

The factor $\lambda_C = h/m_e c$ is the Compton wavelength of an electron.

Pair Production

The pair production is the creation of an electron-positron pair by a single photon which interacts with an atomic nucleus. The energy of the photon needs to be at least equal to the rest energy of the electron-positron pair and even higher. The threshold energy is

$$E_{min}^{\gamma} = 2m_e \left(1 + \frac{m_e}{M}\right)$$

m_e : rest mass of an electron

M : mass of involved nuclei

4.1.2. Energy Loss of Charged Particles in Matter

When charged particles with a mass above the electron mass traverse matter, the main process of losing energy is ionisation. The amount of energy lost per distance travelled can be calculated using the Bethe-Bloch formula [13]:

$$-\left(\frac{dE}{dx}\right) = 2\pi N_a r_e^2 m_e c^2 \rho \frac{Z}{A} \frac{z^2}{\beta^2} \left[\ln \left(\frac{2m_e \gamma^2 v^2 W_{max}}{I^2} \right) - 2\beta^2 - \delta - 2\frac{C}{Z} \right] \quad (4.1)$$

$\frac{dE}{dx}$: mean energy loss per track length

N_a : Avogadro constant = $6.022 \cdot 10^{23} \text{ mol}^{-1}$

r_e : classical radius of an electron = $2.818 \cdot 10^{-15} \text{ m}$

m_e : mass of an electron = 511 keV

c : speed of light = $3 \cdot 10^8 \text{ m s}^{-1}$

ρ : density of absorbing material = 2.33 g cm^{-3}

Z : atomic number of the medium $Z_{Si} = 14$

A : atomic weight of the medium $A_{Si} = 28.09$

z : charge of penetrating particle in units of e_0

β : velocity of penetrating particle in units of c

γ : $\gamma = 1/\sqrt{1-\beta^2}$

I : effective ionisation potential of the medium $I_{Si} = 137 \text{ eV}$

δ : density correction

C : shell correction

W_{max} : maximum energy transfer in a single head on head collision

The Bethe-Bloch formula has a minimum at $\beta\gamma = 3.5$ which fits to an energy loss of $\approx 1.5 \text{ MeV cm}^2 \text{ g}^{-1}$ (Fig. 4.1). Particles with kinetic energies above that minimum are called minimum ionising particles (MIP).

Besides the energy loss described by the Bethe-Bloch formula, electrons can lose their energy via Bremsstrahlung. Electromagnetic radiation is produced when charged particles are accelerated. When an electron is scattered in the electrical field of nuclei, the produced radiation is called Bremsstrahlung. Due to the small mass of electrons the Bethe-Bloch formula does not include Bremsstrahlung.

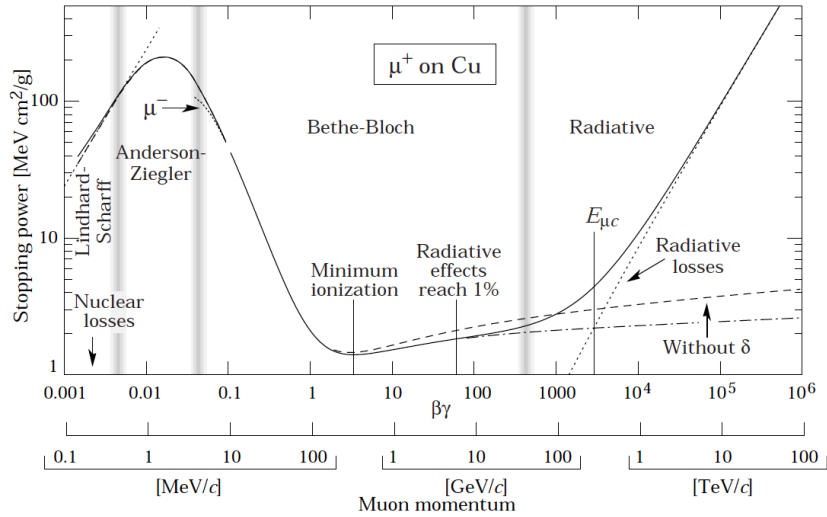


Figure 4.1.: Stopping power of muons in copper as function of $\beta\gamma = p/MC$ [14]

4.1.3. Intrinsic and Extrinsic Semiconductors

A semiconductor is a solid and its resistance decreases with increasing temperature. The material for semiconductors can be classified in intrinsic and extrinsic semiconductors [15].

A crystal is intrinsic if it is without or just with a negligible amount of impurities. As can be seen in figure 4.2 an intrinsic semiconductor implies an equal number of electrons and positive states, also called holes. This is a disadvantage because of the temperature dependence of the charge carrier density. This problem is solved in an extrinsic semiconductor by doping and inserting impurities by purpose. The most common dopants are atoms from the III. (e.g. boron) or from the V. (e.g. phosphorus) main group of the periodic system of the elements.

Boron leads to additional holes in the crystal since these atoms are not able to form bonds with all their neighbours. Silicon that is doped in this way is called p-type silicon. Phosphorus is inserted into the crystal lattice of n-typed silicon and replaces silicon atoms. The covalent bonding of phosphorus inside the lattice has one extra electron which is only bounded loosely. Both dopings are shown in figure 4.2.

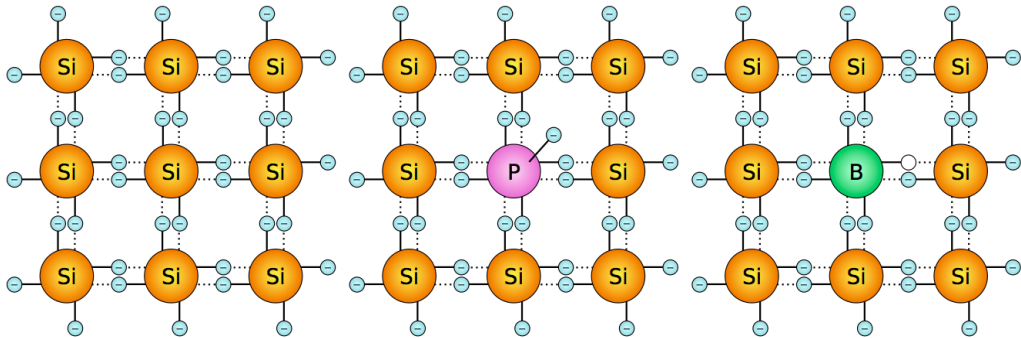


Figure 4.2.: **Left:** The silicon lattice cell shows undoped silicon and has no impurities. **Middle:** This cell shows n-doped lattice with one loosely bound extra electron. **Right:** This cell illustrates a p-doped silicon lattice with one electron less. [16]

4.1.4. The pn-Junction

To detect the signal of a particle traversing the sensitive layer, the material needs to be depleted. This means that the silicon is ideally depleted of free charge carriers. To be able to create a depletion zone a p-n-junction in the material is required. This is realized by merging p-doped silicon with n-doped silicon. Due to the concentration gradient, electrons from the n-side diffuse to the p-side and recombine with holes. The holes from the p-side diffuse to the n-side and recombine with electrons. From this recombination a naturally slim depletion zone is formed. By applying an external voltage in reverse bias mode the potential drop between the n-doped and the p-doped region can be increased. The depletion zone grows through the bulk towards the other side (4.3). The voltage at which the bulk is fully depleted and the complete signal created by an incident particle can be detected, is called depletion voltage V_{depl} . The depletion voltage is proportional to the doping concentration and depends on the bulk thickness and the bulk resistivity [17].

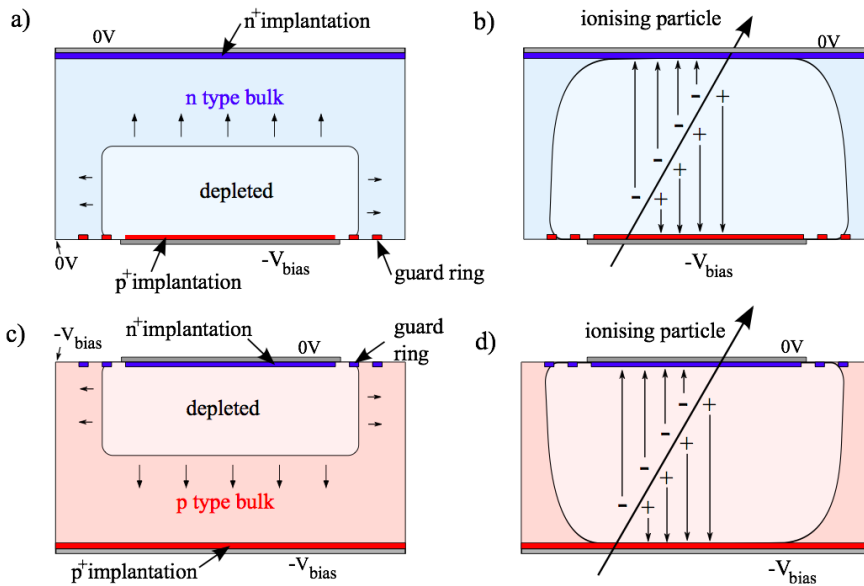


Figure 4.3.: Cross section through a silicon sensor with depletion growth for a n-type bulk (a and b) and a p-type bulk (c and d) [18]

4.1.5. Float Zone and Magnetic Czochralski Silicon

This thesis give attention to two different silicon types: DOFZ¹ and MCz². The names of the silicon types arising from the respective process of production.

The typical oxygen concentration of FZ is about 10^{15} cm^{-3} it can be enriched in a 24 hours process with oxygen up to a concentration of 10^{17} cm^{-3} . The oxygen concentration of MCz is $10^{17} - 10^{18} \text{ cm}^{-3}$. As can be seen in equation 3.1 the depletion voltage depends on N_{eff} . Oxygen enriched FZ needs, after proton and pion irradiation, less depletion voltage than standard FZ (see figure 4.4). All n⁺-in-n ATLAS sensors are made out of DOFZ material.

¹Diffusion Oxygenated Float Zone

²Magnetic Czochralski

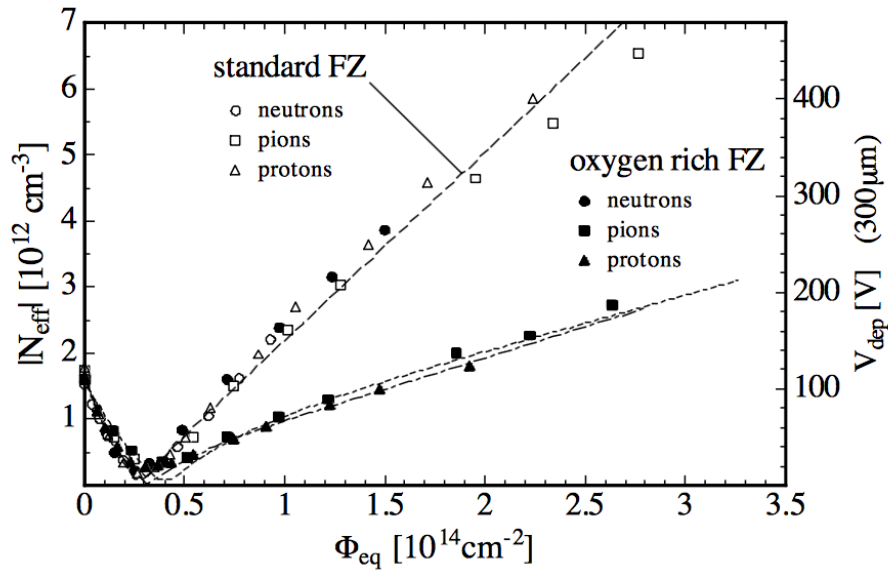


Figure 4.4.: Comparison of N_{eff} for standard and oxygen enriched Float Zone silicon after irradiation with neutrons, protons and pions [26]

4.2. ATLAS Pixel Sensor Modules

The smallest unit of the ATLAS pixel detector is the IBL module. Adding up all modules of all three Pixel layers and the six disks one gets 1744 modules in total. Each module consists of a sensor (4.2.1,) the so called tile, which is bump bonded (4.2.3) to 16 Front End chips of the type FE-I3 (4.2.2). 41,984 pixel per tile have a pixel size of $400\ \mu\text{m} \times 50\ \mu\text{m}$, the remaining pixels are called long pixels, with a pitch of $600\ \mu\text{m} \times 50\ \mu\text{m}$, they cover the $200\ \mu\text{m}$ gap between two FE chips. Further special pixel designs, the so called ganged pixels, are necessary in the outer rows of the sensor. The bare module is glued to a flex. The flex carries passive SMD³ components, a ceramic NTC⁴ thermistor for temperature measurement and the MCC⁵. The MCC is responsible for data processing and communication with the outer detector electronics. More information of the ATLAS pixel modules can be found in [19].

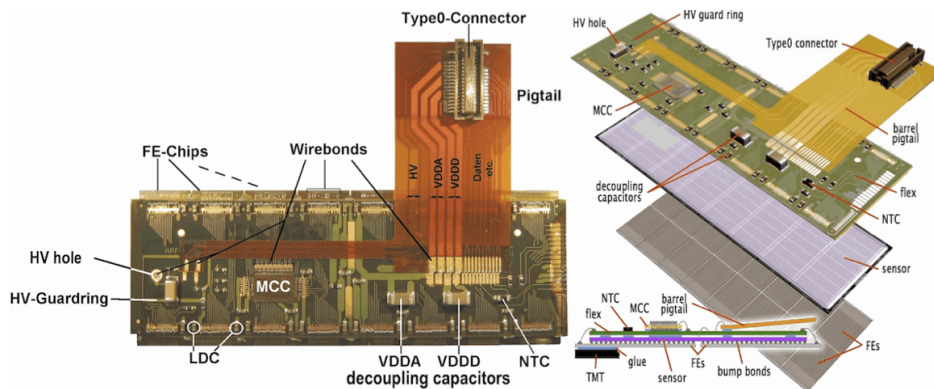


Figure 4.5.: Sketch of the FE-I3 based ATLAS pixel module [20]

³Surface Mounted Device

⁴Negative Temperature Coefficient thermistor

⁵Module Control Chip

4.2.1. ATLAS Pixel Sensor

The sensor of the current ATLAS pixel detector is a planar n^+ -in- n $250\ \mu\text{m}$ thick silicon sensor. It is processed on n -type doped DOFZ⁶ substrate material. An oxygen enrichment of silicon increases the radiation hardness in comparison to standard silicon. The n^+ -implantation is segmented into 2880 pixels with a $400\ \mu\text{m} \times 50\ \mu\text{m}$ pitch for a single pixel. One array of 18 columns and 160 rows are read out by one Front End I3 (FE-I3) chip.

A sketch of the cross section of the sensor bulk can be seen in figure 4.6. For the n^+ -in- n design it is necessary to do a double-sided wafer process since both sides of the wafer have to be structured. Each surface consists of five layers:

- n^+ / p^+ -implantation
- oxide passivation
- inner nitride passivation
- metal (AlSi alloy)
- outer nitride passivation

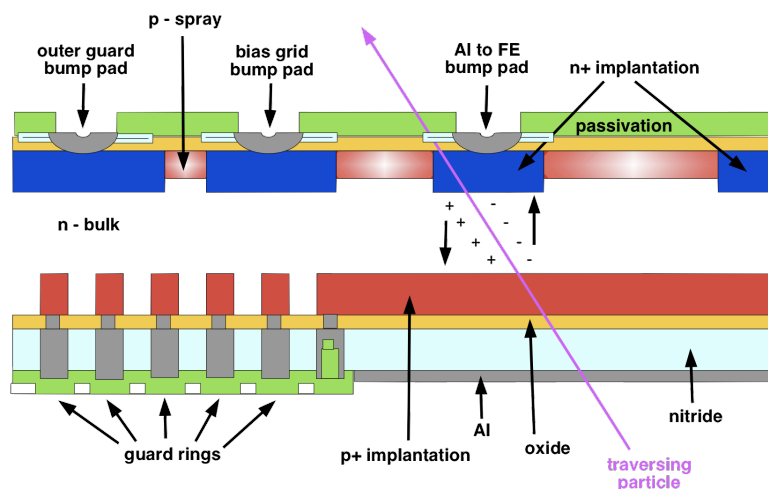


Figure 4.6.: Cross section of the ATLAS pixel sensor

For the present ATLAS pixel sensor design a moderated p-spray is used to insulate the n^+ -implantations. The p-doping is homogeneously spread over the complete sensor surface. For detailed information of the process steps see [21]. On the p-site is one large high voltage pad opposite of the pixel matrix. This site is surrounded by 16 guard rings. The intention of the guard rings is a controlled potential drop from the high voltage pad to the grounded cutting edge.

⁶Diffusion Oxygenated Float Zone

4.2.2. Front End I3

The Front-End chip is the readout part of a module. Each FE chip cell is bump bonded to a sensor pixel and features an analogue and digital part. The analogue part of the FE-I3 chip is shown in 4.7.

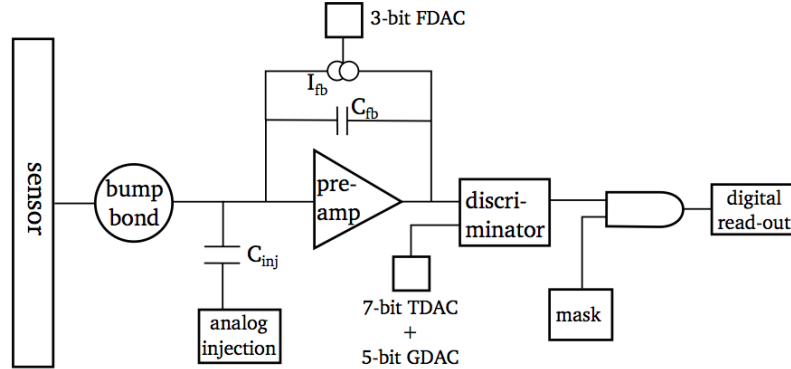


Figure 4.7.: Schematic of the analogue part of the FE-I3 chip, including a bump bond, the test circuits and the preamplifier and discriminator chain.[6]

The signal is emitted from the sensor. A preamplifier amplifies the signal and charges the feedback capacitor which is discharged by a constant current. The general functionality of front end electronics and especially for the FE-I4, which is the succession of the FE-I3, is described in section 4.4.

4.2.3. Bump Bonding

The bonding between each pixel cell of the sensor with one cell of the Front-End chip is done via so called bump bonds. For the ATLAS IBL production was the vendor the IZM⁷, who use tin-silver bumps. A sketch of the process is seen in figure 4.8. Before this process it is necessary to prepare the pads of the sensor with additional metal layers, the UBM⁸. They are applied onto the passivation openings to achieve a good mechanical and electrical contact for the bumps. The UBM is electro-plated and consists of copper, nickel and gold. The bump bond is applied on the pads of the chip and consists of a eutectic alloy of 96.5% tin and 3.5% silver. The bump is a 20 μm high cylinder, after a reflow step at 240°C it becomes a sphere. The interconnection step between sensor and chip is called the flip chip process.

A detailed description of different bump bonding processes can be found in [13].

4.3. IBL Sensors

The wafer material is, like for the ATLAS pixel sensors, n-doped DOFZ silicon with a resistivity of 2 to 5 $\text{k}\Omega\text{cm}^{-1}$. The material is 200 μm thick. The production wafer has a diameter of four inches and holds two DCS and several test structures. More information about the wafer layout can be found in [6].

⁷Fraunhofer Institut für Zuverlässigkeit und Mikrointegration

⁸Under Bump Metalisation

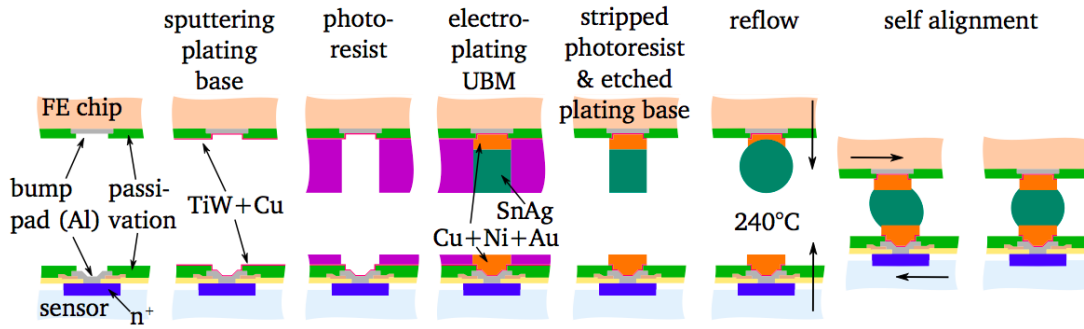


Figure 4.8.: Tin-silver bump bonding process [6]

Based on the ATLAS pixel sensor design modifications were made for the IBL sensor. The sensor and pixel geometries were changed to be compatible with the new readout electronics, the FE-I4. The pixel size is only $250\ \mu\text{m} \times 50\ \mu\text{m}$ which results in a better z-resolution of the detector along the beam pipe. The IBL consists of 2×1 DCS-Modules (one sensor is read out by two FE-I4 chips). A picture of one DCS is shown in 4.9 with the dimensions of the active area. The inner edge sensor pixels are extended to $450\ \mu\text{m}$ to bridge the gap between the two readout chips.

As mentioned in section 2.4.1 it is not possible to shingle the staves for the IBL. For the IBL design the inactive edge distance between the pixel matrix and the cutting edge was shrank to below $450\ \mu\text{m}$. Figure 4.10 shows a comparison between the conservative edge design of the ATLAS pixel sensors and the new slim edge design of the IBL sensors. For the IBL design the outermost pixels are extended to $500\ \mu\text{m}$ length and the innermost eleven guard rings are placed over the outermost half of the edge pixel implants. This is possible for n^+ -in-n sensors as guard rings are on the opposite side of the pixel implants.



Figure 4.9.: Picture of a IBL Double Chip Sensor with the dimension of the active area.

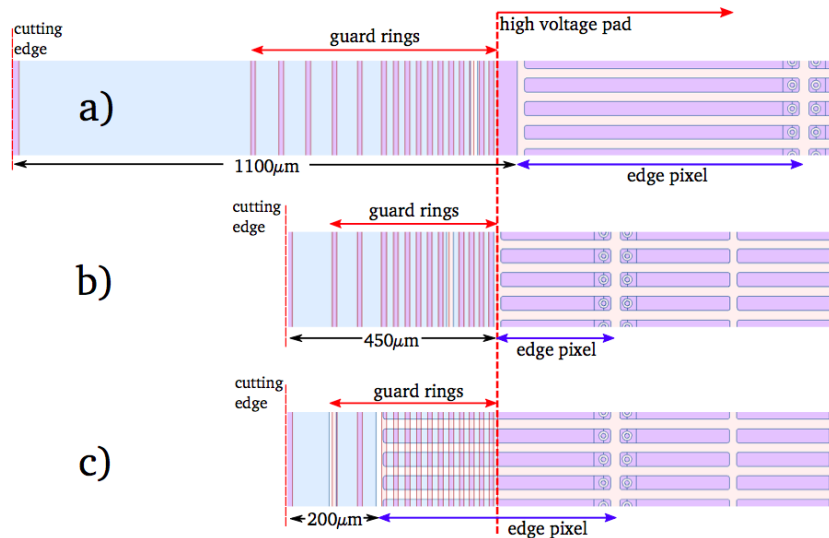


Figure 4.10.: a) Edge region of the ATLAS pixel design b) the conservative design and c) the slim edge IBL design. The inactive edge could be reduced from $1100\ \mu\text{m}$ to $200\ \mu\text{m}$. [6]

4.4. Front End I4

For the ATLAS upgrades a new front end was developed to improve resolution, performance, and radiation hardness of the pixel detector [22].

To increase the radiation hardness the FE-I4 is built in a 130 nm CMOS⁹ feature size technology using thin gate oxide transistors. The dimension of the new chip in comparison to the FE-I3 can be seen in figure 4.11. It has an active area arranged in 80 columns on a $250\ \mu\text{m}$ pitch by 336 rows on a $50\ \mu\text{m}$ pitch and 2 mm periphery. This results in an active over inactive area fraction of about 90% (this is for the FE-I3 <75%).

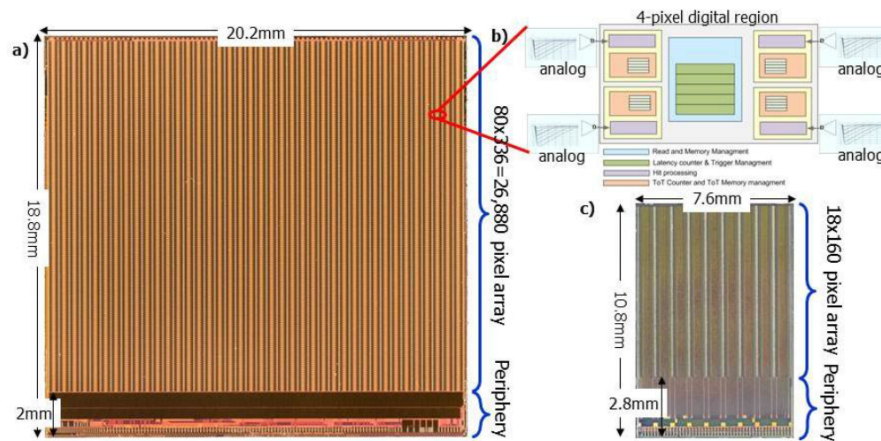


Figure 4.11.: a) Picture and dimensions of a FE-I4. b) Zoom into a 4-pixel region with separated analogue circuits and a combined digital region. c) Picture and dimensions of the current ATLAS readout chip FE-I3 [23]

Each pixel of the FE chip holds an analogue and a digital circuit. The sensor signal

⁹Complementary Metal Oxide Semiconductor

is amplified and digitized in the analogue part and the hit processing is done in the digital part. The digital pixel array is revised in comparison to the FE-I3. Hits are stored in a 4-pixel digital array until the trigger signal arrives and not in the periphery as in the FE-I3.

Figure 4.12 shows a schematic view of the analogue pixel cell. The signal is amplified in two stages, a fast preamplifier and a second amplifier are AC coupled. The feedback currents of both amplifiers are adjustable. The global feedback current, which means that all pixels of the matrix are concerned, is set by the 8-bit $PrmpVbpf$. To be able to tune the ToT^{10} for each pixel individually there is a 4-bit in-pixel adjustment, the so called FDAC¹¹. There is a 5-bit TDAC¹² setting for the adjustment of the threshold for each pixel. The global threshold can be controlled via the value $Vthin_Alt$, which consists of two 8-bit values for a fine and a coarse adjustment.

The discriminator compares the signal with the threshold, if the signal is higher than the threshold the output is a logical one and the pixel sees a hit, if it is lower than the threshold there is no output from the discriminator. Figure 4.13 shows the signal in dependency of the DAC values. Further details of the FE-I4 can be found in [24] and [22].

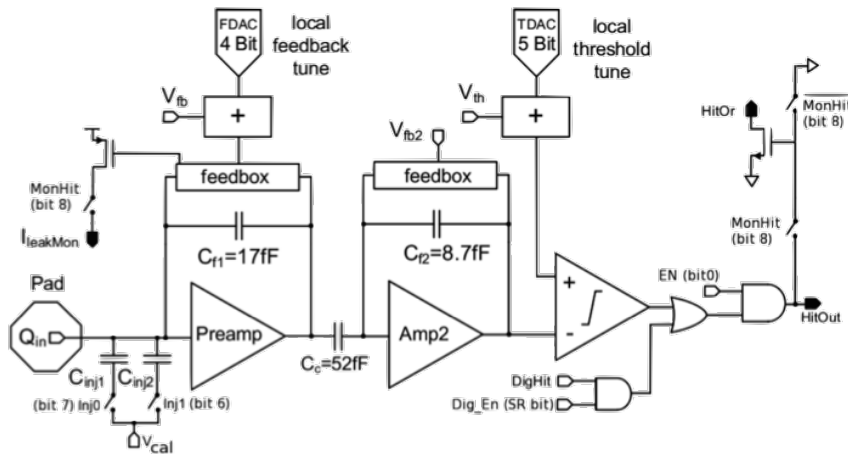


Figure 4.12.: Schematics of the analog pixel circuit [24]

4.5. FE-I4 Single Chip Assembly

The FE-I4 Single Chip Assembly (SCA) consists of a single chip sensor connected via bump bonds to a front-end chip. An SCA is half the size of a DCM and has same kind of test structure: FE-I4 sized single chip sensors, which are produced on a wafer. In order to test the performance and efficiency of this SCA in the laboratory or in the testbeam (more information in section 6) it is connected via wirebonds to a readout card which can be connected with a ribbon cable to the USBpix readout system. This is described in detail in 5.3.1.

¹⁰Time over Threshold

¹¹Feedback-current Digital to Analog Converter

¹²Threshold Digital to Analog Converter

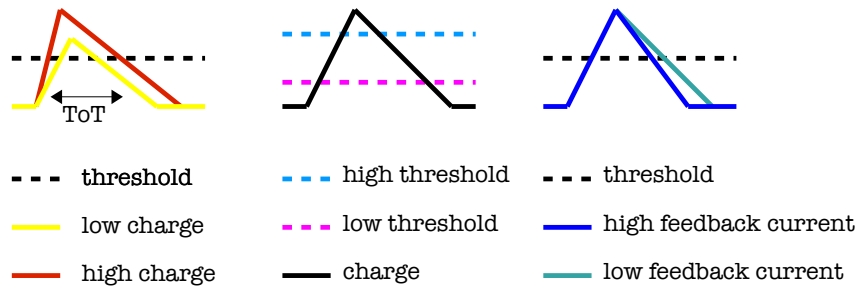


Figure 4.13.: Preamplifier output signals in dependent on the chip DAC values and input charge. (Figure adapted from [19])

5. Methodology

5.1. Measurement of IV Characteristics

The leakage current as a function of the applied bias voltage, the so called IV-curve, is an important tool in sensor investigation.

The measurement itself was done via the lemo connector of the SCC with an *iseg SHQ 222M¹*. A typical IV - curve of an unirradiated FE-I4 sensor is shown in figure 5.1. As described in 3.4, the leakage current is a function of temperature and fluence. The impact of the temperature is shown in figure 5.2. The leakage current is measured at a stable bias voltage of -500 V and the temperature range goes from -15°C to -45°C.

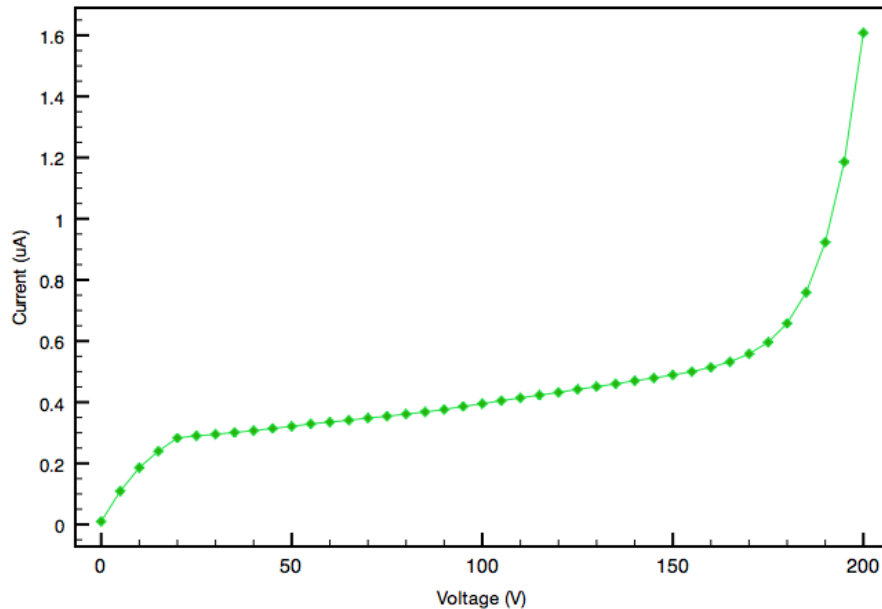


Figure 5.1.: IV-Curve of an irradiated sensor at room temperature.

5.2. Irradiation Sites

Five irradiation facilities were used to investigate the radiation damage that occurs during the operation of the ATLAS detector. The irradiation facilities differ in the energy and the particle type that is used for the irradiation, to normalise the measurements a 1 MeV neutron is typically used. The measured hardness factor for every irradiation facility is used to express the radiation damage in term of the 1 MeV neutron equivalent fluence.

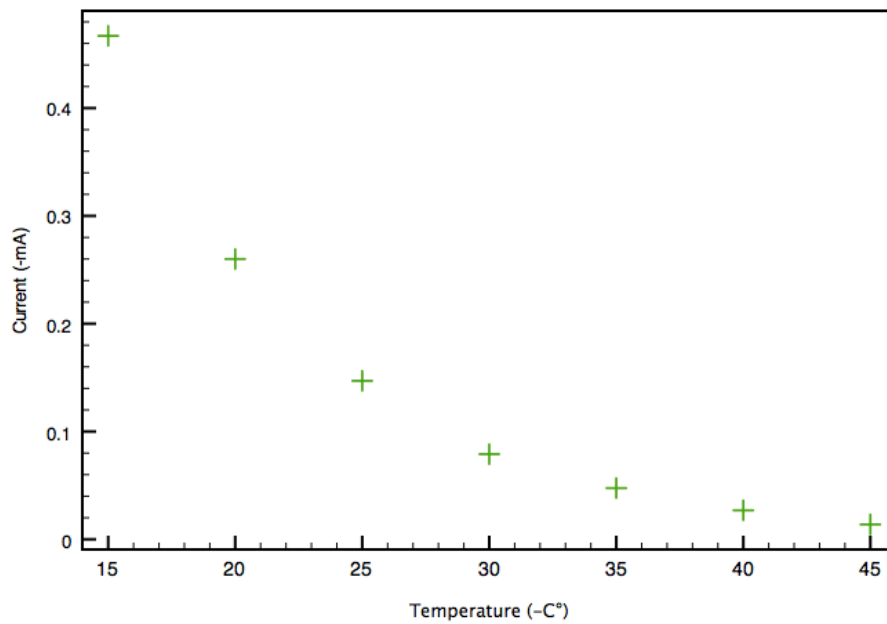


Figure 5.2.: Current-Temperature curve of an irradiated sensor at a bias voltage of -500 V.

JSI-Triga in Ljubljana

The reactor centre of the Jozef Stefan Institute (JSI) in Ljubljana offers the possibility for irradiations with reactor neutrons having a continuous energy spectrum. The Neutrons have an energy above 100 keV and a hardness factor of 0.9. Since the size of the device under test is limited and shielding is difficult in the reactor environment only bare sensors or assemblies can be irradiated.

The irradiation of FE-I4 assemblies is problematic since tantalum contained in the read-out chip is activated during irradiation and thus the assemblies cannot be handled without severe radiation protection for several months. The dosimetry is obtained indirectly from the known flux of the reactor, which is periodically calibrated by measuring the leakage current of silicon diodes.

Irradiation Center in Karlsruhe

An irradiation with low energy protons with an energy of 23 MeV can be done by a cyclotron at the Karlsruher Institut für Technologie (KIT). The protons are delivered with a typical beam current of $9 \cdot 10^{12}$ p/cm²/s. The beam spot has a size of 7 mm but a scanning table allows homogeneous irradiation of bigger samples. The hardness factor is 2.0. During the irradiation the samples are cooled to prevent annealing. The dosimetry is measured over the activation of the ⁵⁷Ni activity in a Ni foil.

CERN-PS in Geneva

For the irradiation with high energy protons the CERN PS irradiation facility is used. The momentum of the protons is 24 GeV and the flux reaches $(2-9) \cdot 10^9$ p/cm²/s. The combination of this and the hardness factor of 0.62 leads to long irradiation times.

[29] The diameter of 2 cm of the beam allows to irradiate samples up to a size of 2 cm without scanning over it. The dosimetry is measured over the activation of an Al foil, a NaI or Ge spectrometer.

LANSCE in Los Alamos

Protons with 800 MeV are available through the LANSCE² [30]. The beam spot size is about 2 cm so that even for FE-I4 assemblies no scanning of the beam over the sample is needed. The flux is about $1.5 \cdot 10^{12}$ p/cm²/s and the hardness factor is 0.71. During the irradiation it is not possible to cool the assemblies.

PSI in Villingen

An irradiation with 300 MeV pions is possible at the PSI³ in Villingen, Switzerland. The pion beam had a flux corresponding to 10^{14} pions/cm²/day. The hardness factor for this irradiation is 1.11.

5.3. Operation of FE-I4 ATLAS ReadOut Chips

In section 4.4 an introduction and principles of the operating mode of a FE-I4 is given. In this section the read-out system USBPix and the STControl program is described (5.3.1). The tuning routine and standard scans for the characterisation of a single chip assembly are introduced (5.3.2).

5.3.1. USBpix ReadOut-System and STControl

The USBpix hardware is based on a multi-purpose FPGA⁴ card, called Multi-IO board. It is usable with an FE-I3 or a FE-I4 adaptercard. The entire system, along with an FE-I4 single chip assembly, is shown in 5.3.

The Multi-IO board contains a microcontroller with an USB2.0 interface which establishes the data transfer to a PC, a high-speed device conforms to the USB2.0 specifications, an EEPROM⁵ for storing the microcontroller firmware, a free programmable Xilinx FPGA to provide logical and sequential functionality through 391 user IO's, a asynchronous SRAM⁶ to extend the internal FPGA memory capability with 16 Mbit SRAM and a programmable clock generator which provides a clock signal from 80 kHz to 150 MHz attached to the FPGA. The card needs to be powered with 5 V, this is possible via an external power supply or directly via USB. The options can be chosen by a solder jumper (P2).[31]

The adapter cards which were directly connected to the Multi-IO board own some support logic and bias voltage regulators for the front end. The regulators are powered

²Los Alamos National Laboratory spallation neutron sources

³Paul Scherrer Institut

⁴Field Programmable Gate Array

⁵Electrically Erasable Programmable Read-Only Memory

⁶Static Random Access Memory

5. Methodology

with 2V VDDA⁷ and VDDD⁸ the output voltage of the regulators can be set from a PC.

The assemblies can be tuned and operated by means of the software STcontrol⁹. How to tune an assembly to operate and characterize it under certain conditions is described in 5.3.2.

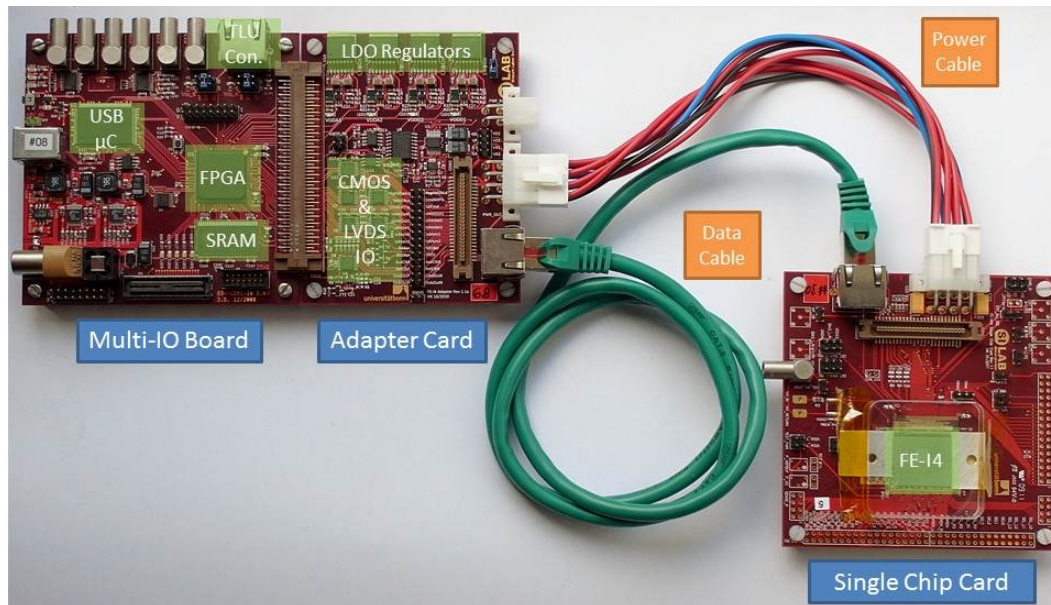


Figure 5.3.: Picture of the USBpix readout system [32]

5.3.2. Tuning and Standard Scans

With the USBPix system and STControl it is possible to calibrate and tune the FE chip to a well understood threshold of the discriminator and ToT [33].

Every tuning step and scan is explained in detail in the next sections. The process for tuning the FE after the global parameters have been set is as follows:

- Analog and digital scans
- Threshold and ToT scans
- TDAC tune
- FDAC tune
- TDAC tune
- Threshold and ToT scans to confirm required results

Analog and Digital Scan

To test if the digital and the analog part of the pixel cell work one can run a Digital and an Analog Scan. A defined charge is injected 200 times into the discriminator (Digital

⁷Analog supply Voltage

⁸Digital supply Voltage

⁹System Test control; <http://icwiki.physik.uni-bonn.de/twiki/bin/view/Systems/UsbPix>

Scan) or the amplifier (Analog Scan) of each pixel via an external charge injection circuit. The digital and analog part of the pixel cell work as expected if the same number of events is read back as was injected. An example for an uniform output of a Digital and Analog Scan is illustrated as an example in 5.4 and 5.5.

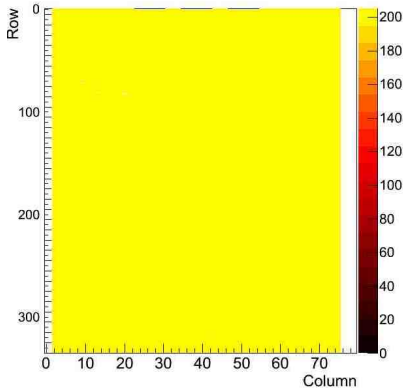


Figure 5.4.: Analog Scan of an unirradiated Single Chip Assembly

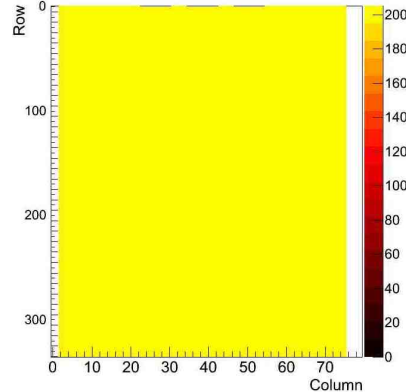


Figure 5.5.: Digital Scan of an unirradiated Single Chip Assembly

Threshold Scan and Tuning

The discriminator in the pixel cell compares the signal from the sensor to an adjustable threshold. The determination and the tuning of this threshold can be done with the "Threshold Tuning" and "Threshold Scan".

Threshold Scan: During this scan a charge is injected into the analogue part of the FE multiple times. This charge is adjusted by the *PlsrDAC*. Ideally the result should be a step function, no hits if the injected charge is below the threshold and if it is above the threshold the number of the injections is equal to the number of hits. A result of a threshold scan for one pixel is shown in figure 5.6. It is fit with a convolution of a step function and a Gaussian function and the hit probability can be described with:

$$p_{hit}(Q) = \frac{1}{2} \text{Erfc} \left(\frac{Q_{thresh} - Q}{\sqrt{2}\sigma_{noise}} \right) \quad (5.1)$$

- **Q:** The charge of injected pulse, given in DAC units.
- **Q_{thresh} :** The charge which consists to the discriminator threshold.
- **Erfc:** The error function.

With a data viewer it is possible to plot the results of Q_{thresh} and σ_{noise} . An example for a threshold and noise plot of an unirradiated sensor is given in figure 5.7 and 5.8. These plots are stored after the scan in SCURVE_MEAN and SCURVE_SIGMA. A high threshold prevents a high rate of noise hits. Due to that the noise gets higher with lower thresholds. This is shown in figure 5.9

Threshold Tuning: As already mentioned in section 4.4 it is possible to adjust the global value of the threshold, *Vthin_Alt_Coarse* and *Vthin_Alt_Fine*. This can be done

5. Methodology

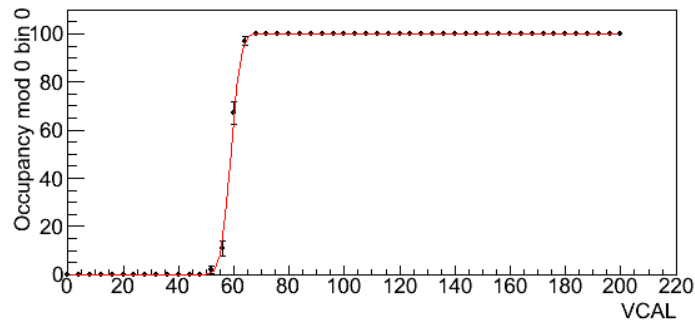


Figure 5.6.: Histogram of a threshold scan for one pixel.

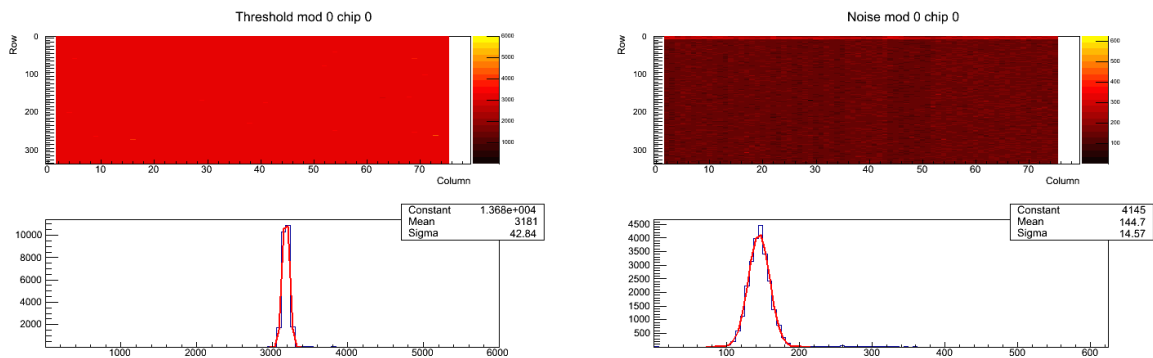


Figure 5.7.: Threshold scan of an unirradiated SCA.

top: Threshold map for every scanned pixel.
bottom: Threshold distribution of the hole SCA.

Figure 5.8.: Noise scan of an unirradiated SCA.

top: Noise map for every scanned pixel.
bottom: Noise distribution of the hole SCA.

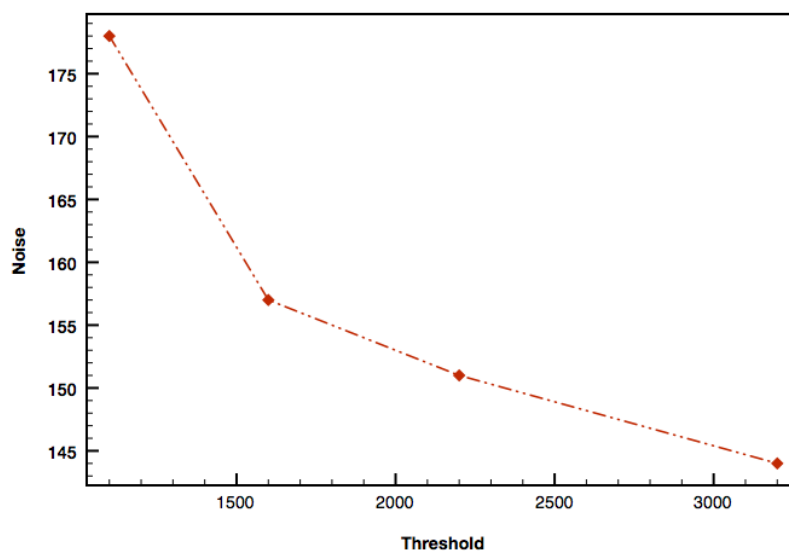


Figure 5.9.: Noise against threshold for an unirradiated sensor

with the GDAC¹⁰ tune. It varies these two values until the desired threshold is reached. If, for an injection of the target charge, less than 50% of the hits are detected the value will be decreased by a defined step size, and if it is more than 50% it increases.

After the GDAC tuning the dispersion of the threshold is still high. To adjust the threshold in every pixel individually a TDAC tuning can be done. This works in the same way as the adjustment of the global parameter. An overview of the influence on the threshold after each tuning step is given in figure 5.10.

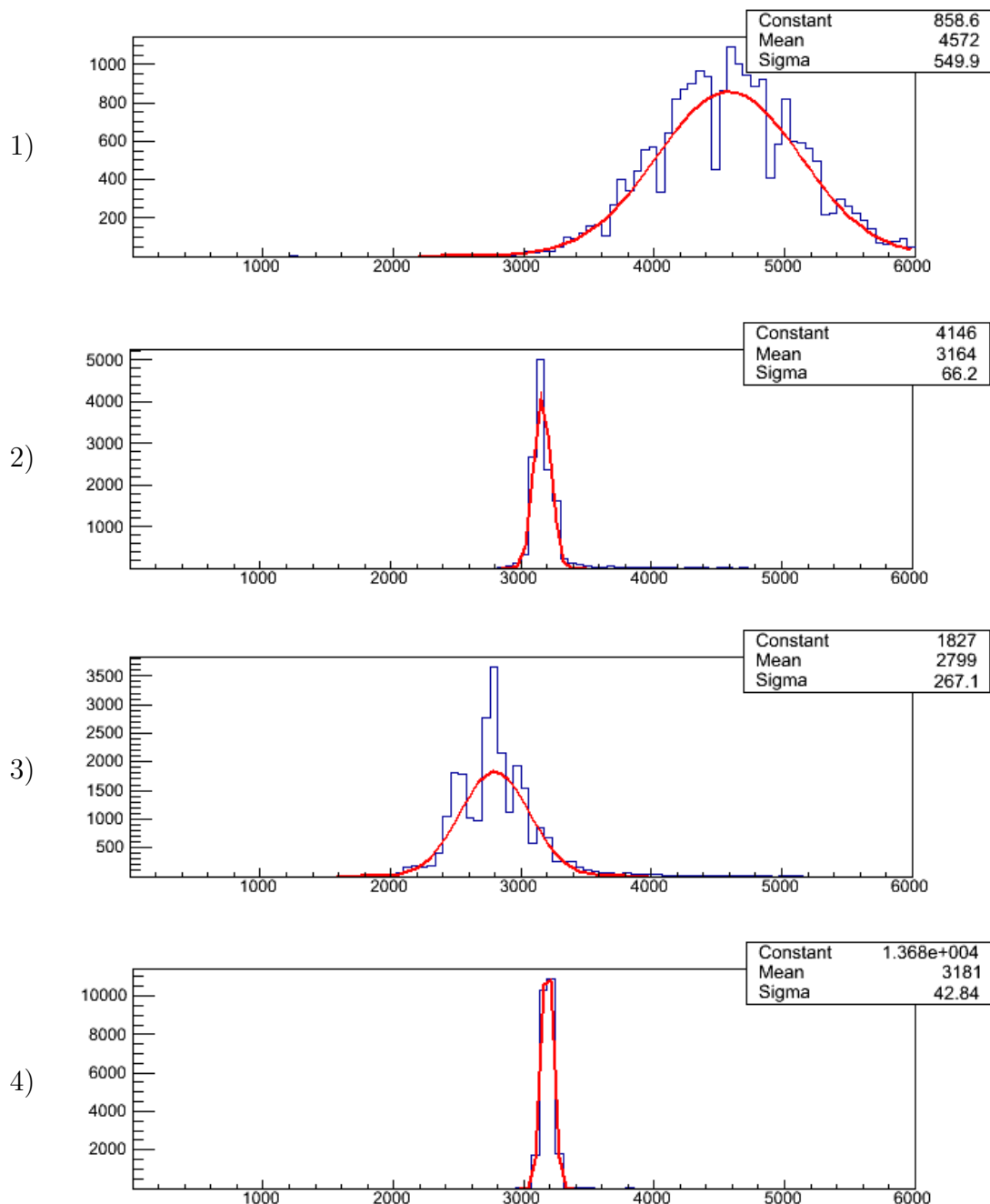


Figure 5.10.: Exemplary threshold tuning of an unirradiated SCA. 1) with standard DAC values, 2) after TDAC tuning, 3) after ToT tuning, 4) after second TDAC tuning

¹⁰Global Digital to Analoge Converter

Time over Threshold Scan and Tuning

To test or tune the ToT a defined charge is injected and the feedback current is scanned to measure the ToT response. The injected charge is changeable so the thickness and the irradiation of the SCA can be taken into account.

As for the threshold it is possible to tune the ToT globally as well as for each pixel. The global tuning can be done with the IF_TUNE. It varies the $PrmpVbpf$ to the best value for the desired ToT. By means of the FDAC_TUNE the FDAC values for each pixel are defined. A reasonable tuning of the ToT is shown in Figure 5.11.

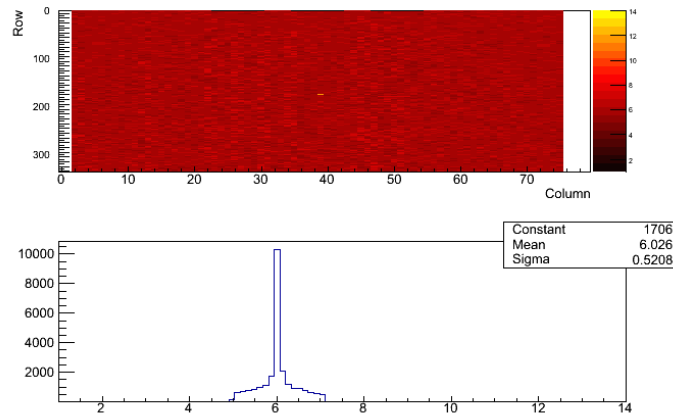


Figure 5.11.: Time over Threshold Scan of an unirradiated SCA after tuning.

Source Scan

To test the assembly with a radioactive source a so called SOURCE_SCAN can be performed. This scan can be done with an external or an internal trigger. The internal trigger signal is generated by the hitbus. It forms a coincidence of the discriminator output of all pixels. Noisy pixels lead to an always high hitbus and have to be masked out. For that it is possible to generate a mask from the scan and load it into the chip configuration (see figure 5.12). The external triggering can be done with a scintillator. The setting in the laboratory is described in section 5.4. The scintillator output can be shaped with an external discriminator, so that only hits above a certain noise level cause a trigger signal. A source scan of an unirradiated SCA is given in figure 5.13 and the corresponding charge collection is shown in figure 5.14 in units of ToT.

Noise Occupancy Scan

Hits are not always recorded due to particles. Noise hits get recorded as well. The noise occupancy scan works in principle like a source scan without a source. It uses a fixed frequency trigger which is not related to the hitbus signal. Figures 5.15 and 5.16 show the result of a noise occupancy scan for a proton and a neutron irradiated SCA. For both scans ten million triggers were set. The activation of the tantalum in the neutron irradiated SCA is obvious.

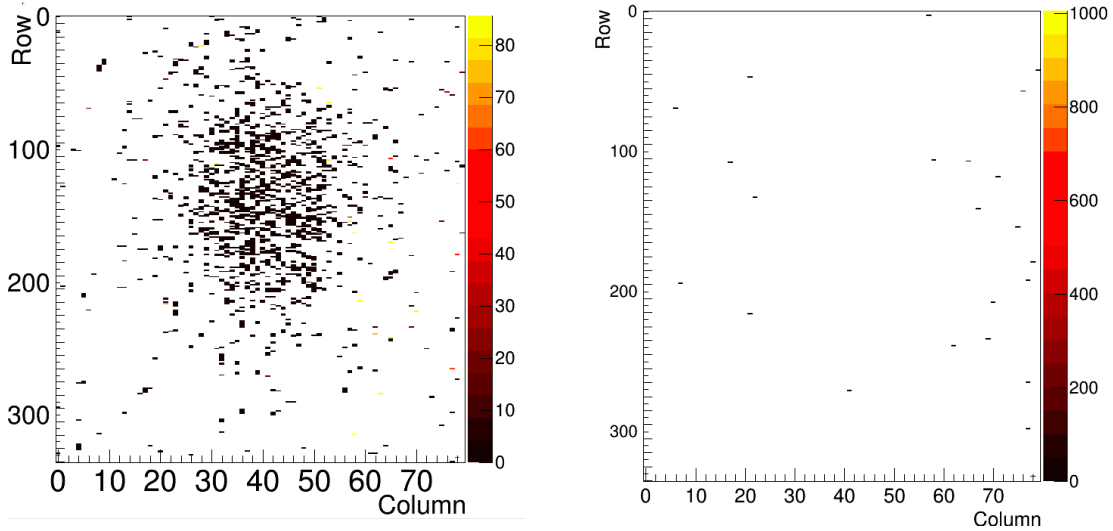


Figure 5.12.: Histogramm of a source scan with a few noisy pixels (left) and the loadable mask histogramm for all pixels with higher entries than five (right).

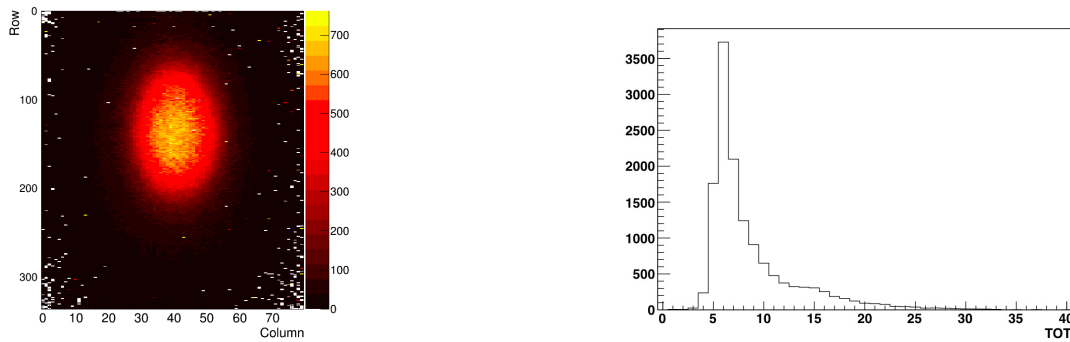


Figure 5.13.: Histogramm of a Source Scan of an unirradiated SCA with a Sr^{90} source.

Figure 5.14.: Charge distribution from the source scan.

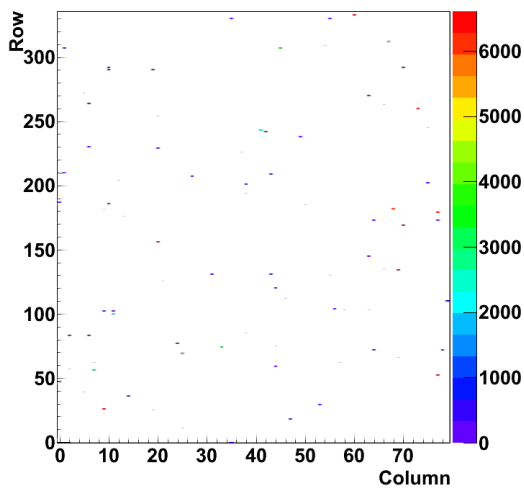


Figure 5.15.: Noise occupancy scan of a proton irradiated SCA.

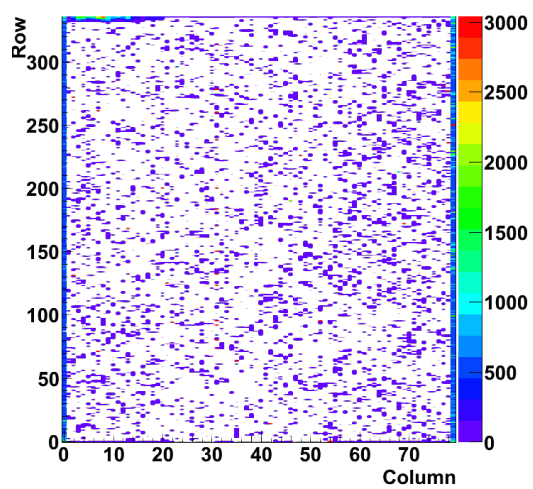


Figure 5.16.: Noise occupancy scan of a neutron irradiated SCA where the tantalum in the FE-I4 got activated.

5.3.3. Single Chip Card

The SCA (see section 4.5) is wirebonded to a PCB¹¹ readout card. This readout card underwent several iterations. On all iterations the SCA is glued to an aluminium carrier which has a good thermal conductivity. This aluminum carrier is constructed as thin as possible to avoid unnecessary multiple scattering during testbeam measurements.

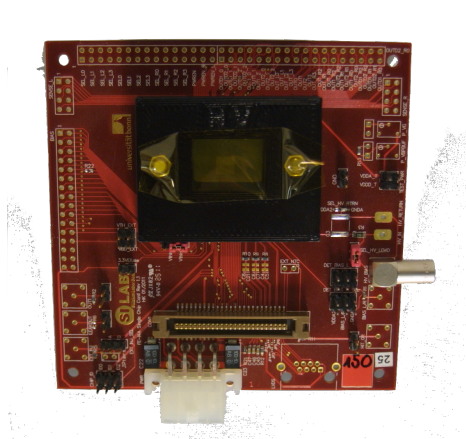


Figure 5.17.: SCC before new cable.



Figure 5.18.: SCC with new soldered cable for bias voltage.

The SCC¹² was never designed to withstand more than 500 V. During a testbeam period a sudden breakdown of the leakage current at -300 V was observed. An IV curve taken at the laboratory in a climate chamber at -25°C air temperature shows a constant breakdown at -600 V. The investigation of the high voltage traces has shown no sparkovers. The lemo connector was unsoldered but underneath there was also no sparkover visible. The workaround applied to a couple of samples is shown in figure 5.18. A lemo cable was soldered directly on the SCC near the sensor and the high voltage trace to the lemo connector was cut. The result of the workaround in comparison to the IV curve before is shown in figure 5.19. The latest iteration of the SCC is shown in figure 5.20. This SCC is constructed to withstand high voltages up to -1000 V. It is also possible to power the SC with modifications to pixel implantations, which is divided into eight different segment [6]. This segments can be supplied with high voltage individually by setting jumpers.

5.4. Laboratory Setup

The core characteristics of the laboratory setup are illustrated in the next sections, the focus is set to the cooling and the mechanical setup for source measurements.. The setup for tuning and readout of the SCAs is described in section 5.3.

¹¹Printed Circuit Board

¹²Single Chip Card

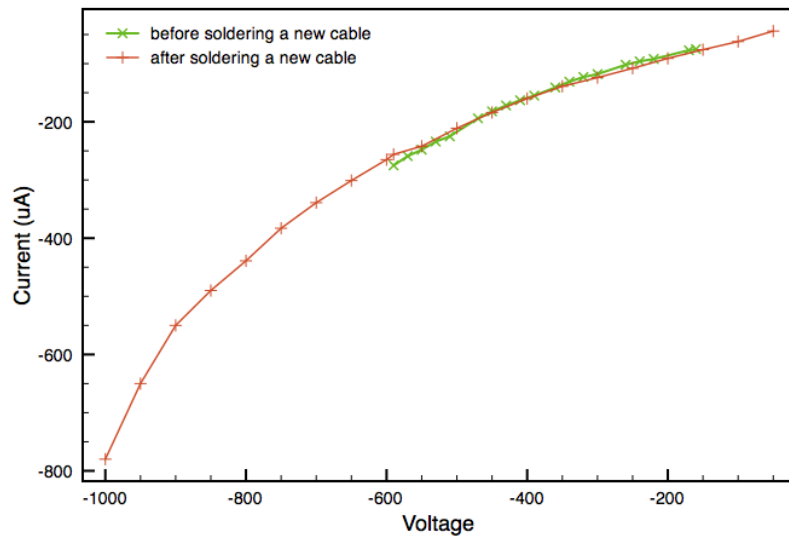


Figure 5.19.: IV curve of an irradiated assembly before and after soldering a new cable. Taken at -25°C air temperature.

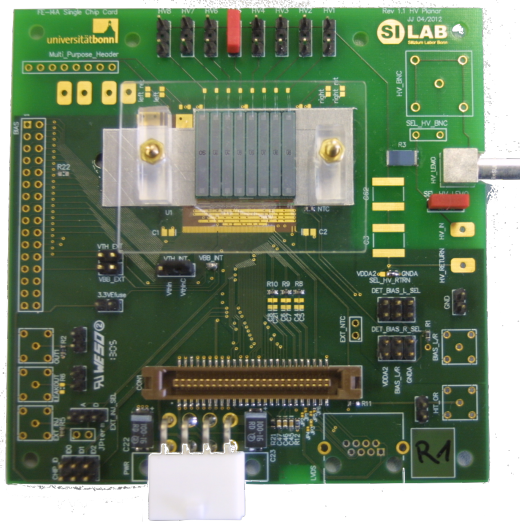


Figure 5.20.: New high voltage single chip card with the possibility to power only segments of the single chip.

5.4.1. Cooling

The cooling of the SCAs is realised with a chiller that is connected to a cooling plate. A sketch of the cooling plate is shown in figure 5.21. The chiller cools down silicone oil and pumps it into the cooling plate thus cooling down the entire setup. To isolate the cooling plate and the SCA from light and humidity the plate is placed inside a styrofoam box.

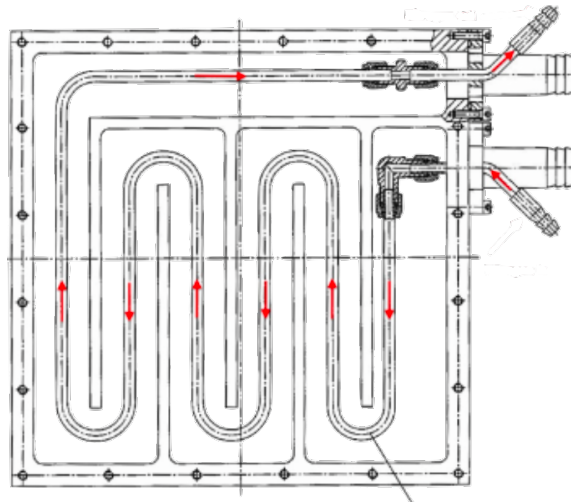


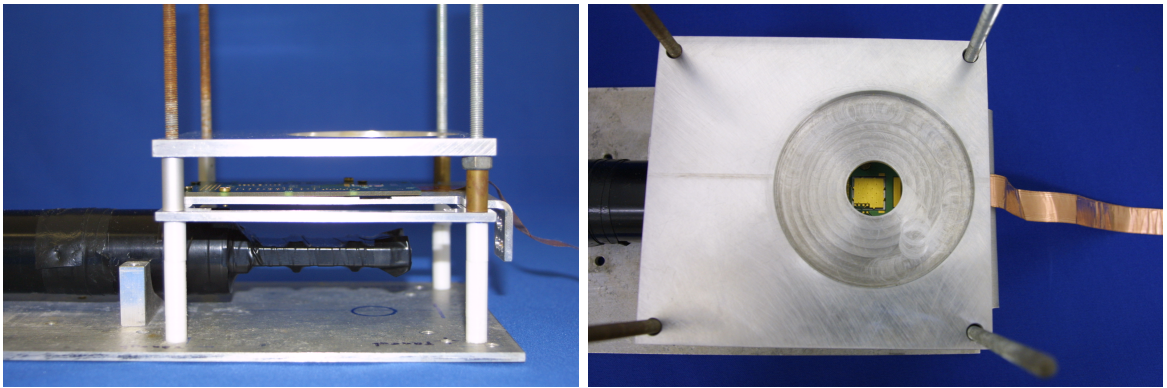
Figure 5.21.: Sketch of the piping for the silicone oil and the dry air.

To avoid surface currents due to humidity the setup can be flushed with nitrogen or dry air. The cooling plate provides a piping system that allows a pre-cooling of the nitrogen or dry air by directing it through the cold plate before flushing into the box.

The temperature is measured with a PT1000 on sensor, on the aluminium carrier and on the backside of the SCC (figure 7.3). The readout is done with a K2000 and the voltage is provided by an ISEG. Every temperature and current measurement is controlled by the testbeamDCS, a program that enables monitoring and readout via computer.

5.4.2. Source carrier

For a good and comparable alignment of the source, SCA and scintillator the source carrier in figure 5.22 was designed. It allows a constant and centric placement of the source above the SCA.



(a) side view

(b) plan view

Figure 5.22.: Pictures of the source carrier.

6. TestBeam

New detectors are required to be tested in an environment similar to that which they will be exposed to within ATLAS to determine how well they function. For this characterisation testbeam measurements are one of the most important techniques to study the sensor performance. To track the charged particles during a testbeam, well characterized detectors are combined to a telescope. The measured tracks can be reconstructed and analysed offline to evaluate the efficiency and the performance of the DUTs¹ for various parameters such as the tilt angle, threshold or bias voltage.

6.1. Beam-Lines

All analysed testbeam data in this thesis were taken at the beamlines at CERN and DESY². An overview of this testbeam facility is given in the following.

CERN SPS H6/8

The Super Proton Synchrotron (SPS) at CERN provides, beside the protons for the LHC, protons for several testbeam lines. All testbeamlines at the north area of CERN can provide different kinds of particles with a certain energy range. This is reached per three main beam targets which are hit by the SPS proton beam. The second beam consists of hadrons and electrons. The particle energy can be varied between 20 GeV and 180 GeV.

The IBL testbeams were operated with high momentum π^+ (~ 120 GeV) which minimizes multiple scattering and allows the simultaneous measurement of four devices in series.

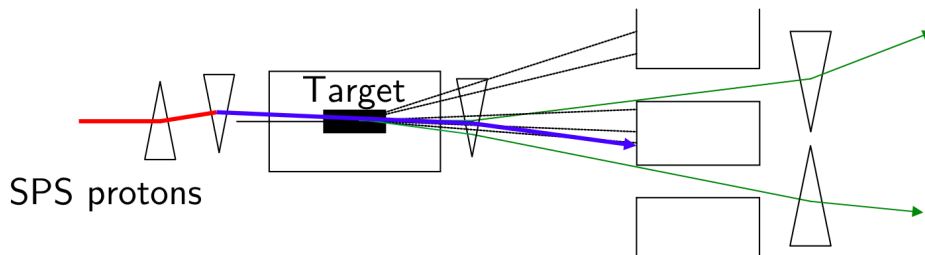


Figure 6.1.: Drawing of the SPS target area. The primary beam passes to dipole magnets to change incident angle into the target, the secondary particles passing a spectrometer magnet are collimated and guided to two beamlines [20].

¹Devices Under Test

²Deutsches Elektronen-SYNchrotron

DESY II

The DESY II can deliver electrons and positrons with an energy of between one and six GeV. Figure 6.2 shows the electron and positron production process at DESY [34]. For the testbeam lines the beam is lead onto a carbon fibre where the photons are created via bremsstrahlung. These photons hit a target and thus create electrons and positrons. The used dipole magnet leads to the variable energy of the particles. Due to the maximum of 6 GeV beam energy, the multiple scattering effect allows a maximum of two DUTs in the beam. The multiple scattering effect limits the tracking precision in measurements. This is important for testbeam measurements where this precision increases with a higher beam momentum.

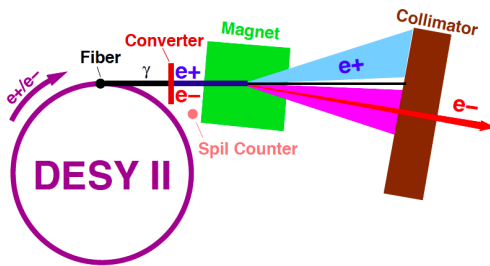


Figure 6.2.: Schematic layout of the electron/positron production at DESY [34]



Figure 6.3.: Picture of the view inside the DESY II tunnel [35]

6.2. Testbeam Setup

A common testbeam setup is shown in figure 6.4. It consists of a two armed telescope with the DUTs in the middle (section 6.2.1). The data are recorded during a window of 16 level-one trigger counts and they are passed to the TLU³ [36]. The TLU is connected to the DUT readout system, to the data streams of the telescope planes and as well to two pairs of scintillators.

The DUTs are readout with the USBPix system (described in section 5.3.1) or with the RCE⁴ system [37]. Multiple USBPix systems can be run simultaneously from a single computer running the data acquisition software EUDAQ⁵ (see section 6.2.3).

6.2.1. Telescope

The trajectories of the beam particles were reconstructed using the high resolution EUDET⁶ telescope (or its successor for ATLAS the so called ACONITE⁷ telescope). The telescope has two arms: one arm is mounted upstream with respect to the DUTs and one arm downstream of the DUTs. Between the two telescope arms is enough and

³Trigger Logic Unit

⁴Reconfigurable Cluster Element

⁵EUdet Data Acquisition system

⁶EUropean DETector R&D towards the International Linear Collider

⁷All copies of the EUDET are renamed after poisonous flowers: aconite, anemone, caladium and datura.

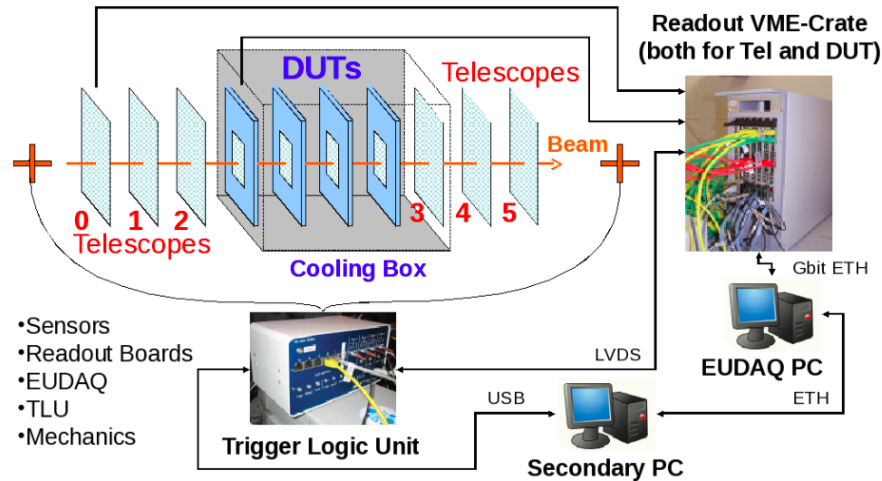


Figure 6.4.: Sketch of a standard testbeam setup [10].

variable space for the box containing the DUTs. One telescope arm consists of three sensor planes. As sensitive elements each sensor plane has a Mimosa⁸-26 active sensors with an active area of $21.2 \times 10.6 \text{ mm}^2$ and square pixel cells of $18.4 \mu\text{m}$ pitch [38]. These sensors fulfil the requirements of a testbeam telescope to provide a single-point spatial resolution in the order of $2 \mu\text{m}$, while the amount of material has to be as low as possible. The Mimosa26 sensors employ a rolling shutter system with an accumulated integration time of $112 \mu\text{s}$. The DUTs are read out every 400 ns . This means that there are a lot of tracks registered by the telescope that cannot be registered by the DUTs, as they are not in the right time window.

Since most of the performed measurements are time sensitive and the integration time of the telescope planes is quite long, one of the DUTs is used as a reference plane. This reference plane has to be unirradiated, well understood, a minimal number of dead pixels and a minimal number of noisy pixels.

6.2.2. Cooling and Mechanics

Due to the increase of the leakage current by irradiation the DUTs should be operated in the dark and at low temperatures. For that reason a polystyrene box, the DOBox⁹, was designed and build to reduce the influence of light and external temperature changes. The DOBox mounted between the telescope arms is shown in figure 6.6. The cooling is realized with dry ice. There is a compartment for the storage of the dry ice in the DOBox. A computer aided drawing of this compartment is shown in figure 6.7 and a picture of it after removing the dry ice can be seen in figure 6.8. A thermal connection of the DUTs is given through copper tape. This tape is mounted on the back side of the sample and guided under the dry ice. This can also be seen in figure 6.7 and in the photography 6.10. The temperature of the sensor is monitored via a PT1000 or, in later testbeams, a NTC¹⁰. The PT1000 is glued with superglue on the surface of the sensor. The placement can be seen in figure 6.9. The DUTs are mounted onto a L-shape

⁸Minimum ionising particle metal oxide sensor active pixel sensor

⁹DOrtmund testbeam BBox

¹⁰Negative Temperature Coefficient thermistors

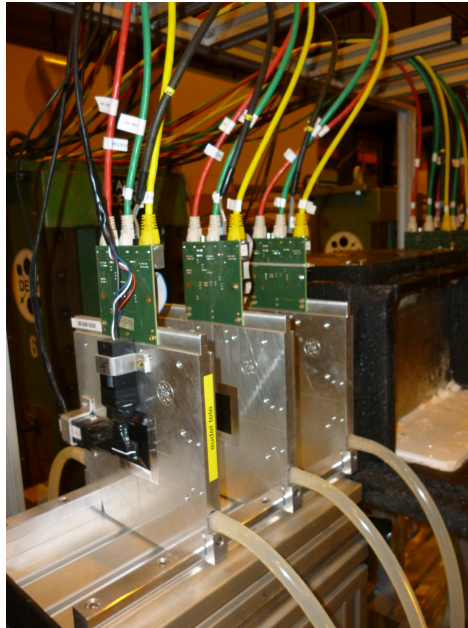


Figure 6.5.: Picture of three EUDET telescope planes

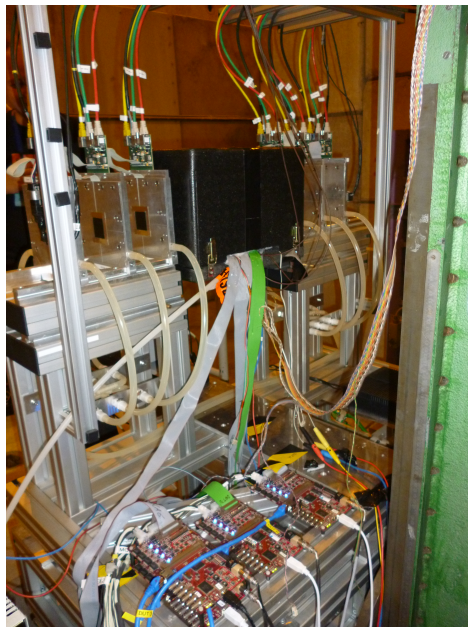


Figure 6.6.: Picture of the telescope with the DOBox mounted between the two telescope arms and connected USBPix systems.

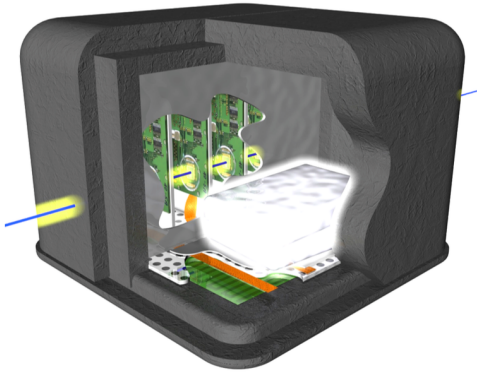


Figure 6.7.: Computer aided design of the DOBox with an open view of the dry ice department. [20]

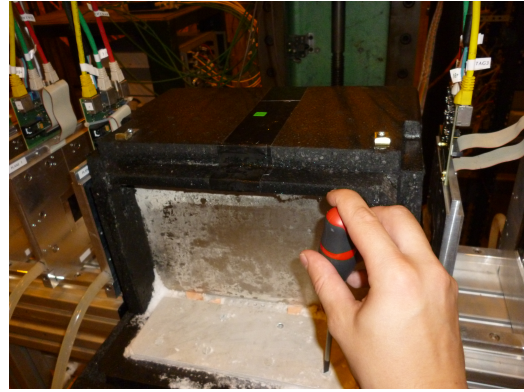


Figure 6.8.: Picture of the DOBox with open dry ice department directly after removing the dry ice.

mount (figures 6.9 and 6.10). This mounts can be screwed to the aluminium baseplate of the DOBox. For good alignment and flexibility of the measurements rotation plates, wedges and heightenings were designed (see picture 6.12).

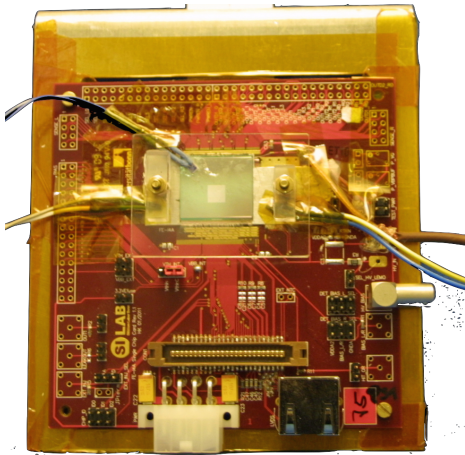


Figure 6.9.: SCA front with PT1000

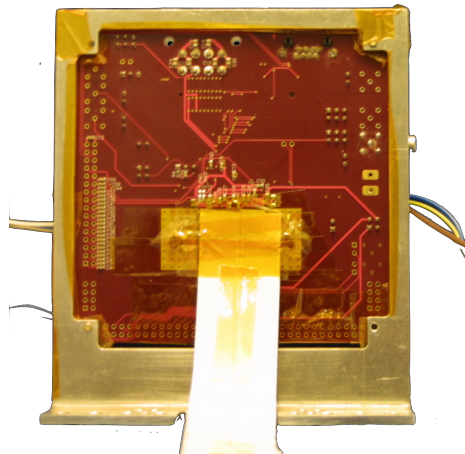


Figure 6.10.: SCA back copper tape

6.2.3. The Telescope-DAQ-Software

The EUDAQ software uses producers to communicate between the various hardware components. These producers are independent and connected to each other via Ethernet connection. One of the central producers is the *Run Control*. This is a graphical interface, shown in figure 6.13, that allows the user to control the data taking. It is possible to load different data taking configurations and to start and stop runs. The other central producer is the *Data Collector*. It gets data streams from different producers and write this information in a raw data file. This file contains all information from each telescope plane and DUT. For each run a new file is written. The size of this run raw files is adjustable.

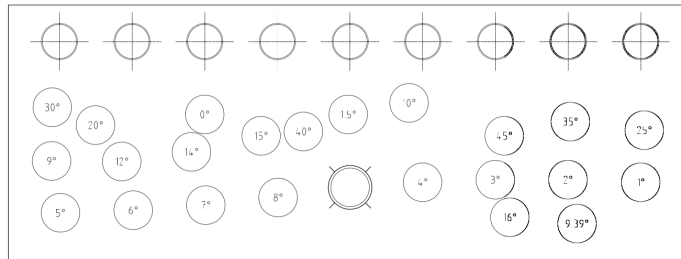


Figure 6.11.: Rotation plate

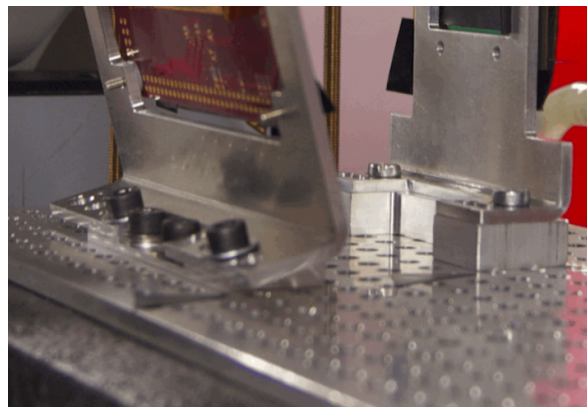


Figure 6.12.: Wedges

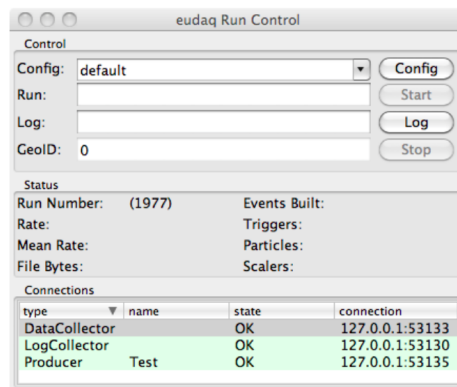


Figure 6.13.: Eudaq run control panel. [39]

Online data monitoring

To be able to control the collected data during the data taking the EUDAQ software provides a live event display called *Online Monitor*. The online monitor reads in the raw file that is written during data taking or can display informations about runs that are already on the hard disk. An example of the online monitor plots is given in figure 6.20, it shows all plots for DUT0 for one run.

The alignment of the DUTs to each other is done via the L-shape mounts in the DOBox. For the alignment of the DUTs and the telescope planes the DOBox is mounted to a x-y-table. Via a remote connection it is possible to move the table with the box on top. To check the alignment, the online monitor provides, beside the information for each DUT, correlation plots. These plots are two-dimensional and an example is given in figure 6.14. Ideally for two well aligned sensors the hits on the correlation plots starts at the bottom left at zero and extend in a 45° angle to the top right. Each incident particle should hit the sensor planes at the same x-y-coordinate.

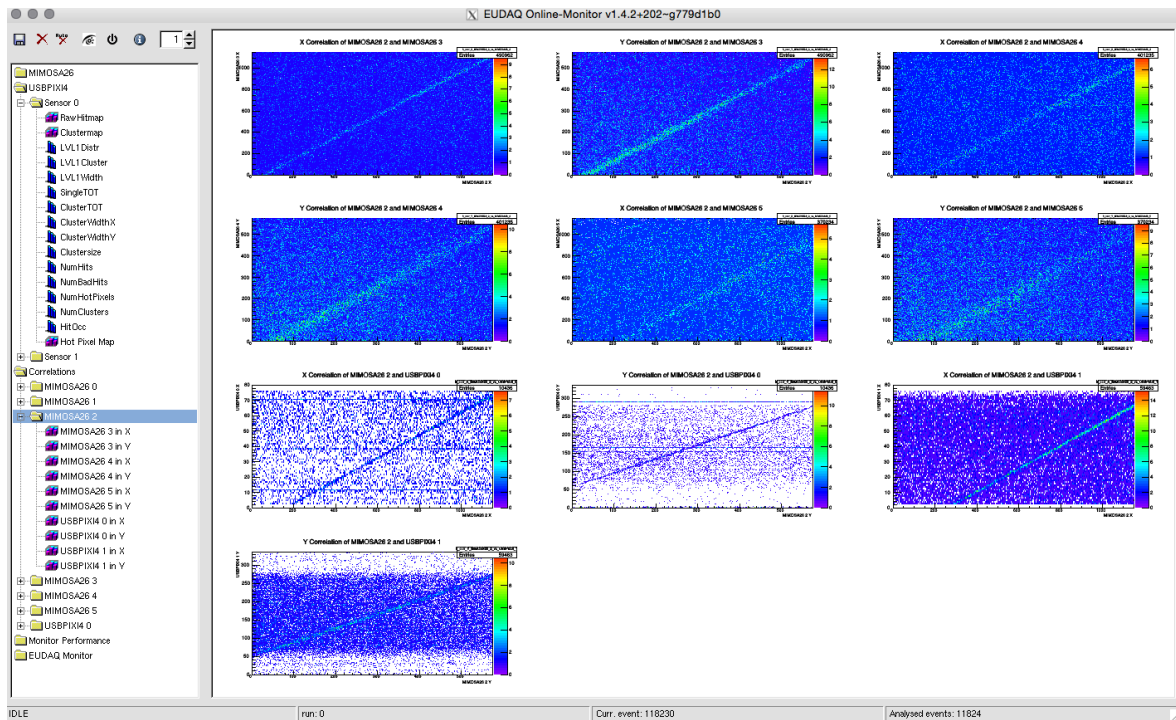


Figure 6.14.: Screenshot of the Online Monitor correlation plots for the MIMOSA plane 2 with all other MIMOSA planes and the DUTs for run 50880 at the IBL testbeam in march 2012.

6. TestBeam

The important plots from the online monitor to check if the data that are collected are good during data taking are:

- **ToT Clusters:** The ToT Clusters shows the charge deposit of the incident particles. The charge information is given in ToT and for that reason the peak position depends on the tuning of the DUT. An example plot is given in figure 6.15 of an unirradiated SCA with a tuning of 3200e and 6 ToT for 20000e at a bias voltage of -500V.

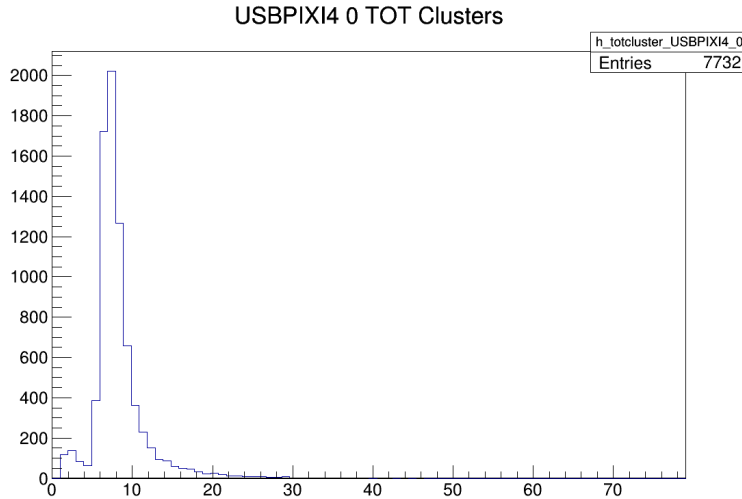


Figure 6.15.: Screenshot of the Online Monitor ToT Cluster of DUT0 during the PPS testbeam in March 2013. Run 1541 with a DUT tuning of 3200e with 6 ToT at 20000e, at a bias voltage of -500 V.

- **Hot Pixel Map:** The Hot Pixel Map is a 2D map and points the position of hot, respectively noisy, pixels. The position is given in column and row coordinates. With this coordinates it is possible to mask the hot pixels in the SCA configuration. Figures 6.16 and 6.17 give an example of the Hot Pixel Map with and without pixel identified as hot.

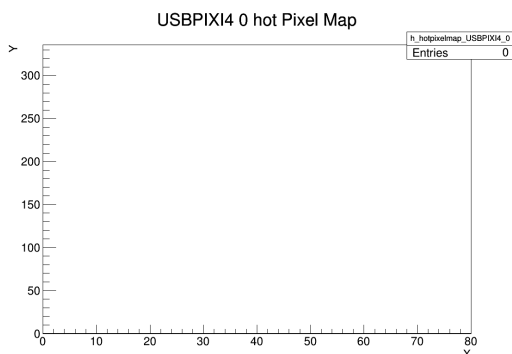


Figure 6.16.: Screenshot of the Online Monitor Hot Pixel map. For this tuning with a threshold of 3200e no pixel is identified as hot. (PPS TB 2013, DUT0, run 1541)

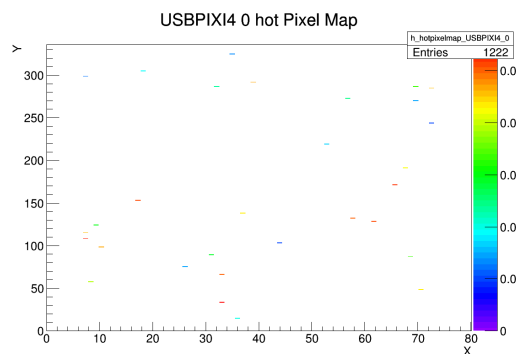


Figure 6.17.: Screenshot of the Online Monitor Hot Pixel map. For this tuning with a threshold of 1100e a few pixels (<1%) are identified as hot. (PPS TB 2013, DUT0, run 1725)

- **LVL1 Pixel Distribution:** The LVL1 Pixel Distribution shows the LVL1 timestamp of the single pixels. The value for each single hit is displayed. Figure 6.18 shows an example LVL1 distribution of run 50880 from the IBL testbeam in march 2012. Pointed is DUT0, which is an irradiated SCA with protons up to a fluence of $5 \cdot 10^{15} n_{eq}/cm^2$ with a bias voltage of -500 V and a threshold of 2000 e.

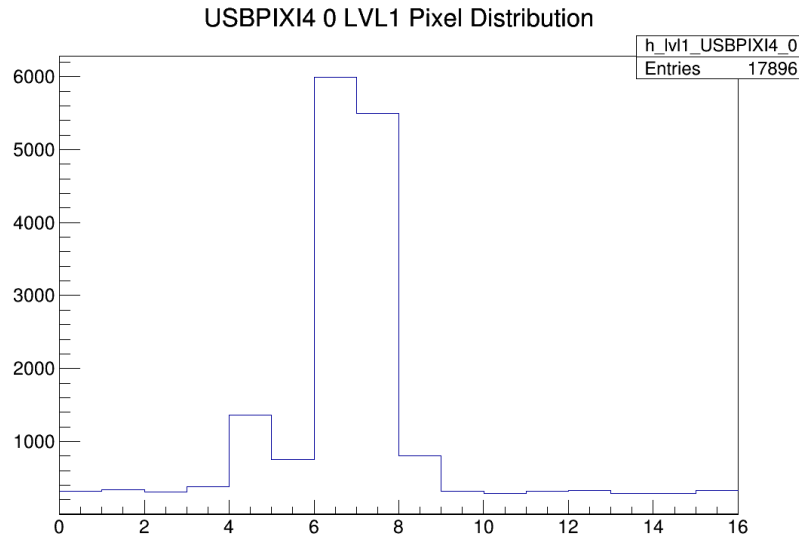


Figure 6.18.: Screenshot of the LVL1 pixel distribution for DUT0 which is proton irradiated with a fluence of $5 \cdot 10^{15} n_{eq}/cm^2$ during the IBL testbeam in march 2012.

- **Raw Hitmap:** The Raw Hitmap shows all hits the DUT registered during the data taking, without any clustering algorithm or cuts.

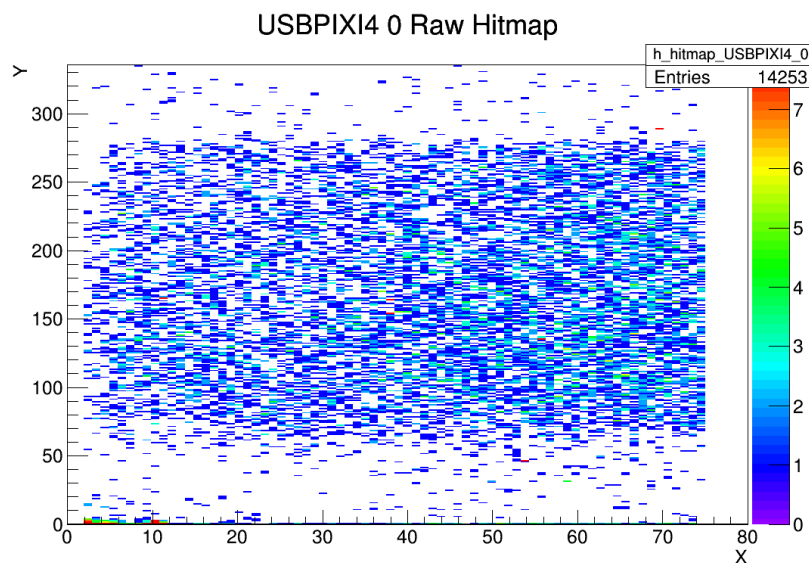


Figure 6.19.: Hitmap

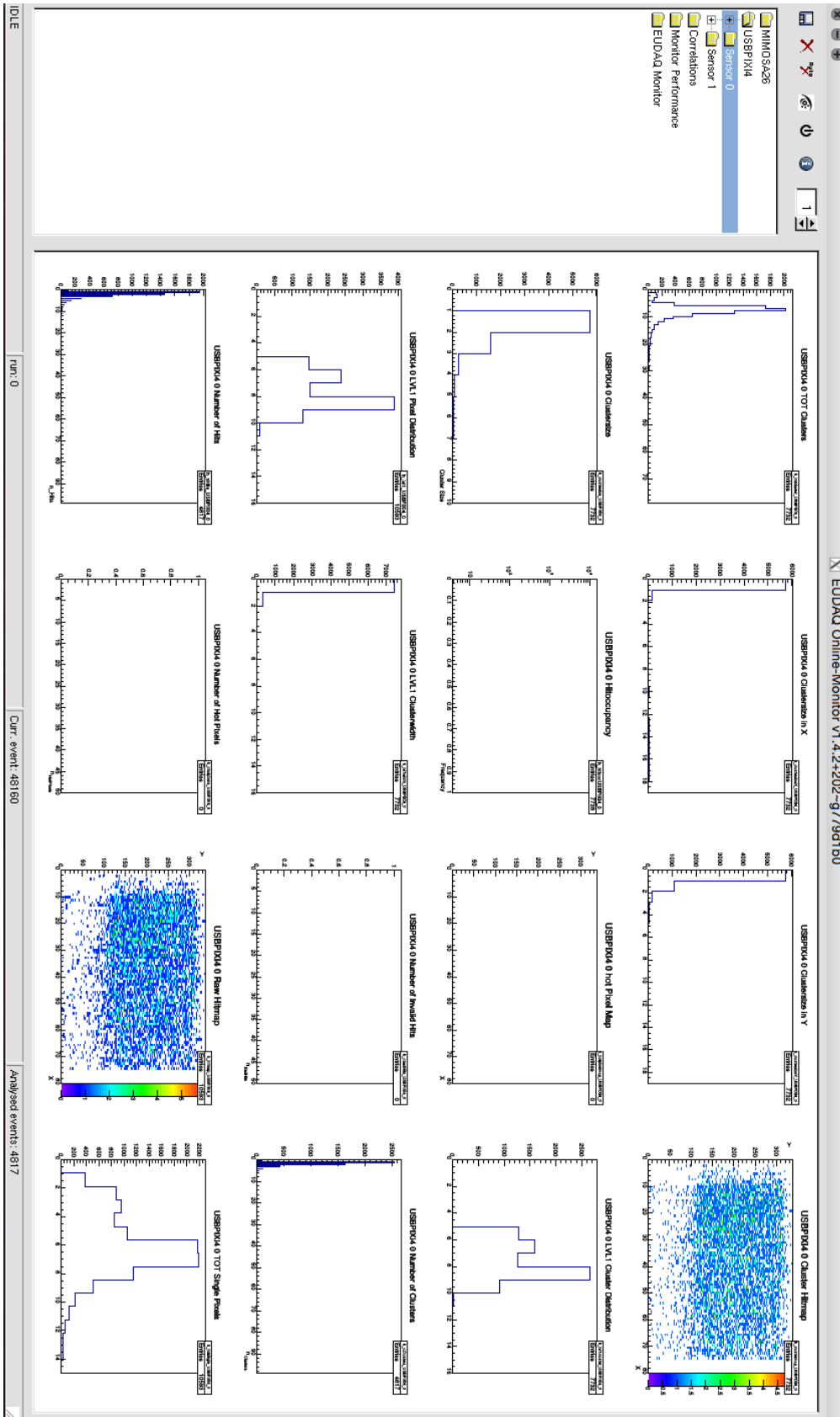


Figure 6.20.: Screenshot of all informations the Online Monitor provides for DUT0 during the PPS testbeam in March 2013, only filled with run 1541.

6.3. Analysis Chain

Before the data of a testbeam can be analysed they have to be reconstructed. This is performed with the EUTelescope software which is implemented as a processor within the MARLIN¹¹ framework. This package and afterwards the analysis tool TBmon will be described in the next section.

6.3.1. Reconstruction with EUTelescope

All informations that are necessary for reconstruction, like pixel pitch, rotation, angles and absolute positions, were described in a GEAR¹² file. This informations are important during the reconstruction procedure. The reconstruction steps are shown in figure 6.21 and are described in short detail below.

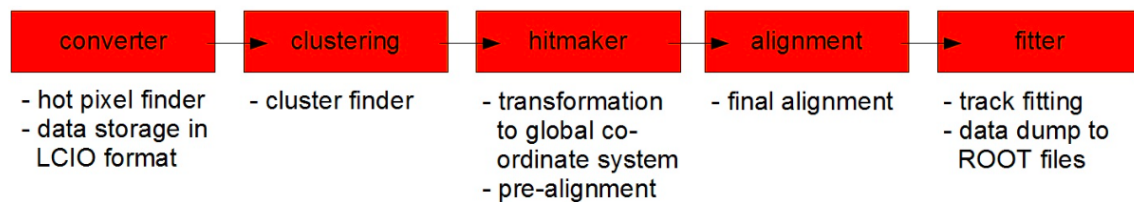


Figure 6.21.: The track reconstruction chain for the testbeam data. [40]

Data converter

At the first reconstruction step the raw data files are converted to the LCIO¹³ data format. The hit informations of the telescope planes and the DUTs are written in separate data collections. During this step also a search for noisy pixel is operated. This is important to avoid fake tracks in the alignment.

Clustering

After the data converter step with its search for hot pixels an event based search for clusters is executed. A cluster consists of a number of hits in different pixels of target plane caused by the same incident particle. For non rotated sensors a single particle deposits its charge in one to two pixel cells. The clustering is done separately for the the telescope planes and the DUTs.

Hitmaker

The third reconstruction step is the “*hitmaker*”. Here the local hit coordinates of the sensor, in terms of rows and columns, are transformed to a global coordinate system

¹¹Modular Analysis and Reconstruction for the LINear Collider

¹²GEometri Api for Reconstruction

¹³Linear Collider In / Oout

6. TestBeam

of the telescope. During the *hitmaker* step, a pre-alignment is also done. These rough pre-alignment values provide a better starting point for the fine-alignment in the next reconstruction step.

Alignment

This step utilises the software MillepedeII [41] to determine the alignment constants. The used fitting algorithm requires that the actual path of the particle through the setup is not a straight line, but kinked, due to multiple scattering. There are also these assumptions that are taken into account: the thickness of the material is much less than the space between the planes, the telescope planes are parallel, the angular spread of the particle beam is small and there is a negligible beam energy loss as the beam crosses each telescope plane [42].

Track fitter

The *Track fitter* is the final step of the reconstruction and reconstruct the particle track through the setup. All results of the previous steps were taken into account. The final output is stored in a .root file and can be analysed with TBmon. The structure of this file is shown in table 6.1.

6.3.2. TBmon

The next step after the reconstruction of the testbeam runs is the analysis with the offline analysis tool called TBmon. It is written in C++ and includes ROOT¹⁴ classes. TBmon reads in the .root file produced after the last stage of the reconstruction and allows the user to combine several runs for one analysis that were taken under the same conditions, e.g. the same bias voltage, threshold and temperature.

The standard pre-analysis steps are:

- Hotpixel finder
- Check alignment with applied pixel masks
- Eta correction with applied pixel masks and alignment corrections
- Check alignment with applied pixel masks and the result of the eta correction

After this standard pre-analysis the central analysis part of TBmon can be executed like the efficiency analysis.

Hotpixel finder

The *Hotpixel finder* creates an out-of-time hitmap per DUT by analysing the LVL1 timing distributions of the data. The available cut for this is set per default to $5 \cdot 10^{-4}$. Here two kinds of pixel are identified dead pixel and noisy pixel. The dead pixel are showing no hits in all of the runs and got marked as dead pixeln and written in a text

¹⁴root.cern.ch

Table 6.1.: Content of the final output file of the reconstruction.

TTree	content	TTree	content
euhits		zspix	
nHits	No of hits in this event	nPixHits	No of raw hits in this event
xPos	Global x coordinate (mm)	euEvt	Current event no
yPos	Global y coordinate (mm)	col	column of raw data hit
zPos	Global z coordinate (mm)	row	row of the raw data hit
clusterId	ID of the corresponding cluster	tot	TOT of the raw data hit
sensorID	ID of the corresponding sensor	lv1	LVL1 value of the raw data hit
		iden	ID of the device
		chip	ID of the device in the MCC board
		clusterId	ID of corresponding cluster
etracks		euclusters	
nTrackParams	No of parameters for estimation	euEvt	Event no
euEvt	Event no	size	No of pixels in a cluster
xPos	The fitted y position (mm)	sizeX	Cluster width in x (pixel)
yPos	The fitted y position (mm)	sizeY	Cluster width in y (pixel)
dxdz	The fitted derivate ?x/?z	posX	Position of the cluster in x (pixel)
dydz	The fitted derivate ?y/?z	posY	Position of the cluster in y (pixel)
trackNum	The track ID	charge	Sum charge of the cluster (ToT)
iden	ID of the corresponding device	iden	ID of the corresponding device
chi2	? of the track	ID	ID of the cluster
ndof	tracks degrees		
timing			
NTimings	No of timings in this event		
SensorId	ID of the corresponding device		
TluId	TLU ID of this event		
TpllId	TPLL ID of this event		
RealtimeSec	Realtime since clock reset (s)		
RealtimeNs	Realtime since clock reset (ns)		
RunNumber	No of the run		

6. TestBeam

file. The pixel that exceed the occupancy cut are marked as noisy pixel in this step and were written in the same text file as the dead pixel. There is the possibility to get a text file after each analysis step with the main informations, an example is shown in figure 6.22. The corresponding hitmap and occupancy mask for DUT0 can be seen in figure 6.23.

```
[ hotpixelfinder-20 ]:  
[ hotpixelfinder-20 ]: Number of pixels identified as hot: 0(0%)  
[ hotpixelfinder-20 ]: Number of pixels identified as dead: 4579(17.035%)  
[ hotpixelfinder-21 ]:  
[ hotpixelfinder-21 ]: Number of pixels identified as hot: 254(0.94494%)  
[ hotpixelfinder-21 ]: Number of pixels identified as dead: 4628(17.2173%)  
Done looping over 451088 triggers.
```

Figure 6.22.: Screen shot from the log file after running the Hotpixel finder for run 1521-1535 from the PPS testbeam in March 2013.

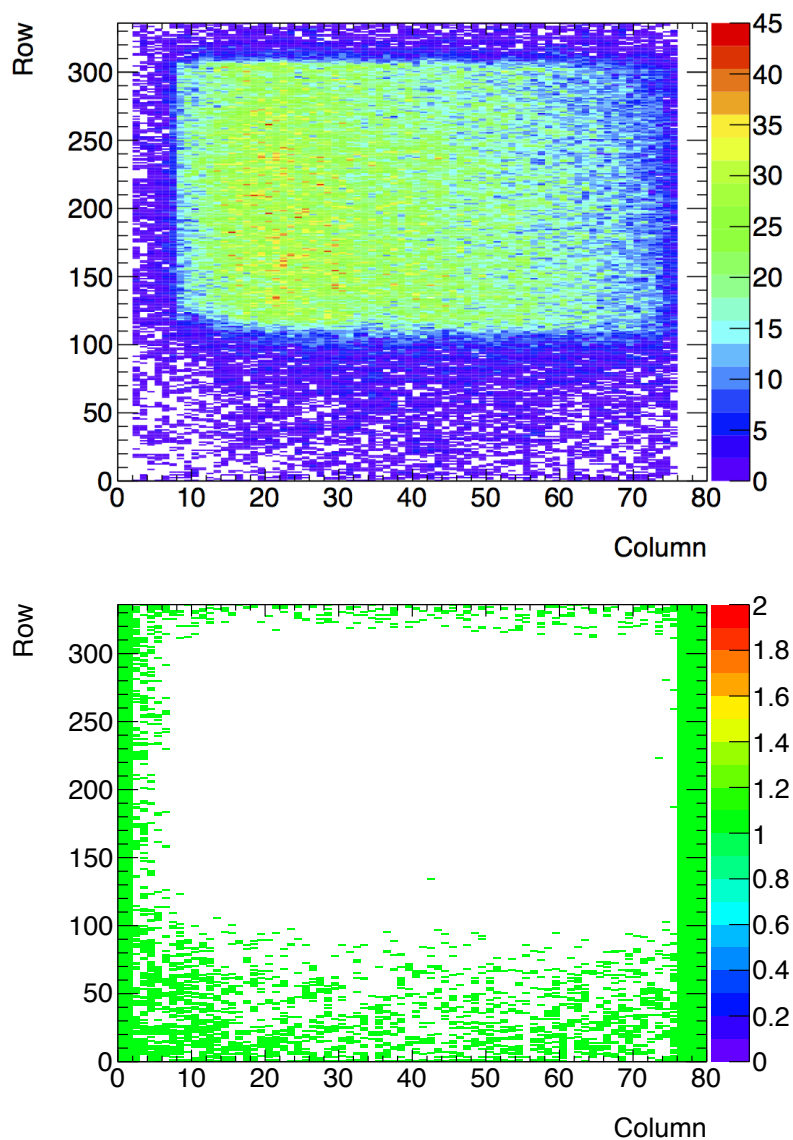


Figure 6.23.: Hitmap (top) and occupancy mask (bottom) for run 1521-1535 for DUT0 from the PPS testbeam in March 2013.

Check align

Check align is the alignment processor for the DUTs included in TBmon. The cuts and masks that are applied in this analysis process are:

- χ^2 cut with a default value of 999
- matching radius with a default of 1.5 x pixel pitch
- number of other planes required to have a matched hit with a default set to 1
- LVL1 timing cut, 0-10 in units of 25 ns per default
- restriction to the central region of the sensor
- track is not extrapolated to a masked pixel/cluster
- event contains at most one cluster per plane
- in the second check align step the eta correction (see next step)

To get an impression of the alignment quality different histograms are available showing the residual against hit position for all combinations. The track residual is the distance between the expected track position on the device and the charge weighted cluster center position. An example of two possible histograms is given in 6.24. For a perfect alignment the histograms show a horizontal line at a value of zero. If the horizontal line has a slope the reconstruction has to be run again with applied angle corrections.

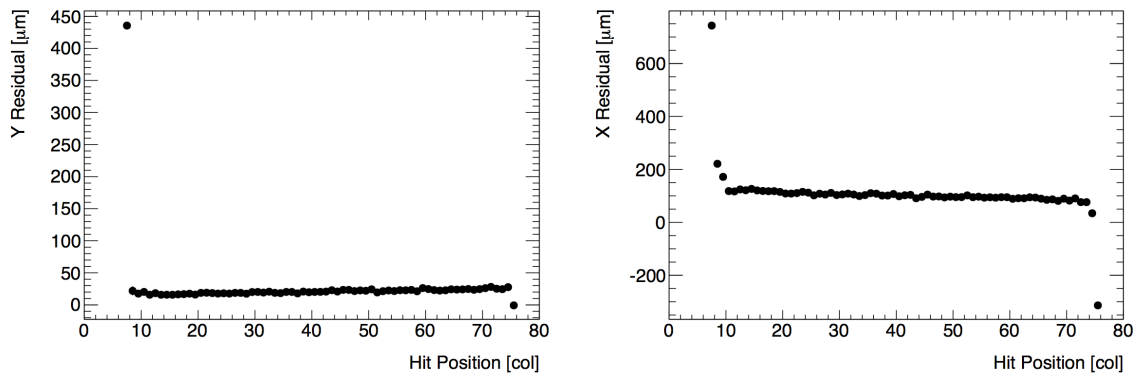


Figure 6.24.: Example histograms from the Check align step in TBmon. The data points far off the horizontal lines are at the edge of the scintillator region and have low statistics.

Eta correction

The eta correction is applied to the cluster to achieve the highest possible alignment quality. This correction is calculated for each DUT individually.

After this basic steps the central analysis part of TBmon can be executed. In this thesis the focus is set to the tracking efficiency.

Hit Efficiency

The determination of the efficiency is caused by the definition of the efficiency itself and as well by the setup during the measurement. The definition of the efficiency is given by:

$$\text{Eff} = \frac{\text{no of tracks with matched hits}}{\text{total no of in-time tracks}} \quad (6.1)$$

and the binomial error of the efficiency with:

$$\sigma(\text{error}) = \sqrt{\frac{\text{Eff} \cdot (1 - \text{Eff})}{\text{no of tracks}}} \quad (6.2)$$

Due to different parameters, they are discussed in section 7.2.2, the error underestimates the real error. For the efficiency calculation only tracks are taken into account, which go through the center region of the device and pass the χ^2 cut. The effect of the matched hit criterion is shown in figure 6.25 by comparing the raw hitmap with a matched in-time hitmap.

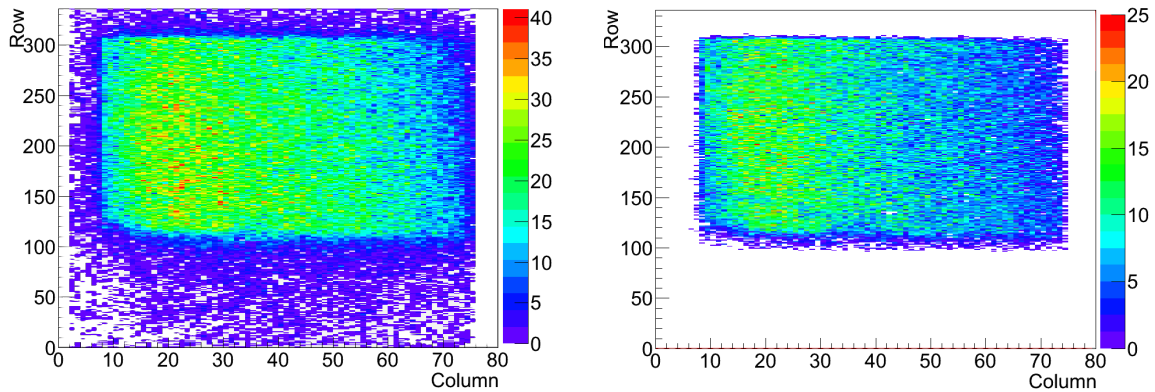


Figure 6.25.: Hitmaps from DUT0 (PPS TB March 2013, run 1521 - 1535).

Left: Hitmap without any cuts, just counting the number of hits per pixel.

Right: Hitmap after applying timing cuts and only hits are taken into account that can be matched to a track.

An example efficiency histogram is given in figure 6.26. The edge regions are excluded for every efficiency map. The efficiency analysis provides beside the histogram a log file with the overall efficiency (figure 6.27).

6.3.3. Uncertainty of the testbeam measurements

A lot of different elements interact with each other during testbeam measurements. This section will give an idea of the uncertainties that are relevant for the grading of the testbeam results.

- *Bias Voltage:* For the applied bias voltage the error is estimated to be ± 1 V. This results on the lowest precision of the used high voltage supply. It was not possible to use at every testbeam campaign the same high voltage supplies and due to a

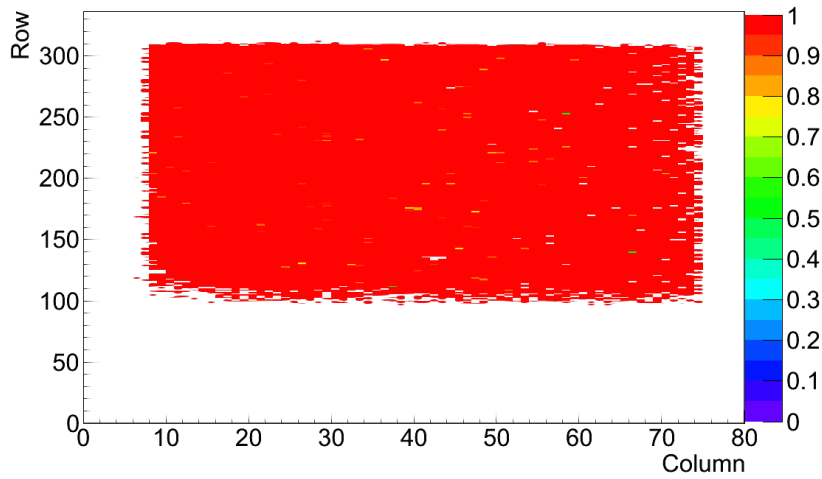


Figure 6.26.: Histogram of the efficiency for DUT0 during the PPS TB in March 2013 run 1521 - 1535.

```
[ efficiency-20 ]: Tracks:      104999
[ efficiency-20 ]: Hits:       104996
[ efficiency-20 ]: Tracks w/ hit: 104901
[ efficiency-20 ]: Efficiency (match): 0.999067 +- 9.42378e-05
[ efficiency-20 ]: Efficiency (any): 0.999971 +- 1.64956e-05

[ efficiency-21 ]: Tracks:      94142
[ efficiency-21 ]: Hits:       94023
[ efficiency-21 ]: Tracks w/ hit: 93839
[ efficiency-21 ]: Efficiency (match): 0.996781 +- 0.000184603
[ efficiency-21 ]: Efficiency (any): 0.998736 +- 0.000115802
```

Figure 6.27.: Efficiency detail of the log file for DUT0 and DUT1 for run 1521 - 1535 during the PPS TB in March 2013.

6. TestBeam

lack of documentation it is not possible to correlate the right high voltage supply channel to the investigated devices.

- *Temperature:* The temperature has a huge effect on the leakage current and the noise of an assembly, which again influences the hit efficiency of the devices. The sublimation of the dry ice has beside the influence on the temperature an influence on the alignment of the DOBox. The shift of the hole box in x and y direction is shown in figure 6.28 for an IBL testbeam run.

The temperature measurement was done with PT1000s and NTCs at different

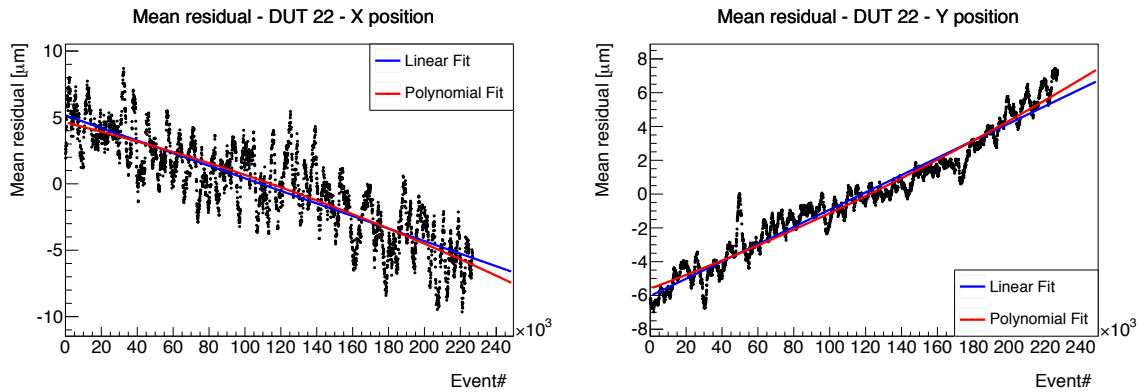


Figure 6.28.: Average Residual plot against time for DUT22 in run 61510 during the IBL TB in September 2011. [43]

places on the DUT and/or the readout card. Due to an only two wire readout and an impossible correlation of the measured temperature and the placement of the PT1000 or NTC the uncertainty of the temperature is estimated to $+2^{\circ}\text{C}$.

- *Fluence:* As described in section 5.2 the actually delivered fluence is determined by measuring the activation of aluminium foil. The radiation background for the JSI reactor is well known due to simulations and regular measurements. An uncertainty for the fluence of 10% is reliable.
- *Annealing:* The annealing of irradiated sensors is relevant for the leakage current and the charge collection. To avoid annealing all DUTs were kept cold before, during and after measurements in the lab and testbeam. But for mounting and dismounting in an experimental setup it was necessary to thaw the DUTs to avoid glazed frost due to condensation. The annealing received through that can be neglected because it can be summed to less than 24 h at room temperature.
- *Reference DUT:* The reference DUT is an unirradiated device which passed the quality criteria of lab measurements and is necessary for in-time measurements. The conditions, threshold and bias voltage, during the measurements were kept constant. Unfortunately it was necessary during some testbeams to change the reference DUT due to high leakage currents or noisy pixel and the new reference DUT did not fulfil the quality criteria completely. An example for a reference DUT with a problem is given in figure 6.29. The efficiency map of PS2 has a missing region which is caused by the unirradiated reference device FBK13. FBK13 had bump-bonding issues in this region and no tracks could be matched there.
- *Hit Efficiency:* Due to the various number of influences on the efficiency and the lack of some informations about conditions during the testbeam runs the

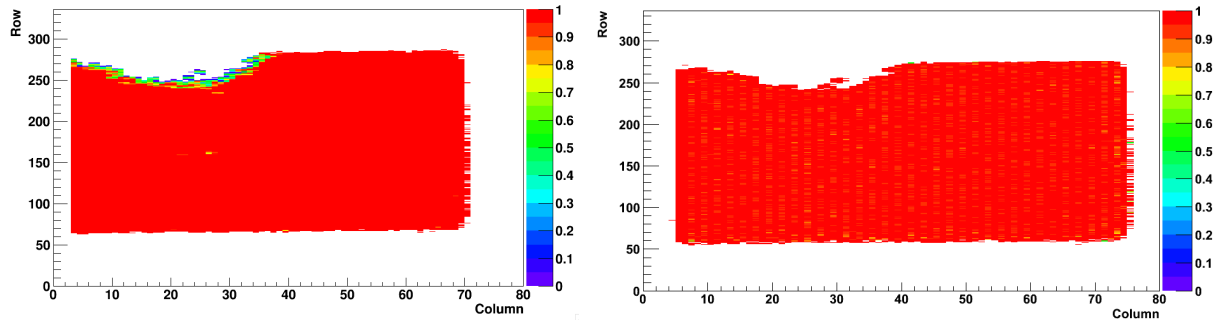


Figure 6.29.: Efficiency maps of FBK13 (left) and PS2 (right) from the IBL TB in March 2012.

systematic error on the hit efficiency values can not be calculated. The statistical error is insignificant due to a high statistic for each measured step. A rough and established estimate is an error for the hit efficiency of -1 %.

7. Results of Lab and TestBeam Measurements

This section presents the results of the laboratory and testbeam measurements of the IBL assemblies (section 7.2) and the comparison and measurements of MCz and FZ assemblies (section 7.3).

7.1. Devices under test

All devices investigated in this thesis are listed in table 7.1 with their characteristics. Every device is a FE-I4 Single Chip sensor flip-chipped to a FE-I4A Front End.

Table 7.1.: FE-I4 devices under test

Sensorname	Design	Irradiation	Fluence ($10^{15} \text{ n}_{eq} \text{ cm}^{-2}$)	Thickness (μm)
SCC 31	slim edge	unirrad.	-	250
PS1	slim edge	proton at CERN	5	200
PS2	slim edge	proton at CERN	5	200
SCC51	slim edge	proton at KIT	4	250
SCC60	slim edge	proton at KIT	6.8	200
SCC61	slim edge	proton at KIT	6.8	200
LUB2	slim edge	neutron at Ljubljana	4	250
LUB4	slim edge	neutron at Ljubljana	5	200
MCz1	slim edge	unirrad.	-	285
MCzPi	slim edge	pions at PSI	0.5	285
FZPi	slim edge	pions at PSI	0.5	200

7.2. IBL sensors

In the framework of this thesis a significant contribution to the data taking of the IBL testbeam campaigns has been done. This includes the preparation of the samples, the construction, debugging and expertised operation of the telescope and DUT data acquisition systems.

7. Results of Lab and TestBeam Measurements

The sensors for the IBL project have to fulfil defined conditions, which are specified in section 2.4.1. To investigate whether the considered sensor technologies are able to fulfil this conditions IBL testbeam campaigns were performed. In these campaigns at CERN and DESY different institutes were involved to test their sensors.

The next section will show the results from the testbeam campaigns and laboratory measurements for the n^+ -in-n planar pixel sensors with respect to the IBL specifications.

7.2.1. Cooling and temperature dependencies

The sensor cooling during testbeam was realised, as described in 6.2.2, with dry ice. One of the main challenges during the testbeam campaigns is the compatability between the measurements caused by the difference of the sensor temperature among others. The sensor temperature varies between -15°C and -40°C . This variation is caused by the sublimation of the dry ice over the runtime. The variation of the temperature is visible in the variation of the current. An example of this is given in figure 7.1.

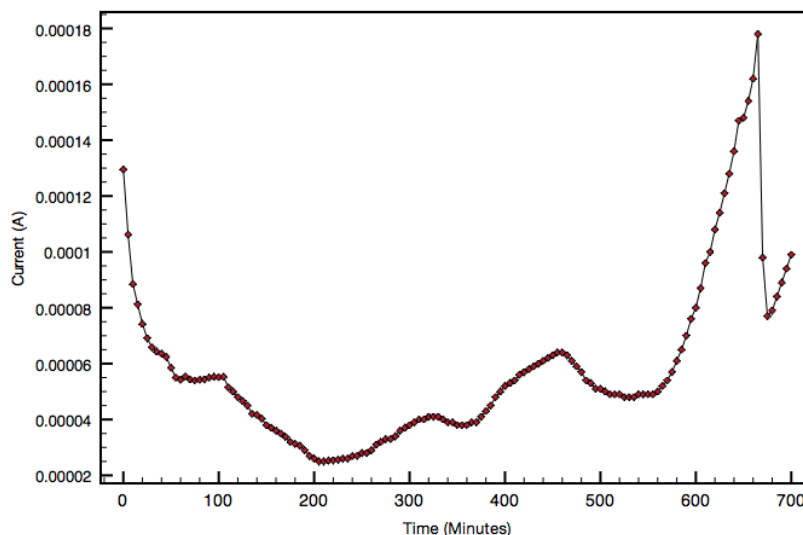


Figure 7.1.: Logged current values of LUB2 during the IBL testbeam in April 2011 at -1000 V plotted against time.

To have a stable temperature during the runs and to fulfil the requirements for the sensor temperature counter heating to -15°C with a heating resistor was tried. The temperature was measured directly on sensor. The placing of the Pt1000 and the heating resistor is given in figure 7.2 and 7.3. The result of the counter heating during runtime is shown in figure 7.4. The maximum peak to peak variation is 7 degrees. Contingent on that the current varies about 0.11 mA , see figure 7.5. This method is not constructive as the slow changing in temperature and resulting of that the change in the leakage current, is better for a stable functionality of the devices.

The changing of temperature has also an influence on the efficiency of the device due to noise effects. The second influence on the analysis is the shift of alignment due to the melting dry ice and the weight movement. Because of that it is better for the reconstruction and analysis of the testbeam measurements not to counter heat during the runtime.



Figure 7.2.: Heatingresistor mounted on the backside of LUB4.

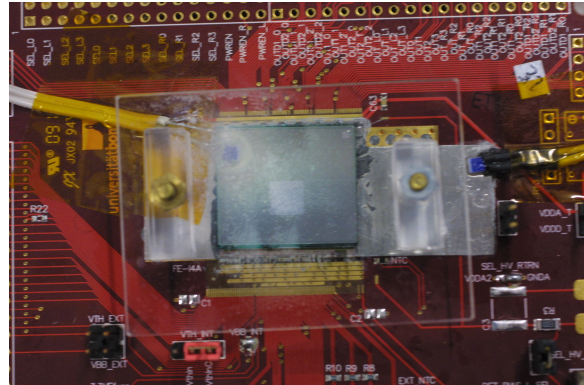


Figure 7.3.: PT1000 positions directly on sensor and on the aluminium carrier.

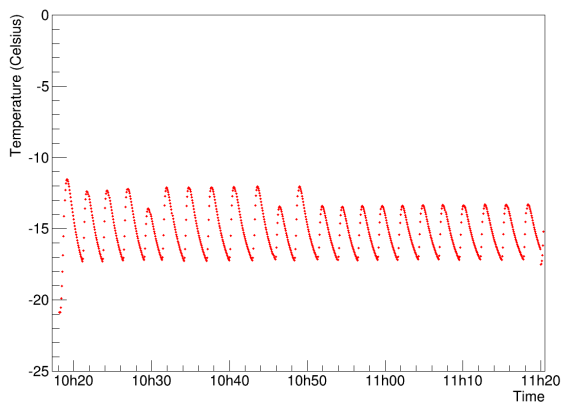


Figure 7.4.: Time vs temperature of LUB4 during IBL testbeam September 2011.

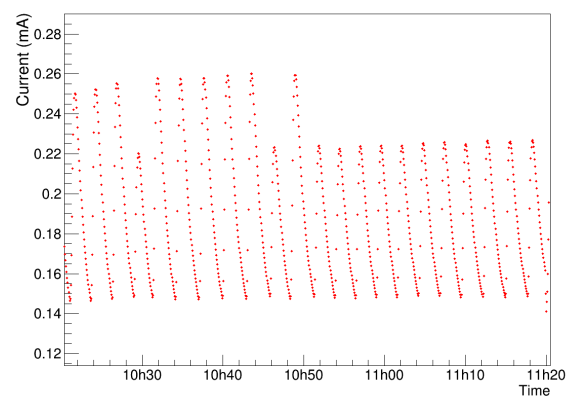


Figure 7.5.: Time vs current of LUB4 during IBL testbeam september 2011.

7. Results of Lab and TestBeam Measurements

To investigate whether the sensors can fulfil the requirements for the pixel current and the requested power dissipation for the hole SCA, currents, voltages and temperatures were written down during the testbeam measurements. With formula 3.6 the currents can be converted to -15°C . Table 7.2 shows the required values for every IBL-like sensor. The active area of a FE-I4 single chip is $3,38\text{ mm}^2$ and is important for the calculation of the power dissipation:

$$\text{Power dissipation}(mW/cm^2) = \frac{I \cdot U}{\text{active area}} \quad (7.1)$$

All sensors, even the higher irradiated ones, fulfil the requirements except LUB2. The reason therefor could be the temperature measurement or a damage of the sensor. LUB4 that fits into the requirements is further neutron irradiated than LUB2.

Table 7.2.: Current of the IBL testbeam sensors at -1000V scaled to -15°C , the current per pixel and the power dissipation.

Sensor	Current (uA)	Current per pixel (nA)	Power dissipation (mW/cm ²)
LUB 2	910	33.9	269
LUB 4	210	7.8	62
PS 1	527	19.6	156
PS 2	250	9.3	74
SCC 60	300	11.2	89
SCC 61	320	12	95

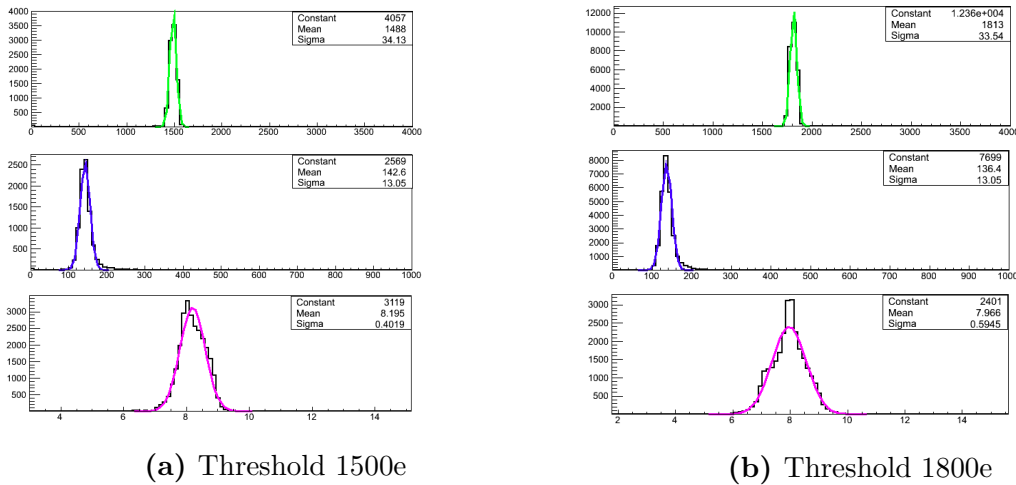
7.2.2. Sensor efficiencies

As mentioned in section 6.3.2 the sensor efficiency was one of the main measurements of the testbeam campaigns and the results for four different assemblies will be presented.

The sensor assembly that fulfils the IBL criteria completely is PS2. PS2 has a thickness of $200\text{ }\mu\text{m}$, a slim edge design with an inactive edge of $200\text{ }\mu\text{m}$, a uniform pixel size of $250 \times 50\text{ }\mu\text{m}^2$ and has been irradiated with protons in the CERN PS up to a fluence of $5 \cdot 10^{15}\text{ n}_{eq}\text{ cm}^2$.

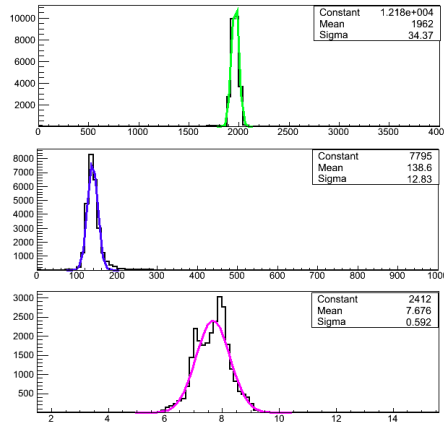
During the IBL testbeam campaign at DESY in March 2012 PS2 runs under different conditions by varying the threshold (1500 e; 1800 e; 2000 e) and the bias voltage (600 V; 800 V; 1000 V). The sensors were mounted in the DOBox on wedges (see figure 6.12), that the beam incidence angle was 15° . This angle simulates the tilt of the staves in the IBL. The reference DUT for the runs was an unirradiated 3D device called FBK13. FBK13 was tuned and kept constant to a threshold of 1600 e with a ToT of 6 for 20 ke at a bias voltage of 20 V. An efficiency map for FBK13 can be seen in figure 6.29.

Figure 7.6 shows all tunings for PS2 with the corresponding noise for every threshold. The desired ToT is 8 for 10 ke. The noise for all threshold steps is less than 150 e and the threshold distributions have a sigma smaller than 35.



(a) Threshold 1500e

(b) Threshold 1800e



(c) Threshold 2000e

Figure 7.6.: Tunings of PS2 for each threshold step measured in the IBL testbeam in March 2012. In every histogram the threshold is shown in green, the corresponding noise in blue and the ToT at 10ke in magenta.

The huge influence of a reasonable tuning and the need of a high voltage adjusted to the fluence is displayed in figure 7.7. The figure shows the LVL1 distribution during the testbeam runs without any cuts. When the bias voltage is decreased to a value below the depletion voltage the noise floor of the assembly increases. A higher threshold also disables the assembly noise. For a threshold of 1500 e at 600 V the noise floor is at 16 % of the peak high with a higher bias voltage of 1000 V the noise floor is at 7 % of the peak high (see figure 7.8). For the 500 e higher threshold of 2000 e the noise floor is 3 % of the peak high at 600 V and 2 % of the peak high at 1000 V. The only LVL1 distributions that do not fit belong to the threshold of 1800 e.

The reason for that can be found in the hitmap, also without any cuts like the LVL1 distributions, shown in figure 7.9. Extremely noisy pixel are visible in the lower left corner and in the edge columns on the right side and on the left side of the sensor. Due to that the measurements for the threshold of 1800 e and also for 2000 e were done with a pixel mask loading into the configuration of the assembly. Concerning to these noise effects the analysis of the efficiency with TBMon runs with a Hotpixel finder to avoid a shift of the results due to noisy pixel. As it can be seen in the efficiency map (figure 6.29) the coverage for the sensor efficiencies reproduces most of the sensor.

7. Results of Lab and TestBeam Measurements

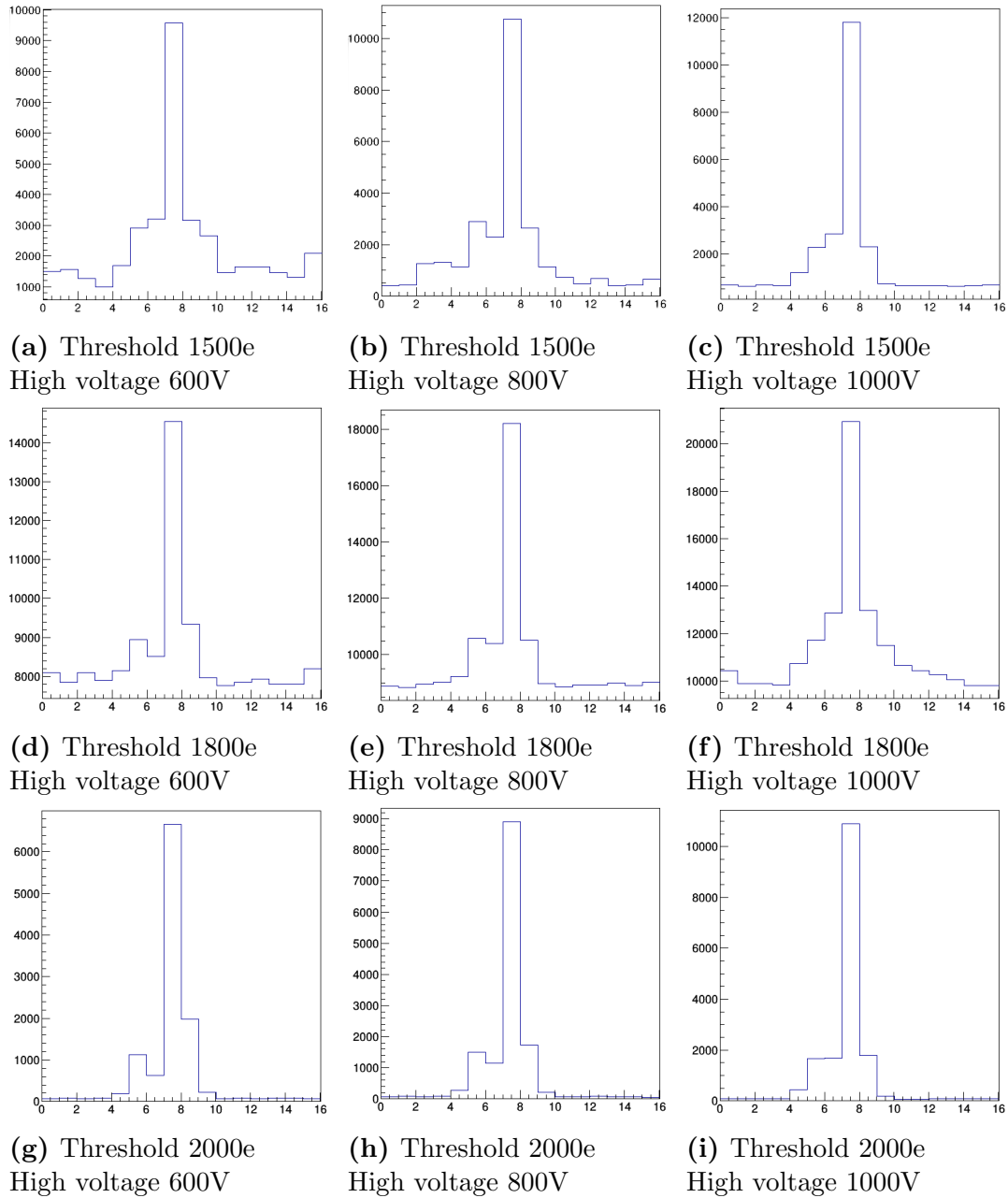


Figure 7.7.: LVL1 distribution for PS2 at all applied voltages and all adjusted thresholds during the IBL testbeam in March 2012.

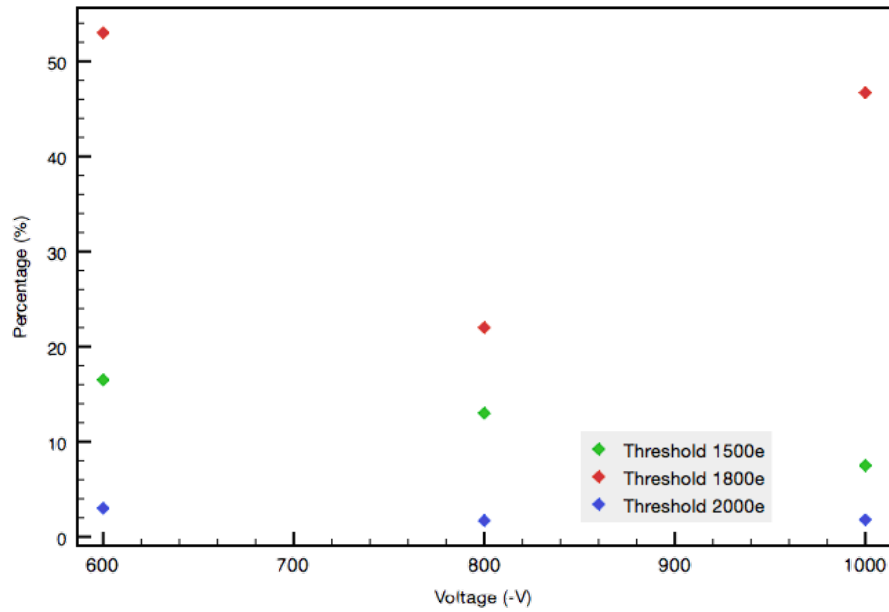


Figure 7.8.: Percentages of the noise floor with respect to the peak height for every threshold and bias voltage.

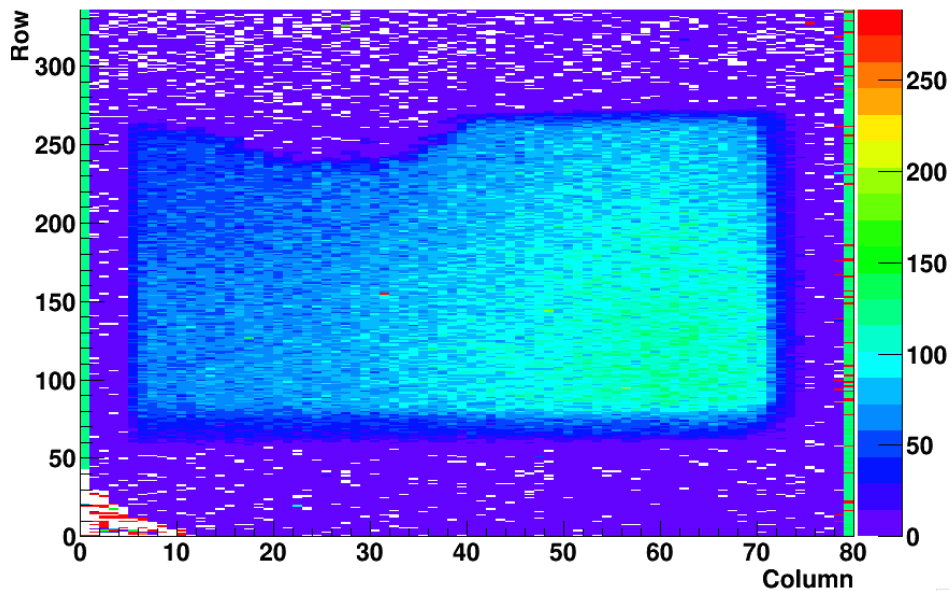


Figure 7.9.: Hitmap of PS2 from the IBL testbeam in March 2011 at 600 V with a threshold of 1800 e without any cuts.

7. Results of Lab and TestBeam Measurements

The average efficiencies for PS2 are shown in figure 7.10. In general one can say the lower the threshold the higher the efficiency and the higher the bias voltage the higher the efficiency. PS2 fulfils at 1000 V the IBL requirements by having an efficiency of more than 97%.

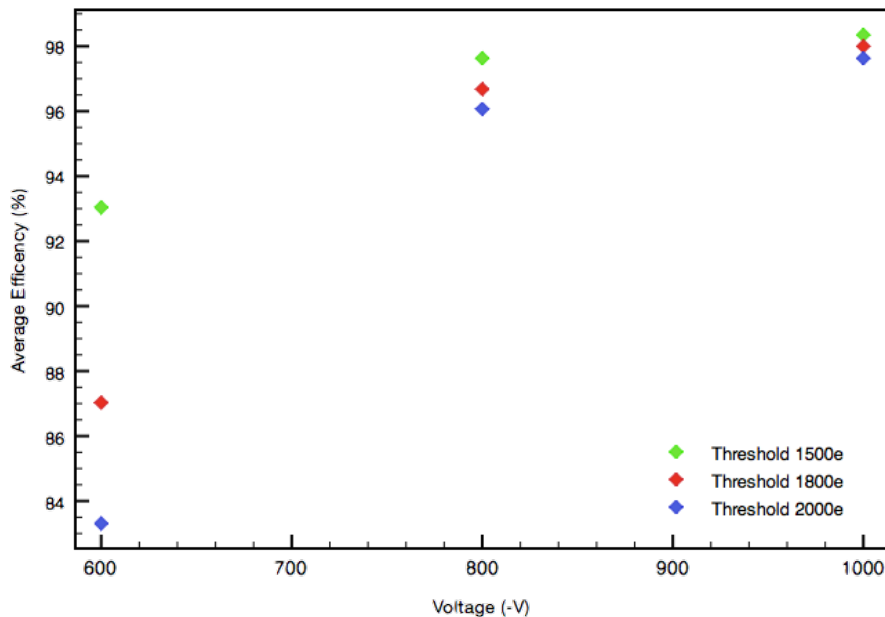


Figure 7.10.: The average efficiency of PS2 during the IBL testbeam in March 2012 in dependency of the applied bias voltage and the threshold.

Another assembly that was investigated during testbeam campaigns is SCC61. It is irradiated with low energy protons at KIT (see section 5.2) up to a fluence of $6 \cdot 10^{15} n_{eq} cm^2$ which is more than the required fluence for the IBL. SCC61 has a thickness of $200 \mu m$ and the slim edge design.

Due to the low energy proton irradiation the readout electronic is heavily damaged. This is clearly visible in the analog and digital scan of SCC60, which is identical to SCC61, shown in figure 7.11. The scans show more than 1000 broken and noisy pixel. Broken pixel are pixel with an entry of 0 and noisy pixel are pixel with an entry unequal 0 or 200.

This effect was observed for all proton irradiated assemblies, also for the 3D ones. This issue was investigated in lab measurements with different conditions like different thresholds, bias voltages and temperatures. The changing of the bias voltage and the temperature have no influence on the number of broken and noisy pixel. The threshold tuning has an influence, the higher the threshold the lower the broken and noisy pixel but there are still broken and noisy pixel.

To operate these assemblies as good as possible some adjustable DAC values were changed and the results investigated. By changing the value of Amp2Vbpf, which is the feedback current in the second amplifier stage, a lot of noisy and broken pixel came back to life.

SCC61 was measured in the IBL testbeam in June 2011 with a threshold of 1600e a corresponding ToT of 8 at 10 ke at a bias voltage of 600 V, 800 V and 1000 V. The success of the tuning to 1600e is displayed in figure 7.13. It is clearly visible in the threshold map on top of the picture that a lot of pixel are not tuneable and the threshold

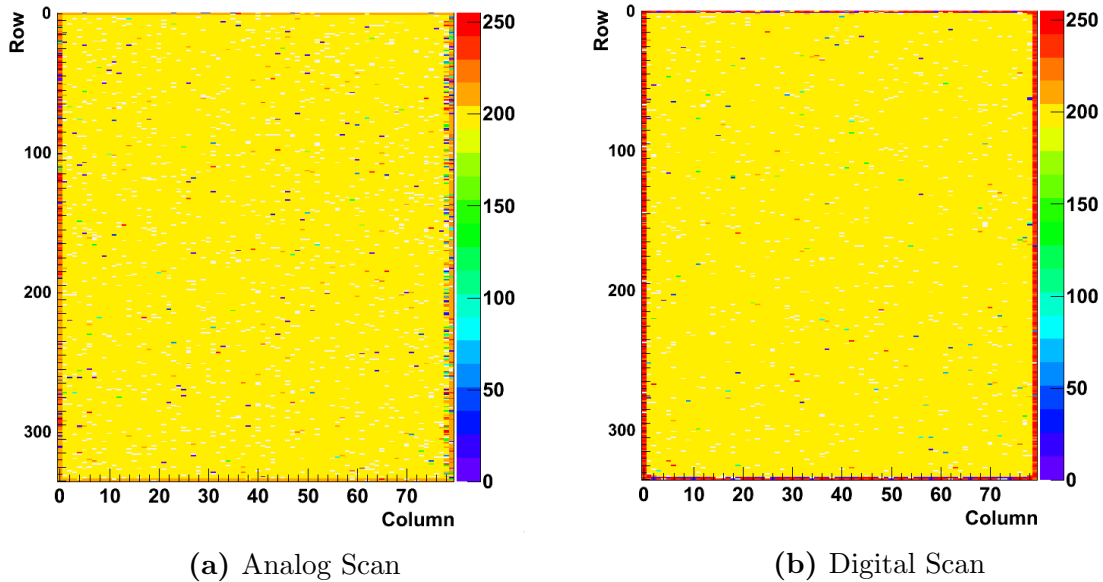


Figure 7.11.: Analog and digital scan of SCC60.

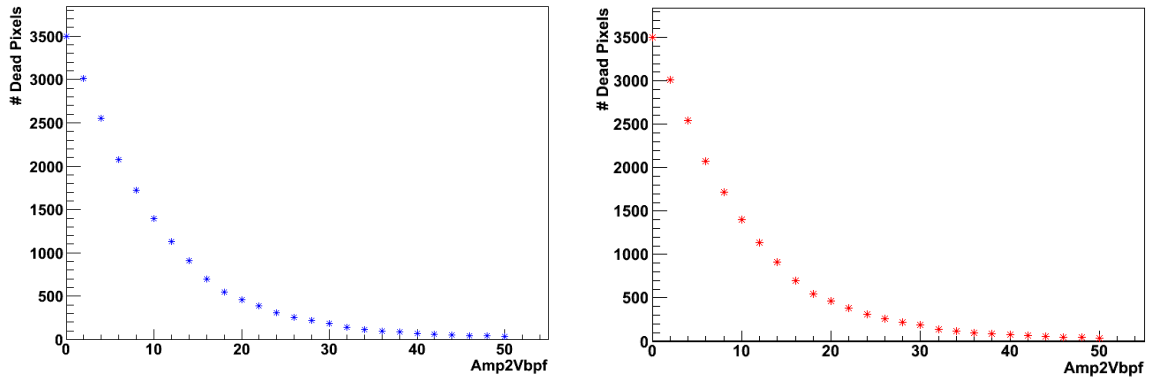


Figure 7.12.: Dependency of dead pixel on the value of Amp2Vbpf for the analog (left) and digital (right) part of the FE-I4.

distribution has a width of ~ 300 e. The corresponding noise is in comparison to the noise for the PS2 tuning a lot higher with approximately 250 e. This high noise of SCC61 is also visible in the LVL1 distribution during the testbeam measurements. The LVL1 distribution at the three different bias voltages is shown in figure 7.14. The chronology of the measurements were 1000 V, 600 V and 800 V. This is relevant for the understanding of the huge difference in the peak height to noise floor ratio. Between every bias voltage step the pixel mask was adjusted to lower the noise entries of the measurements. This lowers the ratio from approximately 48 % at 1000 V to a noise floor of 3 % of the peak height at 800 V. This difference is also visible in the raw hitmaps, the comparison for 600 V and 800 V is displayed in figure 7.15. With this masks it was possible to operate the assembly successful but during the reconstruction and analyses of the data the neighbour pixel of each masked pixel were automatically masked. This results in an efficiency map which clearly shows that the calculation of the efficiency for this assembly is not representative (figure 7.16). Nevertheless the calculated efficiencies for the different bias voltage steps are summarized in figure 7.17. The efficiency values reflect the huge radiation damage of the assembly and especially of the FEI-4 due to the low-energy protons.

7. Results of Lab and TestBeam Measurements

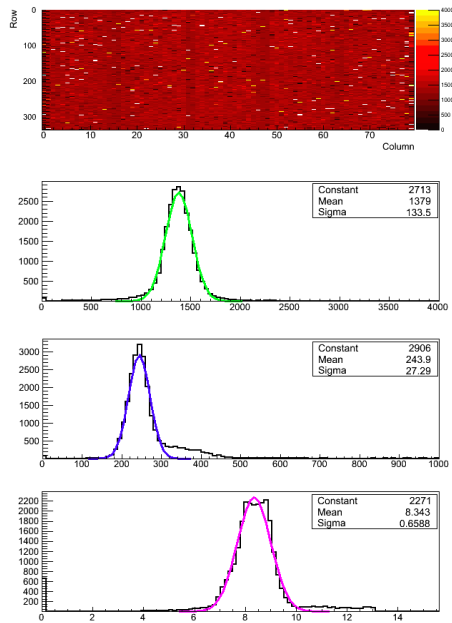


Figure 7.13.: Tuning of SCC61 to a desired threshold of 1600 e with the corresponding noise and ToT at 10 ke.

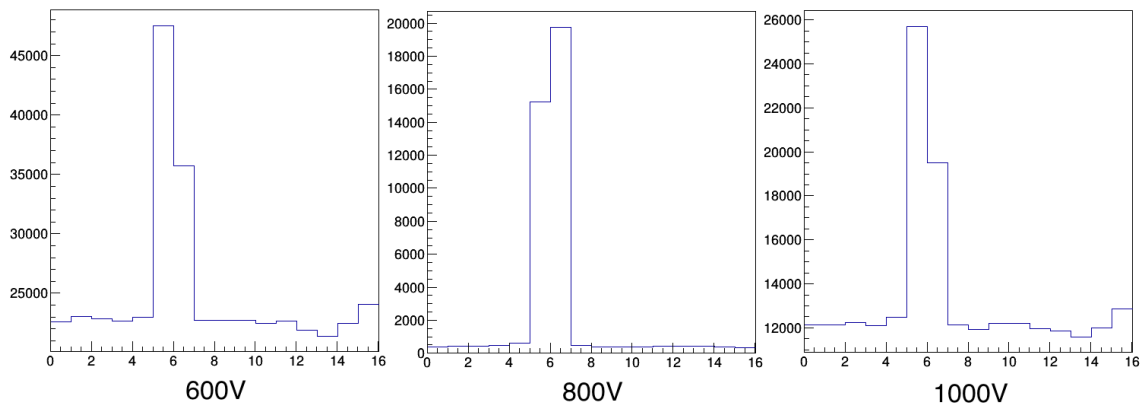


Figure 7.14.: LVL1 distribution for SCC61 during the IBL testbeam in June 2011 for every applied bias voltage without cuts.

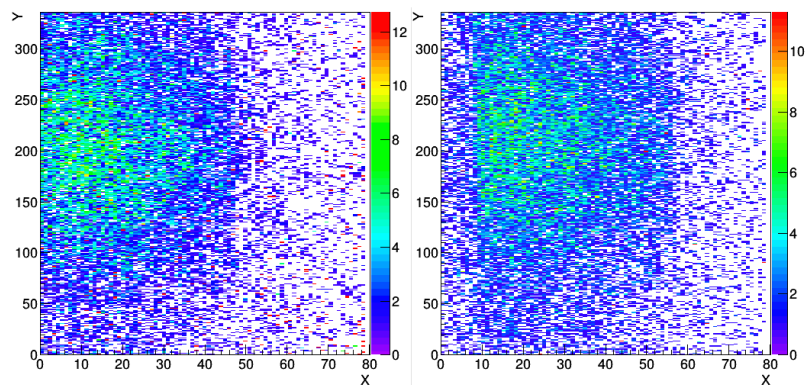


Figure 7.15.: Raw hitmap of SCC61 with a threshold of 1600 e at 600 V (left) and 800 V (right).

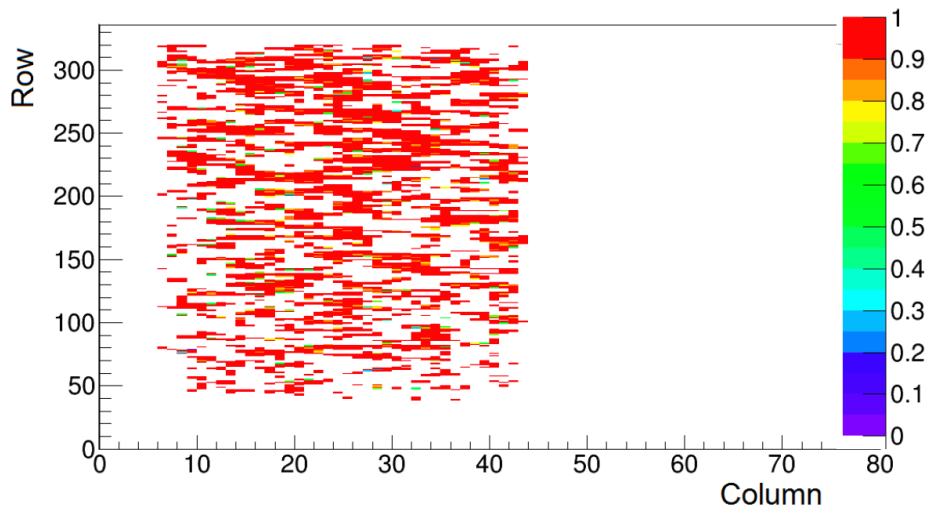


Figure 7.16.: Efficiency map of SCC61 at a threshold of 1600 e and an applied bias voltage of 800 V.

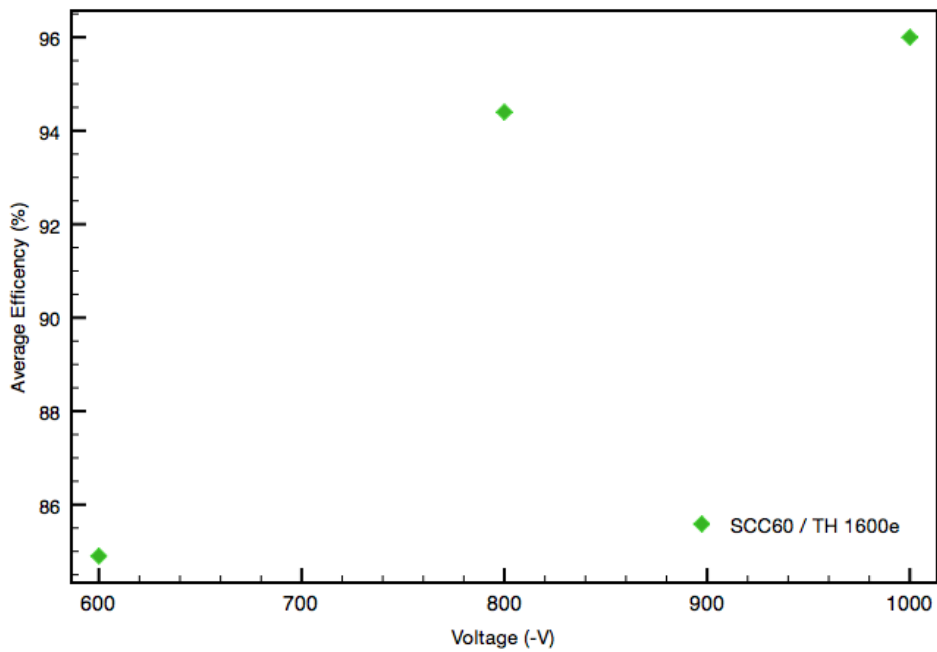


Figure 7.17.: The average efficiency of SCC61 during the IBL testbeam in dependency of the applied bias voltage at a threshold of 1600 e.

7. Results of Lab and TestBeam Measurements

The last IBL assemblies that will be discussed in this thesis are LUB2 and LUB4. They were both neutron irradiated at the JSI-Triga in Ljubljana (section 5.2). LUB2 has a thickness of $250\ \mu\text{m}$ and the IBL slim edge design, it was irradiated up to a fluence of $4 \cdot 10^{15}\ \text{n}_{eq}\text{cm}^2$. LUB4 has also the slim edge design and is $50\ \mu\text{m}$ thinner with the desired IBL sensor thickness of $200\ \mu\text{m}$. The fluence is $5 \cdot 10^{15}\ \text{n}_{eq}\text{cm}^2$.

The tuning for LUB2 in the IBL testbeam in June 2011 and for LUB4 during the IBL testbeam in September 2011 are shown in figure 7.18. The desired threshold for both was 1600 e but LUB2 actual ran with a adjusted threshold of 1100 e. The noise floor of the LVL1 distribution for LUB2 is for the different bias voltage in the range of 3-5 % in comparison to the peak high.

The LVL1 distribution for LUB4 has a noise floor in the order of 20 % to the peak high. Column 31 of the FE-I4 that was bump-bonded to the sensor has some issues as one can see in the raw hitmap at 1000 V in figure 7.19. This column was not mask during the testbeam measurements and has an influence on the noise level. The average efficiency for LUB2 and LUB4 is shown in figure 7.21. At the required bias voltage of 1000 V both assemblies have a higher efficiency than 97 %.

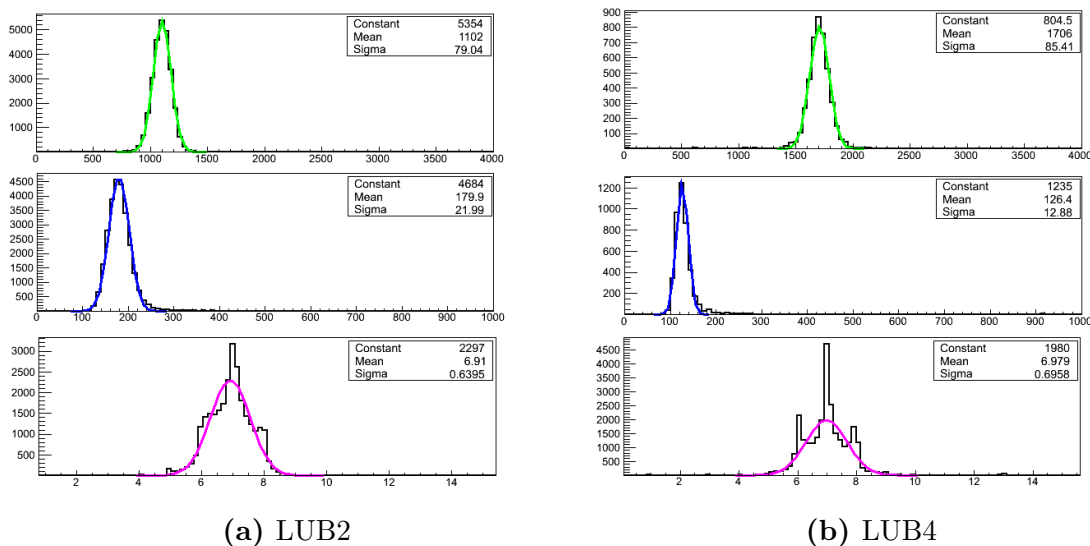


Figure 7.18.: Tunings for LUB2 (left) and LUB4 (right) during their testbeam campaigns. The desired threshold for both were 1600 e. The ToT for LUB2 was 5 at 20ke and for LUB4 8 ToT at 10ke.

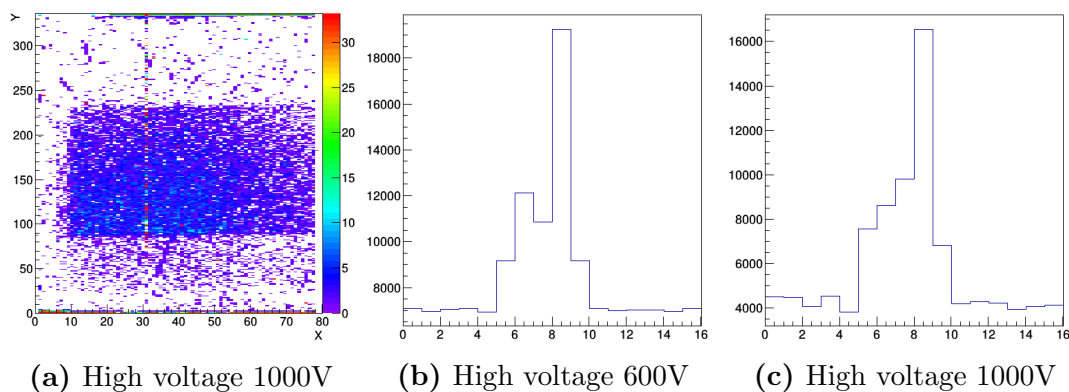


Figure 7.19.: LVL1 distribution for LUB4.

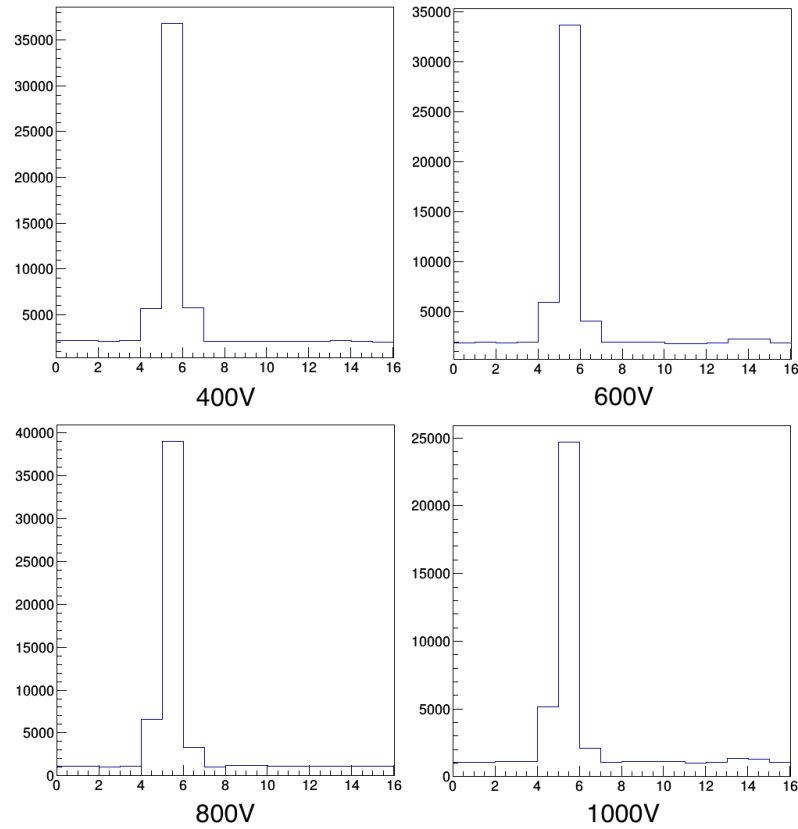


Figure 7.20.: LVL1 distribution for LUB2.

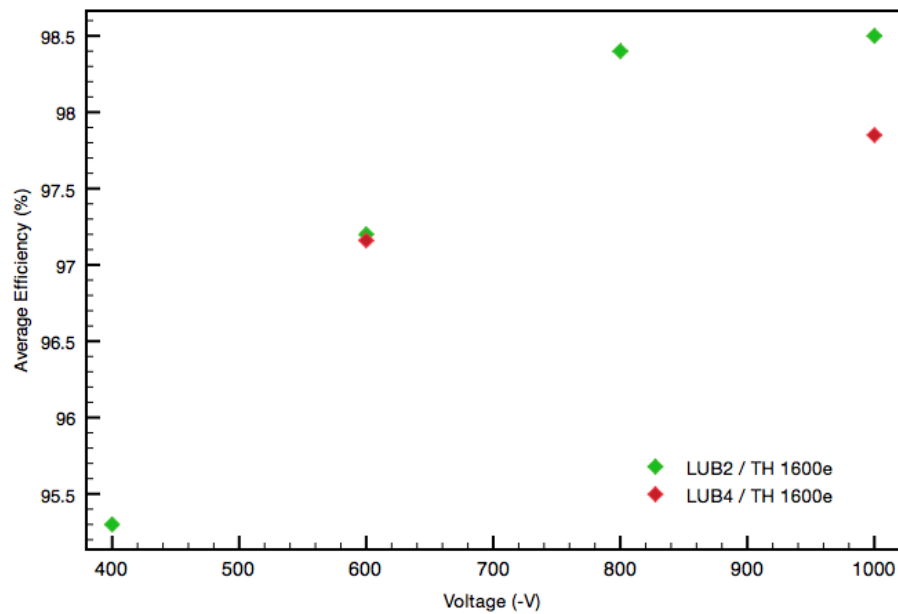


Figure 7.21.: The average efficiency of LUB4 during the IBL testbeam in and LUB2 during the IBL testbeam in dependency of the applied bias voltage at a threshold of 1600 e.

7.2.3. Edge efficiency

The SCA LUB2, as mentioned in the sensor efficiency section, was operated at four different bias voltages with a threshold set to 1600 e in the IBL testbeam in June 2011. Here the edge efficiency for the slim edge design is focused.

Figure 7.22 shows the hit efficiency plots of the edge area for each applied bias voltage and a projection to the long pixel side. At the edge region of the long edge pixel a S-curve fit is applied. When the hit efficiency at the end of the pixel cell is 50 % the edge pixels are defined as fully efficient. With increasing bias voltage the efficiency grows over the edge pixels. At a bias voltage of 1000 V the edge pixels is fully active and efficient over the full length. The efficiency drop to zero close to 500 μm at the pixel edge most likely occurs due to the geometric end of the pixel. For a bias voltage of 1000 V the inactive edge has a width of approximately 196 μm .

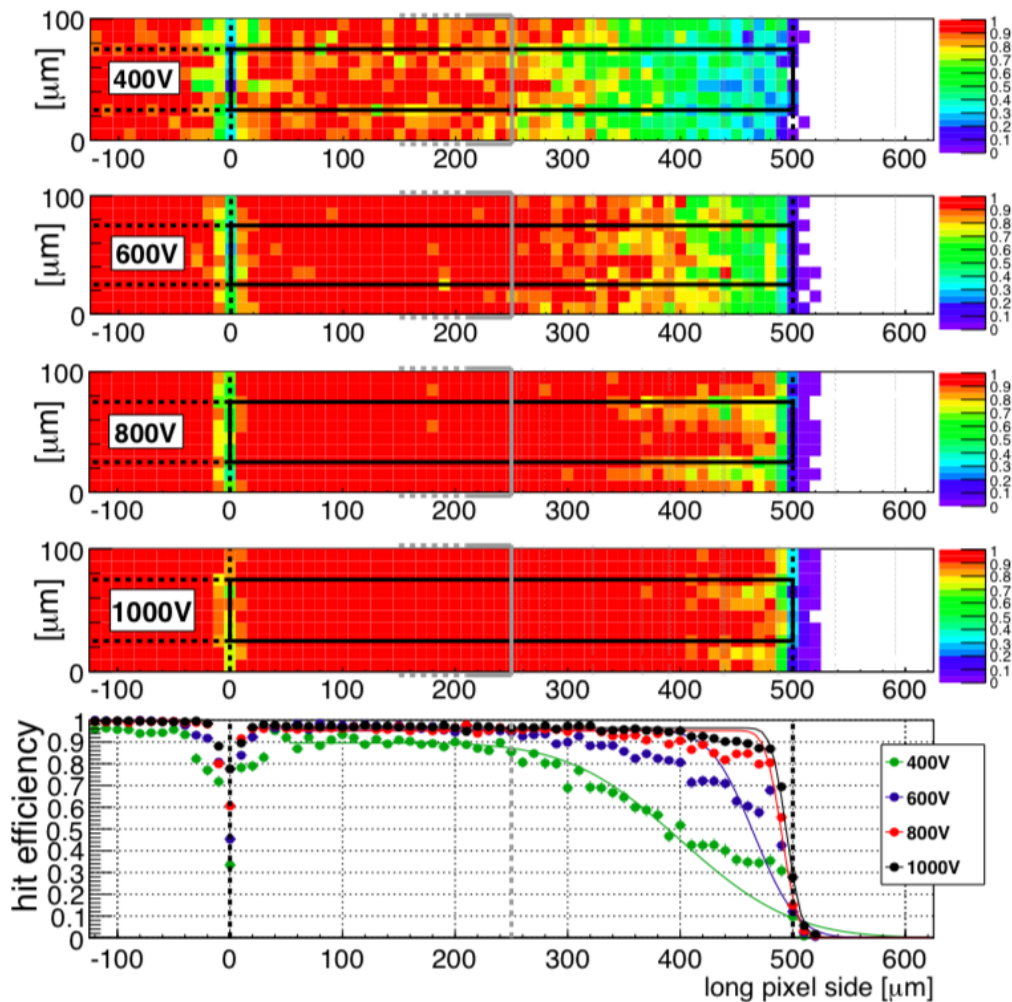


Figure 7.22.: Hit efficiency maps of the edge of LUB2 at four different bias voltages. LUB2 was tuned to a threshold of 1600 e. The pixel cell contours are marked in black and the high voltage pad at 250 μm and the guard rings are marked in grey. [6]

7.2.4. Summary of the IBL sensors measurements

The planar n^+ -in- n assemblies fulfill the defined IBL conditions. The sensors operate stable at a sensor temperature of -15°C and the power dissipation of the whole assembly at a bias voltage of 1000 V is below $200\text{ mW}/\text{cm}^2$, except for LUB2. But LUB2 fulfill like all the other assemblies the requirement for the leakage current per pixel below 100 nA . The inactive edge of the sensors is through the new edge design (section 4.2.1) $200\text{ }\mu\text{m}$ wide. This is $25\text{ }\mu\text{m}$ less than the required $225\text{ }\mu\text{m}$. The average efficiency limit of 97% after a irradiation up to a fluence of $5 \cdot 10^{15}\text{ n}_{eq}\text{cm}^2$ was trespassed with this devices at 1000 V .

Due to these scientific findings the IBL management decided to build the central part of the IBL with $200\text{ }\mu\text{m}$ thick n^+ -in- n planar slim edge sensors.

7.3. Magnetic Czochralski sensors

The next section gives an overview on the investigations of MCz and DOFZ¹ assemblies. Both silicon materials will be compared with each other in terms of leakage current, efficiency and charge collection unirradiated as well as irradiated with charged hadrons or/and neutrons.

Charged hadrons introduces negatively charged acceptors by irradiation of FZ material. In MCz material the creation of positively charged shallow donors dominates. The irradiation of FZ and MCz with neutrons introduce approximately the same rate of active acceptors. [44]

The assemblies that were investigated and compared with each other are MCz1, MCzPi and FZPi. MCz1 is a $285\text{ }\mu\text{m}$ thick, unirradiated FE-I4 assembly with the IBL slim edge design. MCz1 was measured in a testbeam in March 2013 at four different threshold and each threshold at three different bias voltages. MCzPi is an assembly that was irradiated with pions at PSI (section 5.2) up to a fluence of $5 \cdot 10^{14}\text{ n}_{eq}\text{cm}^2$ and is $285\text{ }\mu\text{m}$ thick. The investigated FZ assembly is FZPi, like MCzPi it was irradiated with pions at PSI up to a fluence of $5 \cdot 10^{14}\text{ n}_{eq}\text{cm}^2$ and its thickness is $200\text{ }\mu\text{m}$.

7.3.1. IV and CV Measurements

IV measurements were done before and after irradiation. Before irradiation the temperature during data taking was not regulated and was 23°C , room temperature. After irradiation the samples were cooled with the chiller down to a sensor temperature, measured with a PT1000, of -15°C . The IV curves for the MCz sensor are shown in figure 7.23 and for the DOFZ sensor in figure 7.24.

Before irradiation the leakage current of the MCz sensor is much lower than the leakage current of the FZ sensor. For example at a bias voltage of 100 V the leakage current for the MCz is $0,009\text{ }\mu\text{A}$ and for the FZ $0,68\text{ }\mu\text{A}$. It is no to go up to a bias voltage of 500 V with an unirradiated MCz sensor this is a difference to unirradiated FZ sensors. Unirradiated FZ sensor have a break down at less than 300 V . This turns after irradiation at a bias voltage of 500 V the FZ has a leakage current of $58,5\text{ }\mu\text{A}$ and the current for the MCz is nearly three times higher with $157\text{ }\mu\text{A}$. Applying a bias voltage of 1000 V is no issue for both sensors.

7. Results of Lab and TestBeam Measurements

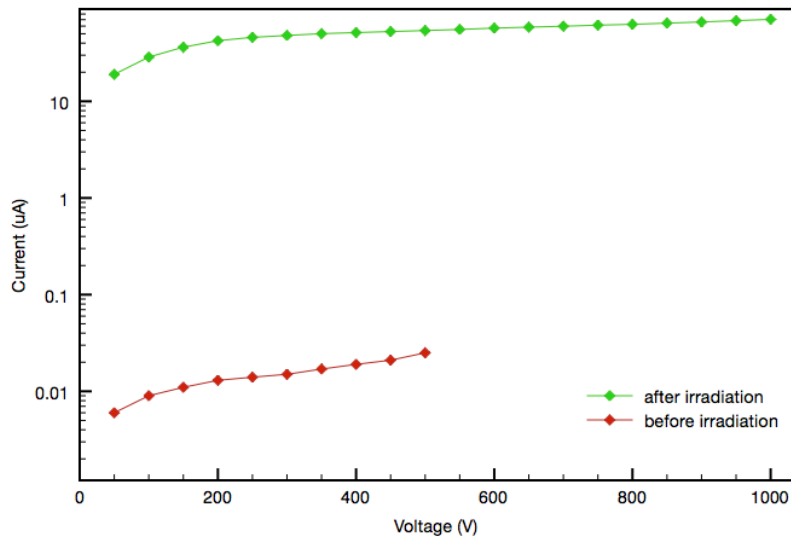


Figure 7.23.: IV curve of MCzPi before and after pion irradiation. Measurement done before irradiation at room temperature after at -15°C on sensor.

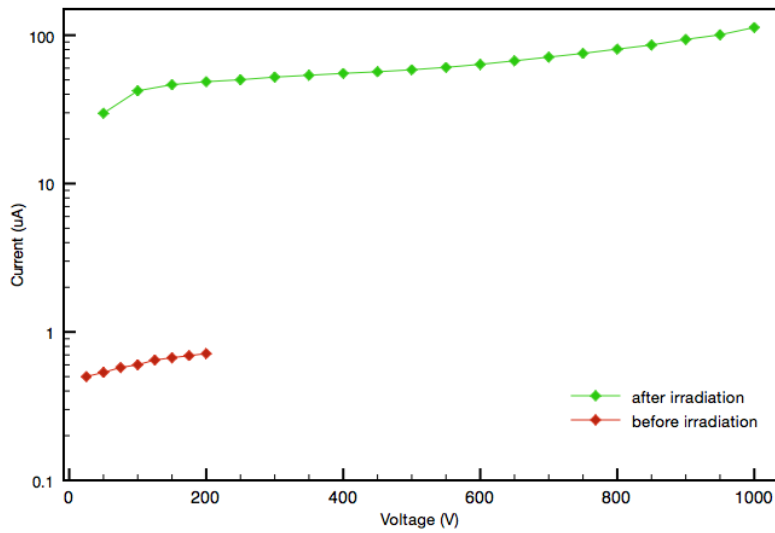


Figure 7.24.: IV curve of FZPi before and after pion irradiation. Measurement done before irradiation at room temperature after at -15°C on sensor.

The exemplary CV curves shown in figure 7.25 and 7.26 were taken with unirradiated MCz and FZ FE-I4 single chip sensors without a bump-bonded FE-I4. The depletion voltage for MCz is 350 V and for FZ 90 V. A CV measurement after irradiation is not possible as the irradiation was done with the hole assembly after bump-bonding and a CV measurement is only feasible with bare sensors.

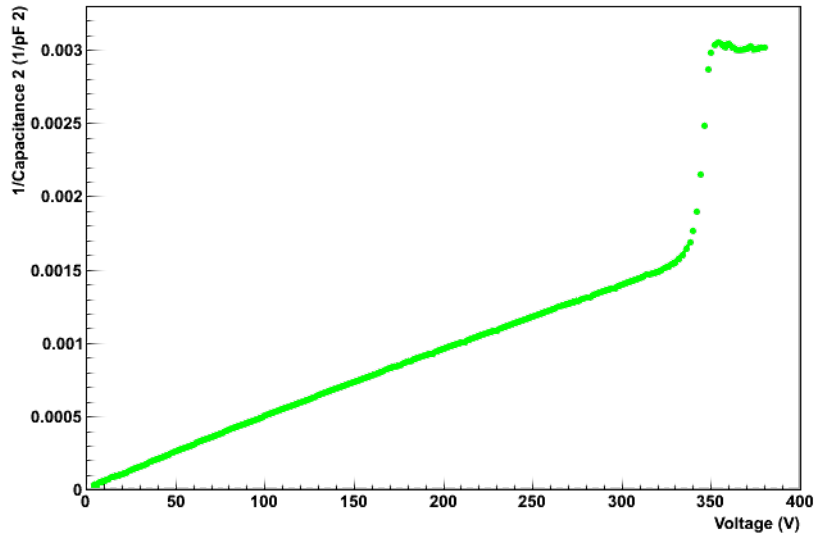


Figure 7.25.: CV curve of a unirradiated MCz sensor.

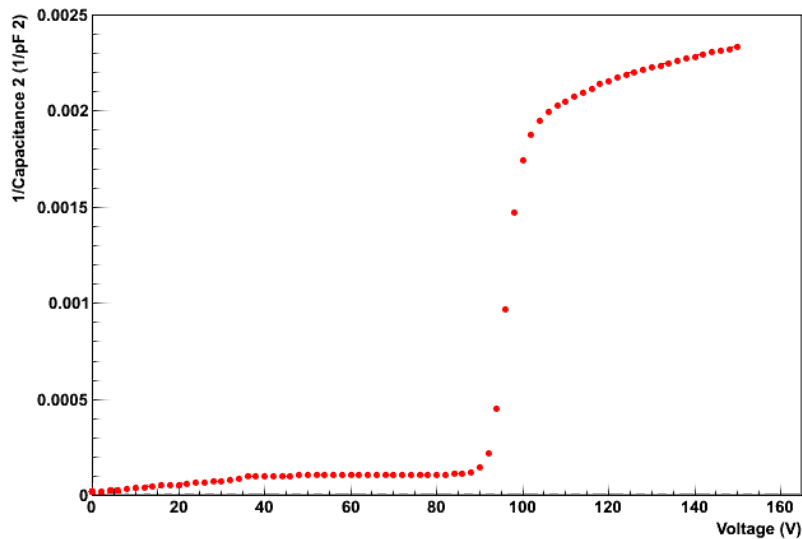


Figure 7.26.: CV curve of a unirradiated DOFZ sensor.

7.3.2. Tuning before and after irradiation

The tuning of the assemblies gives no surprises before or after irradiation. The noise changes are displayed for the four thresholds in figure 7.27. One can see that the noise lowers as expected with higher threshold. There is no systematic difference between the MCz and FZ assemblies. The slightly higher noise after irradiation is expected due to the radiation damage of the assemblies. The only spike is the high, in comparison

¹Below FZ means always DOFZ.

7. Results of Lab and TestBeam Measurements

to the other thresholds and FZ, noise for the 2200 e threshold of the MCz before and after irradiation.

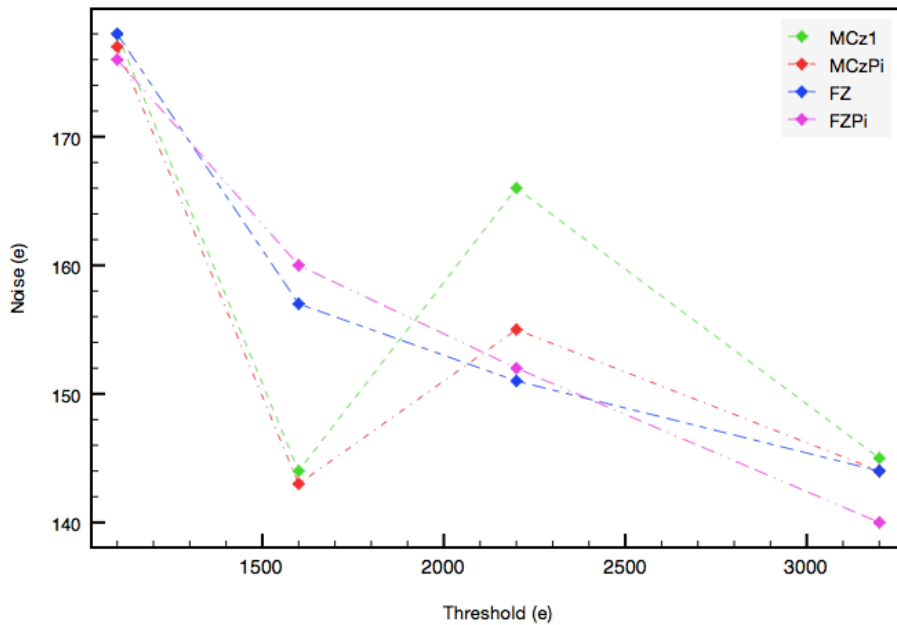


Figure 7.27.: Noise vs. threshold for MCz and FZ sensors before and after irradiation.

The complete histograms for the tunings before and after irradiation can be found in appendix A.2.

7.3.3. Testbeam measurements unirradiated

In the testbeam campaign in March 2013 at DESY (see section 6) MCz1 was measured at four different threshold and three different bias voltages. As MCz1 was unirradiated the testbeam measurements were done without cooling at room temperature. An exemplary hitmap and efficiency map of the runs with a bias voltage of 400 V and a threshold of 3200 e is shown in figure 7.28. The alignment of the telescope and the DUTs was good and this results in a huge enclosure of the device. Figure 7.29 shows

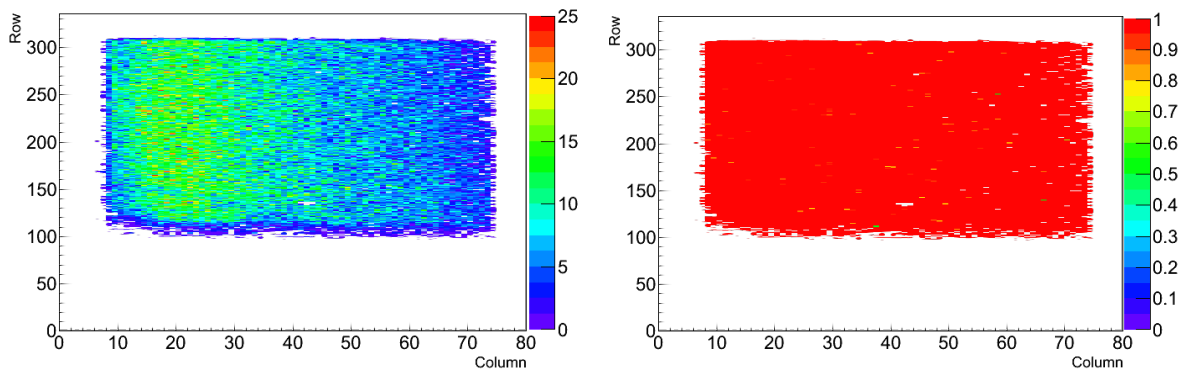


Figure 7.28.: Hitmap and efficiency map of MCz1 with a threshold of 3200 e at 400 V during the testbeam in March 2013.

the average efficiency for the threshold and bias voltage steps. All efficiencies are higher

than 98 %. The irreducible increase from a bias voltage of 350 V to 400 V is referable to the depletion voltage of the sensor. As one can see in the CV measurements the depletion voltage for MCz sensors is around 350 V.

This detailed measurement of an unirradiated MCz device is basic for the comparison of the changing from the efficiency after the irradiation steps.

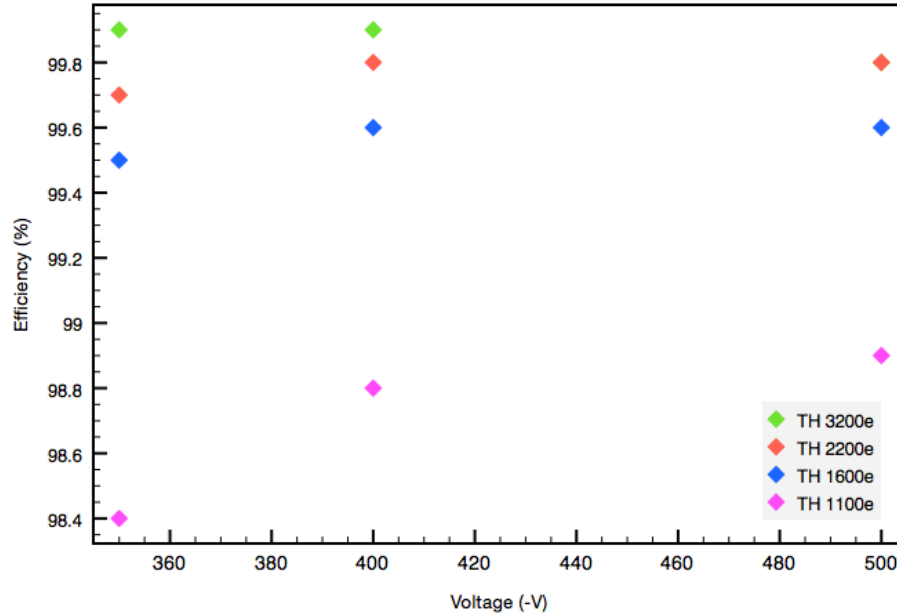
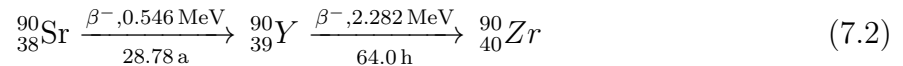


Figure 7.29.: Average efficiency of MCz1 from the testbeam in March 2013 for four thresholds in dependence of the applied bias voltage.

7.3.4. Measurements after pion irradiation

The first step after the irradiation of MCzPi and FZPi were tunings and source scans in the laboratory. The source scans were done with a Sr-90 source in the setup that was described in section 5.4. The Sr-90 isotope is embedded in a acrylic cylinder and the decay is according to the scheme:



over Y-90 to Z-90 by emitting two electrons with energies of 0.546 MeV and 2.282 MeV. These electrons are used as an substitute for ionising particles in the detector.

The SCA was cooled down to -15°C on sensor by using a chiller and the corresponding cooling plate.

The results for the source scans of FZPi at -500 V are shown in figure 7.30. The collected cluster charge is given in units of ToT. FZPi was tuned and measured at the thresholds of 1100 e, 1600 e, 2200 e and 3200 e. The ToT is for all thresholds 8 for 16 ke. On every histogram a convoluted Landau and Gaussian fitting function was adjusted. The Landau distribution describes the energy loss, while underground and noise are summarized in the Gaussian distribution.

7. Results of Lab and TestBeam Measurements

It can be seen that the effect on the collected charge is significant when going to higher thresholds. But with the highest threshold of 3200 e the charge distribution is better defined and the noise went down. This is also visible in the corresponding LVL1 distribution for the measurements (figure 7.31). The noise floor in comparison to the peak high lowers from 3,8 % for a threshold of 1100 e to approximately 1 % for 3200 e.

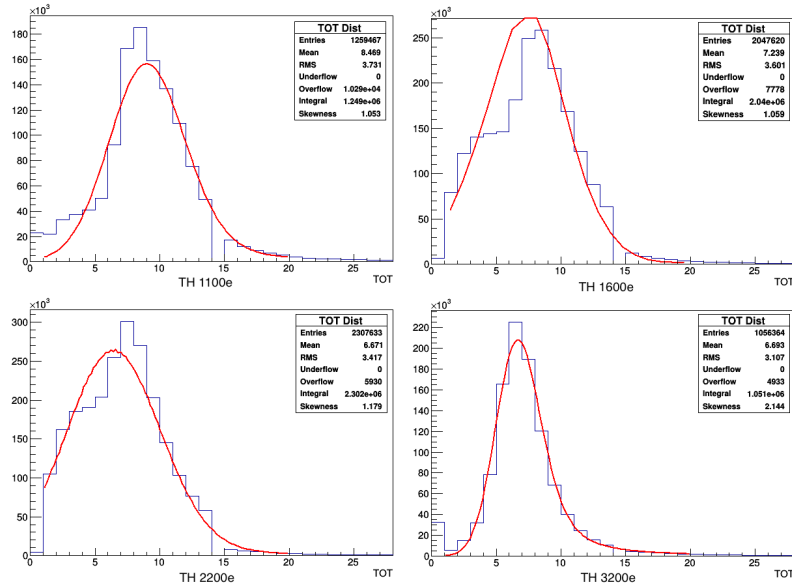


Figure 7.30.: ToT distribution of FZPi at a bias voltage of 500 V for four different thresholds and a ToT of 8 for 16 ke.

For the pion irradiated MCz sample the measurements were also done at two different bias voltages, -500 V and -800 V for the same thresholds. The collected cluster charge also in units of ToT for the -500 V bias voltage is shown in figure 7.32. The measurement at the threshold of 1100 e was corrupted and not analysable. Figure 7.32 shows instead the hitmap of the source scan to point out the good and nearly centric alignment of the source during the scans. The corresponding LVL1 distribution is given in figure 7.33. The results for a bias voltage of -800 e are shown in figure 7.34 and 7.35.

It can be seen that the noise level of the sensor has a big influence on the charge collection. The highest charge collection at -800 V and a threshold of 1600 e is correlated to the lowest noise floor to peak ratio of about 4,5 %. In general the noise level of the MCzPi is higher than the noise level of FZPi.

7.3.5. Summary of the MCz and FZ sensors

FZ and MCz samples were measured and irradiated once with pions with the aim to compare them with each other before and after every irradiation step. The testbeam measurements of the unirradiated MCz show good efficiencies that depend on the bias voltage and the threshold.

By now only lab measurements were done after the irradiation with pions. The noise level and the charge collection looks promising. The next step with these samples will be an irradiation with neutrons.

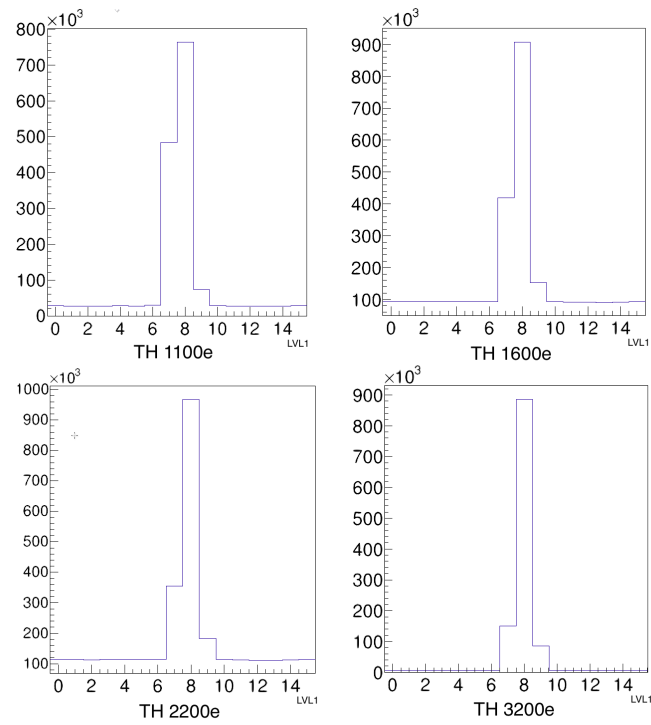


Figure 7.31.: LVL1 distribution for FZPi at a bias voltage of -500 V for four different thresholds.

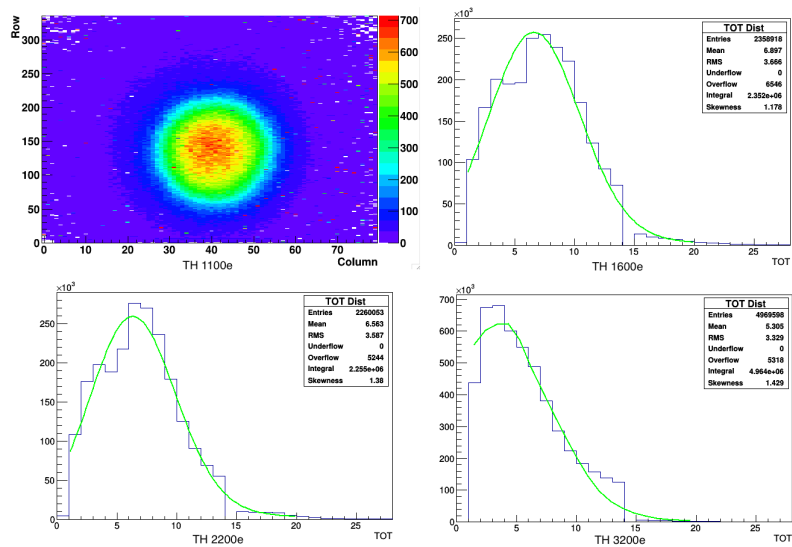


Figure 7.32.: Hitmap and ToT distribution of MCzPi at a bias voltage of 500 V for three different thresholds and a ToT of 8 for 16 ke.

7. Results of Lab and TestBeam Measurements

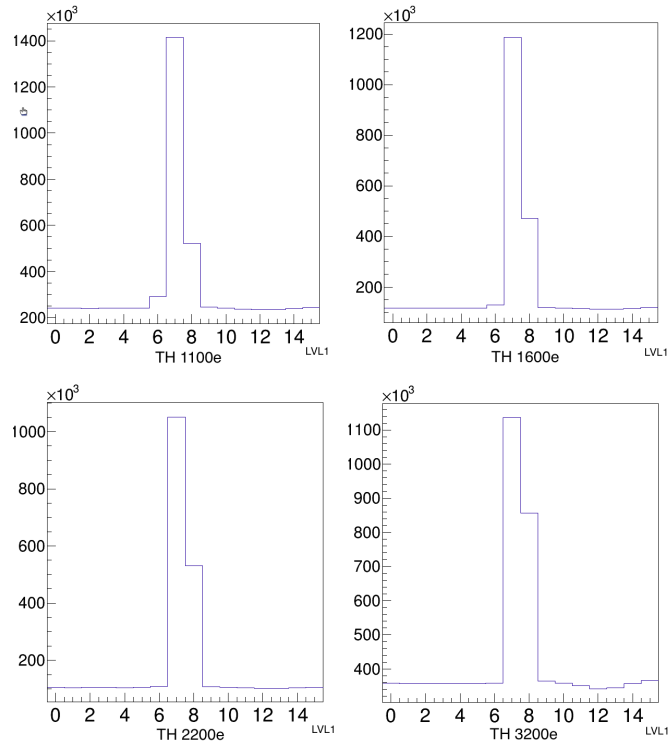


Figure 7.33.: LVL1 distribution for MCzPi at a bias voltage of -500 V for four different thresholds.

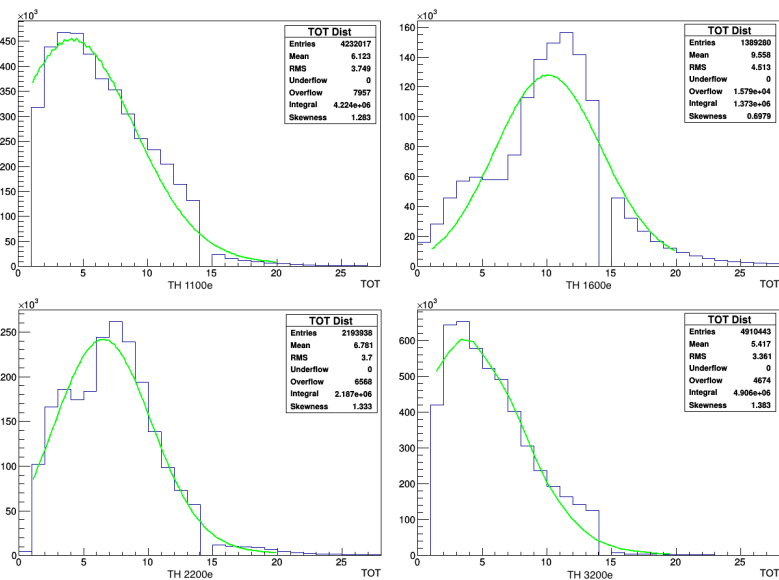


Figure 7.34.: ToT distribution of MCzPi at a bias voltage of 800 V for four different thresholds and a ToT of 8 for 16 ke.

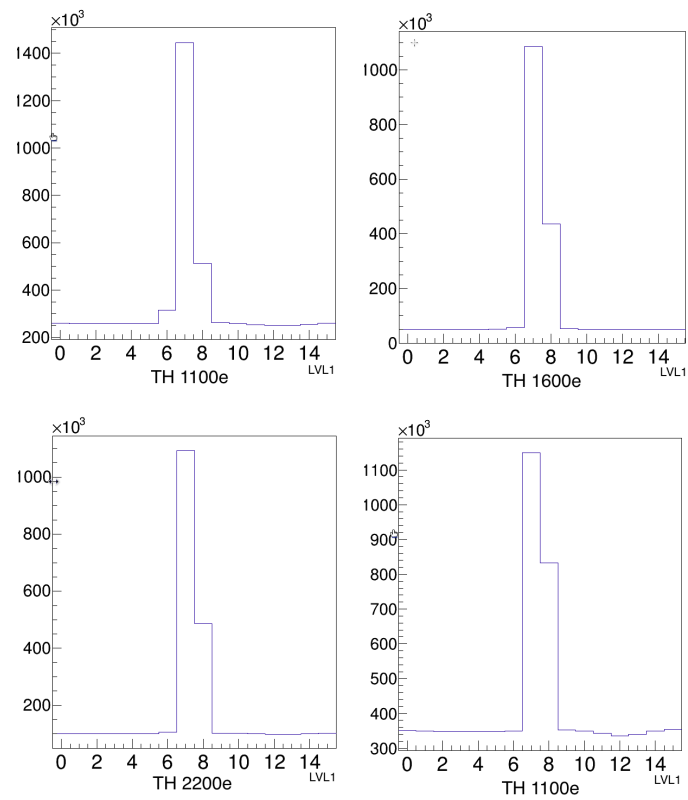


Figure 7.35.: LVL1 distribution for MCzPi at a bias voltage of -800 V for four different thresholds.

8. Conclusions and Outlook

The LHC¹ located at CERN² in Geneva circulated successfully a beam at 6.5 TeV after two years of shutdown in April 2015. During this shutdown a fourth pixel layer, called IBL³, was installed within the ATLAS⁴ pixel detector. The IBL will increase the tracking performance under high-luminosity conditions. Due to the extreme close location to the beampipe the IBL layer has to withstand higher fluences and particle rates than the rest of the pixel detector. This results in stringent conditions for the IBL sensors and the read-out electronic. These requirements are especially the efficiency above 97 % within the sensitive area of the sensor until the end of lifetime fluence of $5 \cdot 10^{15} \text{ n}_{eq} \text{ cm}^{-2}$ and a geometrical inefficiency below 2.2 %.

The work presented in this thesis has made a significant contribution for the IBL sensor decision. The IBL consists to 75 % of n⁺-in-n slim edge planar sensors.

To achieve this, testbeam measurements were done at DESY⁵ and CERN. The sensors together with the readout electronic, FE-I4, were irradiated with protons and neutrons up to the requested fluence of $5 \cdot 10^{15} \text{ n}_{eq} \text{ cm}^{-2}$ and measured afterwards in the testbeam campaigns. The slim edge sensors have proven that they fulfil all requirements for the IBL:

At a bias voltage of 1000 V and a temperature of -15°C the power dissipation of the hole sensors is below 200 mW/cm². The leakage current per pixel for this conditions is less than 100 nA. Due to the new pixel design it was possible to shrink the inactive edge to 200 μm. The average efficiency limit of 97% was trespassed with the irradiated assemblies.

The IBL was inserted into ATLAS in May 2014. In April 2015 the LHC circulated successfully a beam at 6.5 TeV and in May 2015 a beam at 13 TeV. The first plots of ATLAS with the IBL show promising results for the next run time with the IBL.

Besides the targeted measurements of the IBL sensors a comparison of Magnetic Czochralski (MCz) and Diffusion Oxygenated Float Zone (DOFZ) sensors were done. The measurements during a testbeam campaign at DESY with unirradiated sensors have shown sensor efficiencies above 98 % and a low noise level for four different thresholds and three different bias voltages. The next step is a mixed irradiation with charged hadrons and neutrons. Till now a MCz and DOFZ sensor were irradiated at PSI with pions up to a fluence of $5 \cdot 10^{14} \text{ n}_{eq} \text{ cm}^2$. The laboratory measurements shown no significant differences between the MCz and the DOFZ sensors.

This is promising for the planned testbeam measurements. After the systematic testbeam measurements the assemblies will be irradiated with neutrons and afterwards measured in a testbeam campaign and the laboratory.

¹Large Hadron Collider

²European organization for nuclear research (the acronym stands for: **C**onseil **E**uropeen pour la **R**echerche **N**ucleaire and is a remnant of the establishment)

³Insertable **B**-**L**ayer

⁴**A** Toroidal **L**H**C** **A**pparatu**S**

⁵**D**eutsches **E**lectron **S**ynchrotron

Danksagung

Auch wenn es zu einer Arbeit gehört sich zu bedanken, so ist es mir auch wirklich ein großes Bedürfnis, dies zu tun. Es ist keine Selbstverständlichkeit die Möglichkeit zu haben in einer internationalen Kollaboration über mehrere Jahre arbeiten und lernen zu dürfen. Es war eine große Freude und ein Privileg so viele interessante, verschiedene Menschen kennenzulernen.

Mein erster Dank geht an Herrn Prof. Dr. C. Gößling für die Betreuung und Korrektur meiner Arbeit. Es war eine großartige Erfahrung diese Arbeit anfertigen zu dürfen.

Herrn Prof. Dr. K. Kröninger möchte ich für die spontane Bereitschaft danken, die Zweitkorrektur dieser Arbeit zu übernehmen.

Frau Dr. B. Siegmann danke ich dafür, dass sie sich bereit erklärt hat, Beisitzer bei meiner Prüfung zu sein.

Herrn Dr. Reiner Klingenberg danke ich für die erhellenden und inspirierenden Diskussionen fachlicher aber auch privater Natur.

Markus Alex gebührt ein ganz besonderer Dank für einfach alles: technische Beratung bei Laboraufbauten, großartigen Support wenn die Rechner mal wieder nicht das machen was sie sollen und immer ein offenes Ohr wenn man von allem und jedem genervt ist. Danke dafür. Ohne dich wäre E4 nicht so ein großartiger Arbeitsplatz.

Im Laufe der Jahre gab es eine Menge E4ler die mich begleitet und unterstützt haben. Hierfür ein dickes Dankeschön an: Kathrin Rumberg die mich seit dem Physik LK durch das Studium begleitet hat, was hatten wir Spaß und was haben wir gelitten, Tobias Köttig für unendlich schlechte Witze, André Rummler für sein allumfassendes Wissen, Christian Jung für gute Traditionen, Oliver Schulz für seine Motivation.

Natürlich darf man auch die aktuellen E4ler nicht vergessen. Danke für ein freundschaftliches und offenes Arbeitsklima am gesamten Lehrstuhl. Selbst die von COBRA sind ok ;) Hervorheben möchte ich meine beiden Büroinsassen Jan und Andreas, es ist einfach schön wenn man gerne an seinem Schreibtisch sitzt. Danke, dass ihr so seid, wie ihr seid. Christian Nitsch für seine Taxidienste und sein immer offenes Ohr für alle kleinen und großen Probleme des Lebens.

Den CERNies gebührt ein großer Dank dafür, dass sich selbst 18 Stunden Testbeam-Schichten wie Urlaub anfühlen weil man nicht ins Hostel muss. Danke für die großartigen Mädelsabende an Steffi, Jenny und Karo. Danke an Daniel für die perfekte Streit-/Diskussionskultur und den Kaffee danach. Rebecca Carney for correcting my English!!!

Danke Malte Backhaus für deine Freundschaft und das Korrekturmeckern. Dabei ist Matthias George nicht zu vergessen. Danke Bademeister und Prinzessin für die vielen unvergesslichen Meetings.

8. *Conclusions and Outlook*

Thanks to all Testbeam people. It was a pleasure to meet you and work with you. Thanks for all the help and the teamwork.

Last but not least ein riesiges Dankeschön an meine Familie für die jahrelange Unterstützung und den Glauben an mich.

Moritz, du weißt besser als jeder andere, dass ich so etwas nicht gut kann. Deshalb schlicht und einfach: Du bist der beste Mann der Welt! Danke für alles!

Bibliography

- [1] C. Lefevre, The CERN accelerator complex. Complexe des accelerateurs du CERN (2006), <http://cdsweb.cern.ch/record/979035/?ln=en> , CERN-DI-0606052
- [2] ATLAS Collaboration, *Letter of Intent for the Phase-II Upgrade of the ATLAS Experiment*, CERN-2012-022 LHCC-I-023, December
- [3] The ATLAS experiment at CERN, <http://atlas.ch>.
- [4] J. Pequeno, *Computer generated image of the ATLAS inner detector*, CERN, (2008), CERN-GE-0803014
- [5] ATLAS Collaboration, *Letter of Intent for the Phase-I Upgrade of the ATLAS Experiment*, CERN-2011-012 LHCC, December 2011
- [6] T. Wittig, *Slim Edge Studies, Design and Quality Control of Planar ATLAS IBL Pixel Sensors*, PhD Thesis, Technische Universität Dortmund, Physik E IV, 2013
- [7] J. Albert et al. [ATLAS IBL Collaboration], *Prototype ATLAS IBL Modules using the FE-I4A Front-End Readout Chip*, JINST 7 (2012) P11010
- [8] M. Capens et al., *ATLAS Insertable B-Layer Technical Design Report*, Tech. rep. CERN-LHCC-2010-013. ATLAS-TDR-19. Geneva, CERN (2010)
- [9] The ATLAS experiment at CERN, <http://www.atlas.ch/news/2014/a-new-sub-detector-for-ATLAS.html>
- [10] C. Nellist, *Characterisation and Beam Test Data Analysis of 3D Silicon Pixel Detectors for the ATLAS Upgrade*, Phd Thesis, Manchester 2013
- [11] A.A.Ay, R.L. Bayt, K.S. Breuer, *Deep reactive ion etching: a promising technology for micro- and nanosatellites*, Smart Materials and Structures 10 no. 6, (2001)
- [12] C. Da Via et al., *3D active edge silicon sensors with different electrode configurations: Radiation hardness and noise performance*, Nucl. instr. Meth. A604 (2009) S505-511
- [13] L. Rossi, P. Fischer, T. Rohe, N. Wermes, *Pixel Detectors, From Fundamentals to Applications*, Springer 2005
- [14] C. Amsler et al. (Particle Data Group), *Physik Letters B667*, (2009)
- [15] G. Lutz, *Semiconductor Radiation Detectors*, Springer 1999
- [16] J. Rietenbach, *Further Development on a read-out system for the Fanout*, Master Thesis, Technische Universität Dortmund (2014)

- [17] Jonas M. Klaiber-Lodewigs, *The ATLAS Pixel Sensor - properties, characterization and quality control*, PhD thesis, Universität Dortmund, (2005)
- [18] K. Dette, *Temperature and high voltage dependent measurements of an irradiated n^+ -in-n ATLAS FE-I4A Single Chip Assembly*, Diploma Thesis, Technische Universität Dortmund, (2013)
- [19] D.Dobos, *Production accompanying testing of the ATLAS Pixel module*, Diploma thesis, Universität Dortmund, (2004)
- [20] G. Troska, *Development and operation of a testbeam setup for qualification studies of ATLAS Pixel Sensors*, PhD Thesis, Technische Universität Dortmund, Physik E IV, 2012
- [21] F. Hürging, *Der ATLAS Pixelsensor - Der state-of-the-art Pixelsensor für teilchenphysikalische Anwendungen mit extrem hohen Strahlungsfeldern*, PhD thesis, Technische Universität Dortmund, (2001)
- [22] M. Barbero et al., *Submission of the first full scale prototype chip for upgraded ATLAS pixel detector at LHC, FE-I4A*, Nuclear Science (2009)
- [23] M. Barbero et al., *The FE-I4 pixel readout chip and the IBL module*, PoS Vertex 2011 038
- [24] M. Backhaus, *High bandwidth pixel detector modules for the ATLAS Insertable B-Layer*, PhD thesis, Friedrich-Wilhelm-Universität Bonn, (2014)
- [25] M. Moll, *Radiation Damage in Silicon Particle Detectors* PhD thesis, Universität Hamburg, (1999)
- [26] ROSE Collaboration, *3rd RD48 Status Report*, CERN LHCC 2000-009, (Dezember 1999)
- [27] R. Wunstorf, *Systematische Untersuchungen zur Strahlenresistenz von Silizium-Detektoren für die Verwendung in Hochenergiephysik-Experimenten*, PhD thesis, Universität Hamburg, DESY, (1992)
- [28] M. Beimforde, *Development of thin sensors and a novel interconnection technology for the upgrade of the ATLAS pixel system*, PhD thesis, TU München, (2010)
- [29] G. Lindström et al., *Radiation hard silicon detectors - developments by the RD48 collaboration*, Nucl. Instr. Meth. A466 (2001)
- [30] P. Lisowski et al., *Los Alamos National Laboratory spallation neutron sources*, Nucl. Sci. and Eng. 106, (1990)
- [31] J. Schneider, H. Krüger, *S3 Multi IO USB Card Version V1.03*, Bonn (2010)
- [32] USBpix - USB based readout system for ATLAS FE-I3 and FE-I4, <http://icwiki.physik.uni-bonn.de/twiki/bin/view/Systems/UsbPix>
- [33] PixLib Scans, <http://icwiki.physik.uni-bonn.de/twiki/bin/view/Systems/PixLibScans>
- [34] D. Autiero et al., *Characterization of the T24 electron beam line available at DESY*, DESY (2004)
- [35] Webpage of the DESY II accelerator, <http://desy2.desy.de>

- [36] D. Cussans, *Description of the JRA1 Trigger Logic Unit (TLU), v0.2c*, EUDET-Memo-2009-04, (2009)
- [37] Martin Kocian, *Update on RCE developments*, Presentation 2014, <https://indico.cern.ch/event/351782/session/2/contribution/16/material/slides/0.pdf>
- [38] EUDET JRA1 Group, *EUDET Pixel Telescope Data Taking Manual - Updated Version for M26*, (2010)
- [39] E. Corrin, *EUDAQ Software User Manual*, (2010)
- [40] M. George, *Testbeam Measurements with Pixel Sensors for the ATLAS Insertable b-Layer Project*, PhD thesis, Georg-August-Universität Göttingen, (2014)
- [41] V. Blobel, *MillepedeII, Linear Least Squares Fits with a Large Number of Parameters*, (2007)
- [42] A. Bulgheroni, T. Klimkovich, P. Roloff, A. Zarnecki, *EUTelescope: tracking software*, EUDET-Memo-2007-20 (2007)
- [43] Branislav Ristic, *Characterization of Planar Pixel Sensors in Test Beam Experiments with Shallow Incidence Angle*, Master Thesis, Technische Universität Dortmund (2013)
- [44] G. Kramberger et al., *Performance of silicon pad detectors after mixed irradiations with neutrons and fast charged hadrons*, Nucl. Instr. Meth. A 609, (2009)

A. Details of Testbeam Measurements

A.1. IBL Testbeam Campaigns

Table A.1.: Efficiencies of IBL assemblies

Sensorname	Efficiency (%)	Bias voltage (V)	Threshold (e)
PS2	93,0	600	1500
	97,6	800	1500
	98,4	1000	1500
	87,0	600	1800
	96,7	800	1800
	98,0	1000	1800
	83,3	600	2000
	96,1	800	2000
	97,6	1000	2000
SCC61	84,9	600	1600
	94,4	800	1600
	96,0	1000	1600
LUB2	95,3	400	1600
	97,2	600	1600
	98,4	800	1600
	98,5	1000	1600
LUB4	97,2	600	1600
	97,9	1000	1600

A.2. MCz and FZ comparison

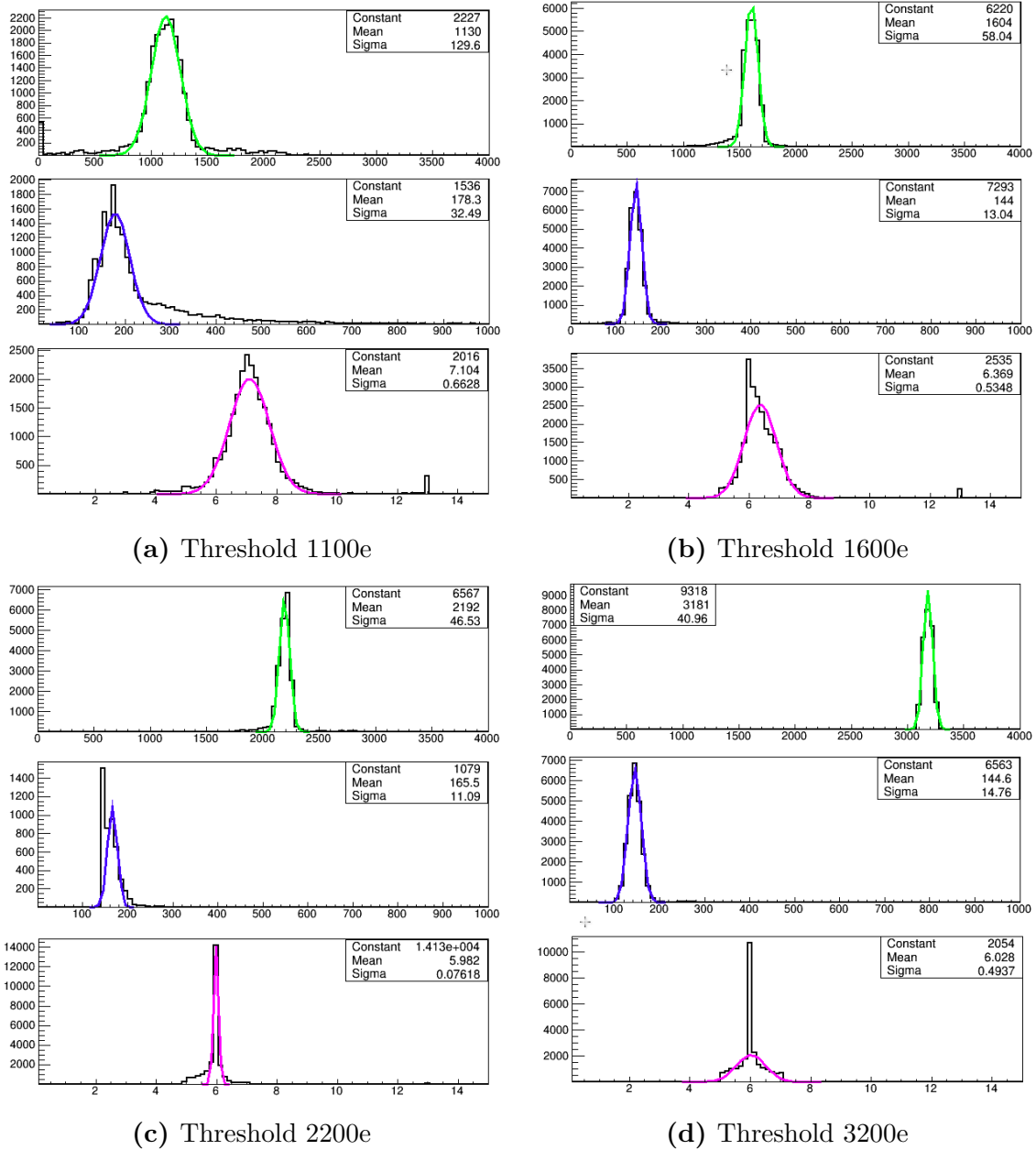
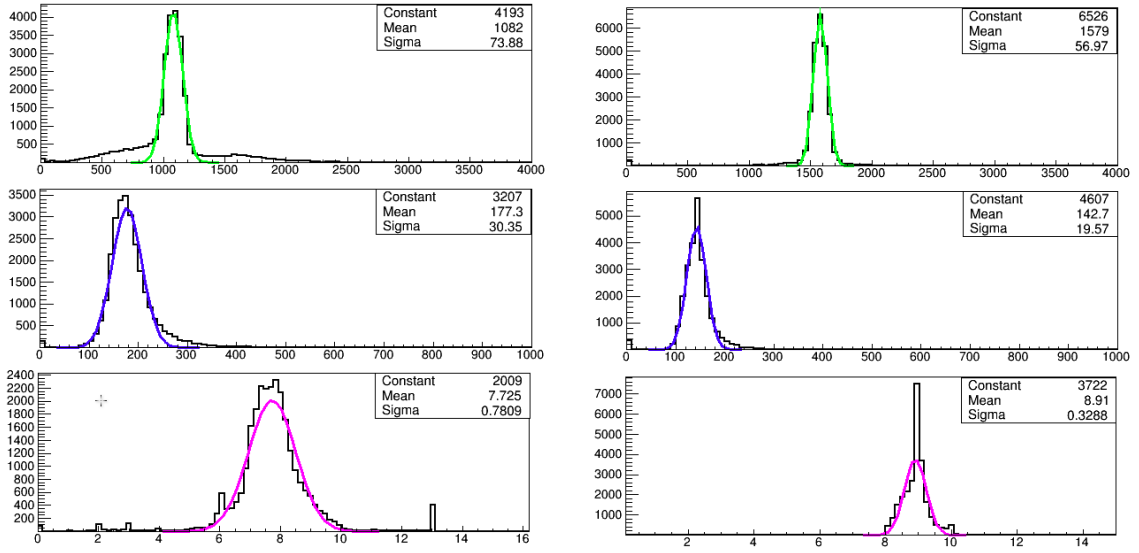
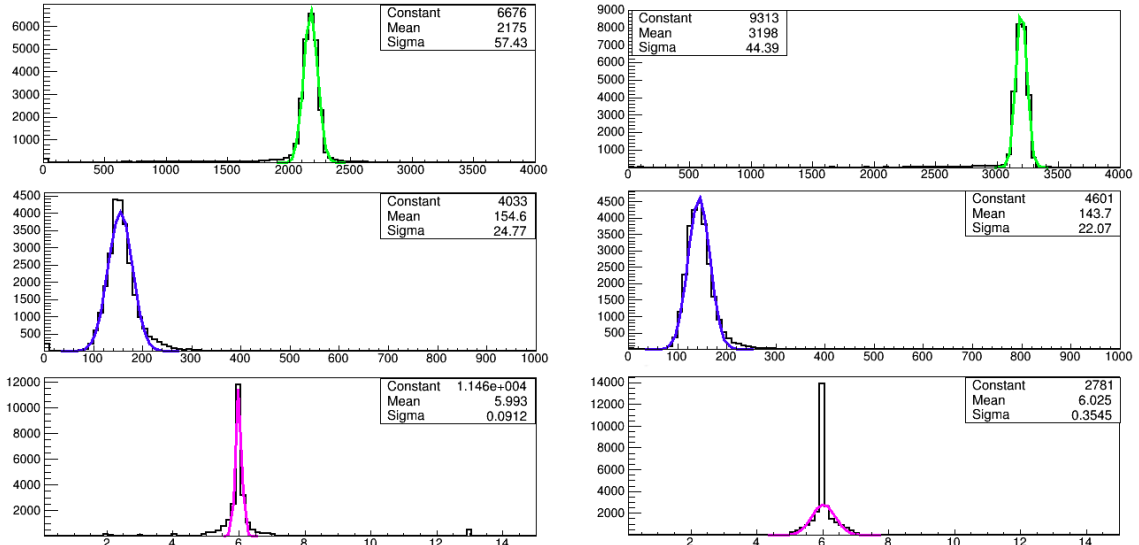


Figure A.1.: Tuning of MCz1 (unirradiated) to four different thresholds with the corresponding noise and ToT at 20ke.



(a) Threshold 1100e

(b) Threshold 1600e



(c) Threshold 2200e

(d) Threshold 3200e

Figure A.2.: Tuning of MCzPi (irradiated) to four different thresholds with the corresponding noise and ToT at 20ke.

A. Details of Testbeam Measurements

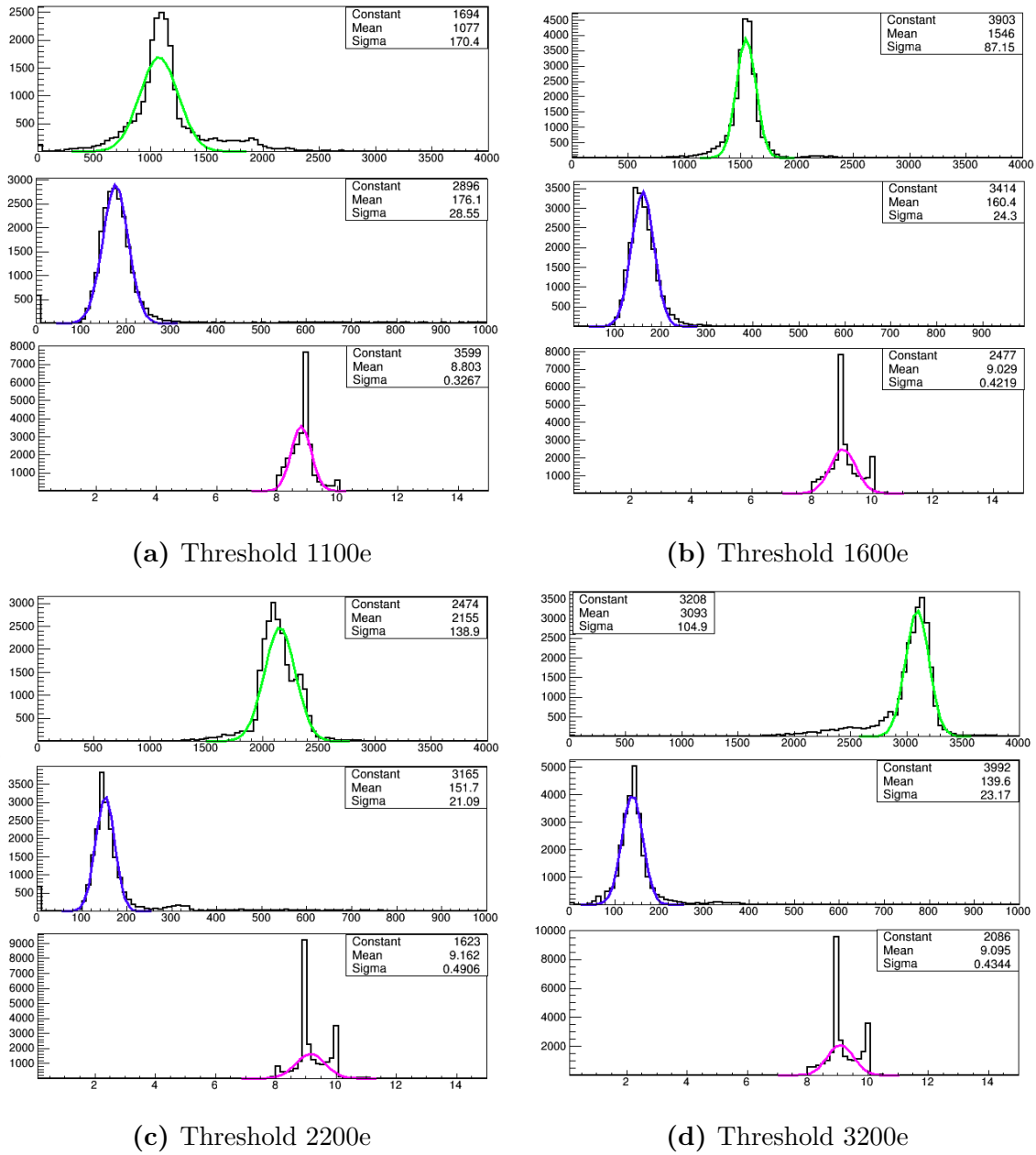


Figure A.3.: Tuning of FZPi (irradiated) to four different thresholds with the corresponding noise and ToT at 20ke.

Table A.2.: Efficiencies of MCz1 from the testbeam in March 2012

Efficiency (%)	Bias voltage (V)	Threshold (e)
98,4	350	1100
98,8	400	1100
98,9	500	1100
99,5	350	1600
99,6	400	1600
99,6	500	1600
99,7	350	2200
99,8	400	2200
99,8	500	2200
99,9	350	3200
99,9	400	3200
99,8	500	3200

B. Publications

Articles

S. Altenheiner for the ATLAS Upgrade PPS R & D Project; *Recent achievements of the ATLAS upgrade planar pixel sensor R & D project*, PoS(TIPP2014)282

R. Klingenberg, **S. Altenheiner**, M. Andrzejewski, K. Dette, C. Gößling, A. Rummler, F. Wizemann; *Temperature-dependent characterization of irradiated planar n^+ -in-n pixel assemblies*, Nucl. Instrum. Meth. A 765: 135-139 (2014)

R. Nagai, ..., **S. Altenheiner**, J. Jentsch, T. Lapsien, A. Rummler, G. Troska et al.; *Evaluation of novel KEK/HPK n-in-p pixel sensors for ATLAS upgrade with testbeam*, Nucl. Instrum. Meth. A 699: 78-83 (2013)

J. Albert, ..., M. Alex, **S. Altenheiner**, C. Gssling, J. Jentsch, R. Klingenberg, T. Lapsien, B. Ristic, A. Rummler, G. Troska, S. von Kleist, T. Wittig et al. (ATLAS IBL Collaboration); *Prototype ATLAS IBL Modules using the FE-I4A Front-End Read-out Chip*, JINST 7, P11010, (2012)

J. Weingarten, ..., **S. Altenheiner**, J. Jentsch, B. Ristic, A. Rummler, G. Troska, T. Wittig et al.; *Planar pixel sensors for the ATLAS upgrade: beam tests results*, JINST 7, P10028, (2012)

S. Altenheiner, C. Goessling, J. Jentsch, R. Klingenberg, T. Lapsien, D. Muenstermann, A. Rummler, G. Troska, T. Wittig; *Planar slim-edge pixel sensors for the ATLAS upgrades*, JINST 7, C02051, (2012)

S. Altenheiner, C. Gößling, J. Jentsch, R. Klingenberg, D. Münstermann, A. Rummler, G. Troska, T. Wittig; *Radiation hardness studies of n^+ -in-n planar pixel sensors for the ATLAS upgrades*, Nucl. Instrum. Meth. A 658: 25-29 (2011)

List of Figures

2.1.	Image of the CERN accelerator complex with its detectors [1]	4
2.2.	Time schedule for the LHC and ATLAS upgrades. Information from[2]	4
2.3.	View of ATLAS during assembly. The muon system, toroid magnets and the inner detector can be seen. [3]	5
2.4.	Components of the inner detector of ATLAS [4]	6
2.5.	Picture of the ATLAS pixel detector during its installation [3]	6
2.6.	Picture of the silicon tracker. [3]	7
2.7.	The completed TRT barrel with all services. [3]	7
2.8.	View of the ATLAS calorimeter along one of eight toroid magnets [3] .	7
2.9.	Installation of the ATLAS muon barrel chambers [3]	7
2.10.	Fluence for the ATLAS Inner Detector as a function of distance from the interaction point (in R outwards and Z along the beam pipe). The fluence is given in units of $1 \text{ MeV n}_{eq}\text{cm}^2$ [6]	9
2.11.	A photo of the pixel detector surrounding the beam pipe during the integration in SR1 (left) [8] and a photo of the insertion of the IBL mounted on a new beam pipe with reduced radius (right) [9]	10
2.12.	Difference in particle detection of a 3D silicon sensor (left) and a planar sensor (right) [10]	11
2.13.	Sketch of the sensor positions on stave.	11
3.1.	Schematic illustration of different crystal defects [20]	13
3.2.	Effective doping concentration is dependent on the fluence, which is shown in a neutron equivalent dosage [27]	14
3.3.	Change of the effective doping concentration in dependence of the annealing time at a temperature of 60°C [25]	16
3.4.	Fluence dependence of the leakage current. Measurements were taken after 80 minutes annealing at 60°C [25]	17
4.1.	Stopping power of muons in copper as function of $\beta\gamma = p/MC$ [14] . .	21
4.2.	Left: The silicon lattice cell shows undoped silicon and has no impurities. Middle: This cell shows n-doped lattice with one loosely bound extra electron. Right: This cell illustrates a p-doped silicon lattice with one electron less. [16]	21
4.3.	Cross section through a silicon sensor with depletion growth for a n-type bulk (a and b) and a p-type bulk (c and d) [18]	22
4.4.	Comparison of N_{eff} for standard and oxygen enriched Float Zone silicon after irradiation with neutrons, protons and pions [26]	23
4.5.	Sketch of the FE-I3 based ATLAS pixel module [20]	23
4.6.	Cross section of the ATLAS pixel sensor	24
4.7.	Schematic of the analogue part of the FE-I3 chip, including a bump bond, the test circuits and the pramplifier and discriminator chain.[6] .	25
4.8.	Tin-silver bump bonding process [6]	26

4.9.	Picture of a IBL Double Chip Sensor with the dimension of the active area.	26
4.10.	a) Edge region of the ATLAS pixel design b) the consevative design and c) the slim edge IBL design. The inactive edge could be reduced from 1100 μm to 200 μm . [6]	27
4.11.	a) Picture and dimensions of a FE-I4. b) Zoom into a 4-pixel region with separated analogue circuits and a combined digital region. c) Picture and dimensions of the current ATLAS readout chip FE-I3 [23]	27
4.12.	Schematics of the analog pixel circuit [24]	28
4.13.	Preamplifier output signals in dependent on the chip DAC values and input charge. (Figure adapted from [19])	29
5.1.	IV-Curve of an irradiated sensor at room temperature.	31
5.2.	Current-Temperature curve of an irradiated sensor at a bias voltage of -500 V.	32
5.3.	Picture of the USBpix readout system [32]	34
5.4.	Analog Scan of an unirradiated Single Chip Assembly	35
5.5.	Digital Scan of an unirradiated Single Chip Assembly	35
5.6.	Histogram of a threshold scan for one pixel.	36
5.7.	Threshold scan of an unirradiated SCA. top: Threshold map for every scanned pixel. bottom: Threshold distribution of the hole SCA.	36
5.8.	Noise scan of an unirradiated SCA. top: Noise map for every scanned pixel. bottom: Noise distribution of the hole SCA.	36
5.9.	Noise against threshold for an unirradiated sensor	36
5.10.	Exemplary threshold tuning of an unirradiated SCA. 1) with standard DAC values, 2) after TDAC tuning, 3) after ToT tuning, 4) after second TDAC tuning	37
5.11.	Time over Threshold Scan of an unirradiated SCA after tuning.	38
5.12.	Histogramm of a source scan with a few noisy pixels (left) and the loadable mask histogramm for all pixels with higher entries than five (right).	39
5.13.	Histogramm of a Source Scan of an unirradiated SCA with a Sr^{90} source.	39
5.14.	Charge distribution from the source scan.	39
5.15.	Noise occupancy scan of a proton irradiated SCA.	39
5.16.	Noise occupancy scan of a neutron irradiated SCA where the tantalum in the FE-I4 got activated.	39
5.17.	SCC before new cable.	40
5.18.	SCC with new soldered cable for bias voltage.	40
5.19.	IV curve of an irradiated assembly before and after soldering a new cable. Taken at -25°C air temperature.	41
5.20.	New high voltage single chip card with the possibility to power only segments of the single chip.	41
5.21.	Sketch of the piping for the silicone oil and the dry air.	42
5.22.	Pictures of the source carrier.	43
6.1.	Drawing of the SPS target area. The primary beam passes to dipole magnets to change incident angle into the target, the secondary particles passing a spectrometer magnet are collimated and guided to two beamlines [20].	45
6.2.	Schematic layout of the electron/positron production at DESY [34]	46
6.3.	Picture of the view inside the DESY II tunnel [35]	46

6.4.	Sketch of a standard testbeam setup [10].	47
6.5.	Picture of three EUDET telescope planes	48
6.6.	Picture of the telescope with the DOBox mounted between the two telescope arms and connected USBPix systems.	48
6.7.	Computer aided design of the DOBox with an open view of the dry ice department. [20]	49
6.8.	Picture of the DOBox with open dry ice department directly after removing the dry ice.	49
6.9.	SCA front with PT1000	49
6.10.	SCA back copper tape	49
6.11.	Rotation plate	50
6.12.	Wedges	50
6.13.	Eudaq run control panel. [39]	50
6.14.	Screenshot of the Online Monitor correlation plots for the MIMOSA plane 2 with all other MIMOSA planes and the DUTs for run 50880 at the IBL testbeam in march 2012.	51
6.15.	Screenshot of the Online Monitor ToT Cluster of DUT0 during the PPS testbeam in March 2013. Run 1541 with a DUT tuning of 3200 e with 6 ToT at 20000 e, at a bias voltage of -500 V.	52
6.16.	Screenshot of the Online Monitor Hot Pixel map. For this tuning with a threshold of 3200 e no pixel is identified as hot. (PPS TB 2013, DUT0, run 1541)	52
6.17.	Screenshot of the Online Monitor Hot Pixel map. For this tuning with a threshold of 1100 e a few pixels (<1 %) are identified as hot. (PPS TB 2013, DUT0, run 1725)	52
6.18.	Screenshot of the LVL1 pixel distribution for DUT0 which is proton irradiated with a fluence of $5 \cdot 10^{15} n_{eq}/cm^2$ during the IBL testbeam in march 2012.	53
6.19.	Hitmap	53
6.20.	Screenshot of all informations the Online Monitor provides for DUT0 during the PPS testbeam in March 2013, only filled with run 1541.	54
6.21.	The track reconstruction chain for the testbeam data. [40]	55
6.22.	Screen shot from the log file after running the Hotpixel finder for run 1521 - 1535 from the PPS testbeam in March 2013.	58
6.23.	Hitmap (top) and occupancy mask (bottom) for run 1521-1535 for DUT0 from the PPS testbeam in March 2013.	58
6.24.	Example histograms from the Check align step in TBmon. The data points far off the horizontal lines are at the edge of the scintillator region and have low statistics.	59
6.25.	Hitmaps from DUT0 (PPS TB March 2013, run 1521-1535). Left: Hitmap without any cuts, just counting the number of hits per pixel. Right: Hitmap after applying timing cuts and only hits are taken into account that can be matched to a track.	60
6.26.	Histogram of the efficiency for DUT0 during the PPS TB in March 2013 run 1521-1535.	61
6.27.	Efficiency detail of the log file for DUT0 and DUT1 for run 1521-1535 during the PPS TB in March 2013.	61
6.28.	Average Residual plot against time for DUT22 in run 61510 during the IBL TB in September 2011. [43]	62

6.29. Efficiency maps of FBK13 (left) and PS2 (right) from the IBL TB in March 2012.	63
7.1. Logged current values of LUB2 during the IBL testbeam in April 2011 at -1000 V plotted against time.	66
7.2. Heatingresistor mounted on the backside of LUB4.	67
7.3. PT1000 positions directly on sensor and on the aluminium carrier.	67
7.4. Time vs temperature of LUB4 during IBL testbeam September 2011.	67
7.5. Time vs current of LUB4 during IBL testbeam september 2011.	67
7.6. Tunings of PS2 for each threshold step measured in the IBL testbeam in March 2012. In every histogram the threshold is shown in green, the corresponding noise in blue and the ToT at 10ke in magenta.	69
7.7. LVL1 distribution for PS2 at all applied voltages and all adjusted thresholds during the IBL testbeam in March 2012.	70
7.8. Percentages of the noise floor with respect to the peak height for every threshold and bias voltage.	71
7.9. Hitmap of PS2 from the IBL testbeam in March 2011 at 600 V with a threshold of 1800 e without any cuts.	71
7.10. The average efficiency of PS2 during the IBL testbeam in March 2012 in dependency of the applied bias voltage and the threshold.	72
7.11. Analog and digital scan of SCC60.	73
7.12. Dependency of dead pixel on the value of Amp2Vbpf for the analog (left) and digital (right) part of the FE-I4.	73
7.13. Tuning of SCC61 to a desired threshold of 1600 e with the corresponding noise and ToT at 10 ke.	74
7.14. LVL1 distribution for SCC61 during the IBL testbeam in June 2011 for every applied bias voltage without cuts.	74
7.15. Raw hitmap of SCC61 with a threshold of 1600 e at 600 V (left) and 800 V (right).	74
7.16. Efficiency map of SCC61 at a threshold of 1600 e and an applied bias voltage of 800 V.	75
7.17. The average efficiency of SCC61 during the IBL testbeam in dependency of the applied bias voltage at a threshold of 1600 e.	75
7.18. Tunings for LUB2 (left) and LUB4 (right) during their testbeam campaigns. The desired threshold for both were 1600 e. The ToT for LUB2 was 5 at 20ke and for LUB4 8 ToT at 10ke.	76
7.19. LVL1 distribution for LUB4.	76
7.20. LVL1 distribution for LUB2.	77
7.21. The average efficiency of LUB4 during the IBL testbeam in and LUB2 during the IBL testbeam in dependency of the applied bias voltage at a threshold of 1600 e.	77
7.22. Hit efficiency maps of the edge of LUB2 at four different bias voltages. LUB2 was tuned to a threshold of 1600 e. The pixel cell contours are marked in black and the high voltage pad at $250 \mu\text{m}$ and the guard rings are marked in grey. [6]	78
7.23. IV curve of MCzPi before and after pion irradiation. Measurement done before irradiation at room temperature after at -15°C on sensor.	80
7.24. IV curve of FZPi before and after pion irradiation. Measurement done before irradiation at room temperature after at -15°C on sensor.	80

7.25. CV curve of a unirradiated MCz sensor.	81
7.26. CV curve of a unirradiated DOFZ sensor.	81
7.27. Noise vs. threshold for MCz and FZ sensors before and after irradiation.	82
7.28. Hitmap and efficiency map of MCz1 with a threshold of 3200 e at 400 V during the testbeam in March 2013.	82
7.29. Average efficiency of MCz1 from the testbeam in March 2013 for four thresholds in dependence of the applied bias voltage.	83
7.30. ToT distribution of FZPi at a bias voltage of 500 V for four different thresholds and a ToT of 8 for 16 ke.	84
7.31. LVL1 distribution for FZPi at a bias voltage of -500 V for four different thresholds.	85
7.32. Hitmap and ToT distribution of MCzPi at a bias voltage of 500 V for three different thresholds and a ToT of 8 for 16 ke.	85
7.33. LVL1 distribution for MCzPi at a bias voltage of -500 V for four different thresholds.	86
7.34. ToT distribution of MCzPi at a bias voltage of 800 V for four different thresholds and a ToT of 8 for 16 ke.	86
7.35. LVL1 distribution for MCzPi at a bias voltage of -800 V for four different thresholds.	87
A.1. Tuning of MCz1 (unirradiated) to four different thresholds with the corresponding noise and ToT at 20ke.	98
A.2. Tuning of MCzPi (irradiated) to four different thresholds with the corresponding noise and ToT at 20ke.	99
A.3. Tuning of FZPi (irradiated) to four different thresholds with the corresponding noise and ToT at 20ke.	100

List of Tables

6.1. Content of the final output file of the reconstruction.	57
7.1. FE-I4 devices under test	65
7.2. Current of the IBL testbeam sensors at -1000V scaled to -15°C, the current per pixel and the power dissipation.	68
A.1. Efficiencies of IBL assemblies	97
A.2. Efficiencies of MCz1 from the testbeam in March 2012	101